SIMULATION OF FLUID FLOW THROUGH FRACTURED ROCK

A SMEARED APPROACH

T.M. GRUBBEN

Student number:	4454421	
Date:	November 6, 2020	
Thesis committee:	Assoc. Prof. Dr P. J. Vardon,	TU Delft
	Assis. Prof. Dr A. A. M. Dieudonné,	TU Delft
	Assoc. Prof. Dr A. Barnhoorn,	TU Delft
	Dr G. M. A. Schreppers,	DIANA FEA

DELFT UNIVERSITY OF TECHNOLOGY

Faculty of Civil Engineering & Geosciences
MSc. Geo-Engineering

Preface

This thesis describes the development and evaluation of a new material model in the Diana FEA software that allows for the simulation of fluid flow through fractured rock, based on a smeared approach. It furthermore seeks to identify the applicability and limitations of the current state of the model and provides recommendations for further model development.

The research is part of the master programme Geo-Engineering at the faculty of Civil Engineering and Geosciences at the TU Delft, and has been conducted in collaboration with Diana FEA bv.

I would like to thank my supervisors; Gerd-Jan Schreppers, Phil Vardon, Anne-Catherine Dieudonné and Auke Barnhoorn, for their great guidance and support during the process. It has been very much appreciated. Furthermore, I would also like to thank Diana FEA and its employees, for providing me with the knowledge and tools that were necessary for conducting the research.

As this thesis marks the end of my time as a student at the TU Delft, I also want to express my appreciation for my family and friends, who have always been supportive through all these years. My parents deserve a special note of thanks for their endless words of counsel and encouragement. And finally, Pippi Eikhout, thank you for not only offering me a place to work on my thesis during the pandemic, but also being the very best study partner.

I hope you enjoy your reading,

Tessel Grubben
November 6, 2020

Summary

Geothermal energy reservoirs can be used as sources of renewable and sustainable energy, which technology resides on the harvesting of heat from deep rock formations. Geothermal reservoirs that require permeability improvement are termed Enhanced Geothermal Systems (EGS). The presence of fractures will, on the one hand decrease the flow resistance in the reservoir, yet on the other hand, lead to a higher rate of temperature drawdown, which poses a contradicting dilemma. For a reservoir engineer, being able to predict and control the size, orientation and density of the fractures is thus a crucial component of the reservoir design optimisation. This study, therefore, aims to develop a model using DIANA Finite Element Analysis software that can simulate the flow through fractured rock.

The modelling of a geothermal energy system is a complex challenge as the model should be able to represent the interplay between the geomechanical, hydraulic and thermal mechanisms occurring in the rock. A model of geothermal energy systems in the subsurface can be formulated as a coupled Thermo-Hydro-Mechanical fracture problem. The continuously coupling between these aspects is governed by the stresses, pore pressures, temperatures, deformation and fractures of the rock.

Cracks are often represented according to a discontinuum approach because of a crack's discrete nature. However, when examining a THM fracture problem, adhering to a smeared approach is considered to be suitable as well. The smeared crack approach expresses the cracked rock as a material with equivalent anisotropic continuum properties. It is better capable at simulating fracture branching and representing multiple cracks with non-predetermined directions, and also poses computational advantages over the discontinuum approach.

The fluid flow through a porous, fractured medium can be described by Darcy's law, whereby the permeability represents the permeability of the porous rock and the fracture networks. The permeability of a single fracture can be derived based on the cubic law for fluid flow, which leads to an expression of the permeability as a quadratic function of the aperture. The aperture can be calculated based on the rock deformation, and thereby provides coupling between the hydro- and geomechanical behaviour of the medium.

Within the smeared crack concept Diana FEA offers two different non-masonry/concrete fracture material models: the Total Strain crack model and the Multi-Directional Fixed crack model. They are both capable of simulating multiple cracks occurring in one point (both space and time) but differ in their definition of the crack strain. Diana FEA offers a mixture analysis, which considers an extra degree of freedom in addition to the displacement in the form of a pore pressure potential. Darcy's law relates the fluid flow in the porous media with the gradient in the pore pressure potential through the modified permeability k'.

This study proposes a new fracture-dependent material model, that can be used in combination with other smeared, fracture models in the Diana FEA software. The model takes into account the presence of fractures through the deformation of the material and therefore enables the simulation of the altered fluid flow through the fractured rock. The model considers only tensile cracks (mode I) and employs a rotating crack model for computational purposes. Cracks are defined to occur if the principal strain exceeds a crack strain threshold, whereby the fracture will propagate in the direction orthogonal to the main principal strain. It assumes that a single fracture can be represented by the parallel plate model and the fluid flow through the fracture can thus be described by the cubic law, where the permeability is a function of the fracture aperture. For the actual implementation of the fracture-dependent permeability, three new subroutines have been created. These subroutines express the updated permeability as a relative permeability factor, which direction and magnitude depends on the size and orientation of the fractures. For achieving this, two different methods are suggested: method 1 treats the medium as a continuum with fracture-dependent properties, thereby expressing the change in permeability as an overall change in the permeability of the rock mass. Method 2 separately takes the effects of the fractures into account by adding a fracture permeability to the initial permeability of the rock mass.

For evaluating the model's ability to simulate fluid flow in fractures near geothermal boreholes, the results are compared with a different numerical study on hydraulic fracturing. The comparison shows that the model is quite capable of simulating the development of fractures and corresponding changes in permeability. The analyses indicate that simulations according to method 1 display a much more instantaneous increase in permeability at the onset of cracking, whereas method 2 shows a much more gradual increase. A mesh-dependency analysis shows that the model is not entirely objective with respect to its mesh. However, this dependence can be very much improved for method 1 if b_0 is defined as function of the tensile strain and crack bandwidth instead of a single parameter, resulting in a converging solution. Furthermore, the model appears to be very sensitive to its input parameters, being b_0 (initial aperture) for method 1 and the JRC (Joint Roughness Coefficient) for method 2. Method 2 next to this also displays a sensitivity to the initial permeability, thereby limiting its applicability.

The applicability of the model is also evaluated in situations other than EGS. A case study concerning the hydro-mechanical behaviour in excavation damaged zones near underground galleries shows that the model is only capable of simulating the behaviour to a limited extent. This limitation can most be attributed to the fact that the model lacks an elaborate description of an initially cracked state or heterogeneities in the rock, and it only incorporates mode I (extensional) fractures and can not account for shear fracturing. Furthermore, the case study also illustrates that the strain crack criterion and a rotating crack approach, may not be suited in every situation.

With regards to further development of the model, the study recommends a merging of the two proposed methods, thereby combining both their advantages as well as disadvantages. It also suggests incorporating a more detailed description of the initially cracked stated of the rock, which includes not only the aperture of the fractures but also their direction. And finally, for achieving a more comprehensive model, it is recommended to incorporate the thermal effects and other modes of fracturing apart from tensile cracks in the expression for the fracture-dependent permeability.

Nomenclature

Abbreviations

EDZ	Excavation Damaged Zone
EGS	Enhanced Geothermal Systems
EPFM	Elasto-Plastic Fracture Mechanics
LEFM	Linear Elastic Fracture Mechanics
M1	Method 1
M2	Method 2
THM	Thermo-Hydro-Mechanical

Symbols

α	Permeability factor	1
α_{TD}	Fracture threshold angle	rad
β	Shear retention factor	1
ε	Strain	1
ε^{cr}	Global crack strain	1
ε_n	Crack normal strain	1
ε_t	Crack strain criterion	1
ε_u^{cr}	Ultimate crack strain	1
ε_{nst}	Strain in the crack coordinate system	1
$\varepsilon_{u,min}^{cr}$	Minimum ultimate crack strain	1
ε_{xyz}	Strain in element coordinate system	1
μ	Dynamic viscosity	$N \cdot m^{-2} \cdot s$

ν	Poisson's ratio	1
ϕ	Friction angle	rad
ψ	Dilatancy angle	rad
ψ	Shear capacity	1
ρ	Density	$kg \cdot m^{-3}$
σ	Stress	$N \cdot m^{-2}$
σ^{cr}	Global crack stress	$N \cdot m^{-2}$
σ_H	Major principal stress	$N \cdot m^{-2}$
σ_h	Minor principal stress	$N \cdot m^{-2}$
σ_{ci}	Uniaxial compressive strength	$N \cdot m^{-2}$
σ_{nst}	Stress in crack coordinate system	$N \cdot m^{-2}$
σ_{xyz}	Stress in element coordinate system	$N \cdot m^{-2}$
τ	Tortuosity	1
θ	Crack direction angle	rad
ξ	Hydraulic aperture factor	1
A	Area	m^2
b	Mechanical fracture aperture	m
b^*	Hydraulic fracture aperture	m
b_0	Initial fracture aperture	m
c	Cohesion	$N \cdot m^{-2}$
c	Kozeny constant	1
COD	Crack Opening Displacement	m
$CTOD$	Crack Tip Opening Displacement	m
DF	Darcy flux	$m^{-1} \cdot s^{-1}$
E	Young's modulus	$N \cdot m^{-2}$
e^{cr}	Individual crack strain	1
f_c	Compressive strength	$N \cdot m^{-2}$
f_t	Tensile strength	$N \cdot m^{-2}$
G	(Strain) Energy release rate (surface area)	$J \cdot m^{-2}$

g	Energy release rate (volume)	$J \cdot m^{-3}$
g	Gravitational acceleration	$m \cdot s^{-2}$
G_c	Critical energy release rate	$J \cdot m^{-2}$
h_{cr}	Crack bandwidth	m
I	Identity matrix	1
J	Energy release rate (non-linear)	$J \cdot m^{-2}$
JRC	Joint Roughness Coefficient	1
K	Hydraulic conductivity	$m \cdot s^{-1}$
K	Stress intensity	$kg \cdot s^{-2} \cdot m^{-1/2}$
k	Permeability	m^2
k'	Modified permeability	$m^3 \cdot s \cdot kg^{-1}$
k'_0	Initial modified permeability	$m^3 \cdot s \cdot kg^{-1}$
K_c	Critical stress intensity or fracture toughness	$kg \cdot s^{-2} \cdot m^{-1/2}$
K_f	Bulk modulus fluid	$N \cdot m^{-2}$
K_s	Bulk modulus solid	$N \cdot m^{-2}$
l^*	Characteristic length	m
m_b	Hoek and Brown failure criterion constant	1
n	Porosity	1
q	Equivalent shear stress	$N \cdot m^{-2}$
q_{mc}	Morh-Coulomb failure criterion	$N \cdot m^{-2}$
R	Crack resistance	$J \cdot m^{-2}$
S	Surface area per volume	$m^2 \cdot m^{-3}$
s	Fracture spacing	m
s	Hoek and Brown failure criterion constant	1
s^{cr}	Individual crack stress	$N \cdot m^{-2}$
s_{mx}	Crack control characteristic	m
T	Temperature	K
T	Transformation matrix	1
T	Transmissivity	$m^2 \cdot s^{-1}$
w	Fracture width	m

Contents

List of Figures

List of Tables

1. Introduction

Geothermal energy reservoirs located in subsurface rocks can be used as sources of renewable and sustainable energy for heating systems or electricity networks. The concept of geothermal technology relies on the harvesting of heat from deep rock by injecting fluid that circulates through the porous, fractured reservoir rock between injection and production boreholes and thereby transports the heat to the ground surface.

Flow rates in geothermal energy reservoirs depend on the porosity structures in the rock, being the pores and the fractures. The presence of fractures can strongly increase the permeability of the rock and thereby enhance the flow circulation in the system. Properly being able to model the fluid flow through the porous, fractured rock is therefore of importance in the optimization of reservoir design. For that reason, this study aims to develop a model using DIANA Finite Element Analysis software that can simulate the fluid flow through fractured rock. The research, first of all, focuses on investigating how the coupling between fracture development and fluid flow can be modelled, and once a model has been established, explores the applicability and limitations of the model.

This study proposes a new material model, which relates fracture initiation and propagation with a change in permeability of the rock, assuming a smeared approach. This fracture-dependent permeability model can be used in combination with other fracture models in the Diana FEA software, that account for the stress and strain redistribution due to presence of fractures. The hydro-mechanical behaviour of fractured rock in geothermal energy reservoirs can be simulated, by performing a mixture analysis on a rock that is described by the fracture-dependent permeability model.

A literature study is conducted, attempting to provide a theoretical framework for the derivation of the model. This study deals with the following three main topics: thermo-hydro-mechanical processes in geothermal energy reservoirs, fracture mechanics of rock, and the effect of fractures on the bulk permeability and fluid flow of the rock. Subsequently, the steps required for the implementation of the model can be determined, by evaluating the theoretical framework based on their computational aspects and by looking into how the Diana software currently simulates fracture development and fluid flow. Based on that evaluation, the context of the already existing fracture material models and mixture analysis can be identified.

After the fracture-dependent permeability model has been defined and implemented in the Diana FEA software, the simulations are evaluated. The main goal is to identify the applicability and limitations of the newly developed model, and compare between the two different methods that are proposed for the calculation of a fracture-dependent permeability. The final phase therefore considers a few different test cases that verify and evaluate the workings and objectivity of the model according to its two methods. The objectivity evaluation includes a mesh-dependency analysis, and furthermore, aims to map the sensitivity of the model to its input parameters. Simulations are first of all compared with another numerical study on hydraulic fracturing in geothermal energy reservoirs.

Secondly, a study on the hydro-mechanical behaviour in excavation damaged zones is discussed, thereby evaluating the usage of the model to a broader extent.

The outline of the report is as following: The study commences with a short chapter providing background information on geothermal energy reservoirs in Chapter 2. Next, the literature study is discussed in Chapter 3. The function of this study is to provide the theoretical framework for model development. Furthermore, a bridge is made between the theory and the computational aspects of the model implementation, thereby also evaluating which models and type of analyses are already available in Diana as the model will be developed forming an extension to the Diana FEA software. Based on this theoretical research, a model concept is proposed, and its practical implementation into the software is dealt with in Chapter 4. Chapter 5 describes the first results of simple 2D and 3D simulations that were performed using the new code. The aim of this chapter is to demonstrate and verify the workings of the model, thereby also providing initial insight into the sensitivity of the model to some input parameters. A different numerical study on hydraulic fracturing is discussed in Chapter 6, results are compared with simulations by the fracture-dependent permeability model. Moreover, this study is used as a starting point for the objectivity evaluation of the model, which considers a mesh-dependency and a parameter sensitivity analysis. Both analyses can be found in Chapter 6 as well. A case study describing a situation other than EGS, where potentially the model can also be applied to, is presented in Chapter 7. This case study concerns the hydro-mechanical behaviour of excavation damaged zones surrounding underground galleries. The aim of comparing results with this case study is to investigate the applicability of the model in a broader sense. All relevant methods and assumptions concerning the model development and evaluation of the methods are discussed in Chapter 8. And finally, the study is concluded on in Chapter 9. This chapter also includes recommendations for further development.

2. Geothermal energy reservoirs

2.1 Introduction

The concept of geothermal technology as a source of renewable and sustainable energy resides on the harvesting of heat from deep rock formations. The collected thermal energy can be converted into electricity or can be used directly in heating networks. The extraction of the geothermal energy aims at rock reservoirs located at a depth shallower than 5 km and temperatures between 100 and 400 °C. The fluid is injected into the hot rock mass and circulates between the injection and production boreholes, thereby transporting heat to the ground surface (Tomac and Sauter, 2018).

The rock formations that form the natural reservoirs for the harvesting of geothermal energy are often tight and have low initial permeability. The rock must therefore be fractured in order to generate sufficient fluid circulation rates. The fracturing can be achieved through hydraulic fracturing techniques, in which (cold) pressurized fluid is injected into the deep hot rock through wells, thereby producing new fractures. Geothermal reservoirs that require permeability improvement are termed Enhanced Geothermal Systems (EGS). The concept and modelling of EGS will be discussed in the following sections.

2.2 Enhanced Geothermal Systems

The term Enhanced Geothermal Systems (EGS) is used to describe projects that involve the modification of rock permeability for the creation, or the enhancement of an existing, geothermal reservoir (Grant, 2013). According to Grant (2013), there are two main parameters that summarise the performance of an EGS from an engineering point of view being, firstly, the resistance to the flow between two wells, and secondly, the rate of temperature drawdown of the produced water. The presence of fractures creates a contradicting dilemma concerning these two parameters. On the one hand, the fractures will decrease the flow resistance and thereby lower the required pumping power, however, on the other hand, they will also lead to a higher rate of temperature drawdown due to the increase surface area that is now available for heat exchange between the fluid and the rock. A reservoir engineer should therefore aim to find an appropriate balance between flow resistance on the one side and temperature draw down on the other in the design of the EGS. Being able to predict and control the size, orientation and density of the fractures is thus a crucial component of the design optimisation.

Fluid flow

The most straightforward representation of the flow in a geothermal reservoir is by the analogy of fluid flow in a confined aquifer (Grant, 2013). A confined aquifer is a layer of permeable, water-bearing rock that is fully saturated. Figure 2.1 shows the fluid flow in an

exploited geothermal reservoir. The arrows at the top of the figure illustrate the injection and production wells. Pressurized, cold water is injected in the rock, as it travels through the reservoir it slowly decreases in pressure and increases in temperature due to the heat exchange with the rock formation. The heated water is extracted at the production well.

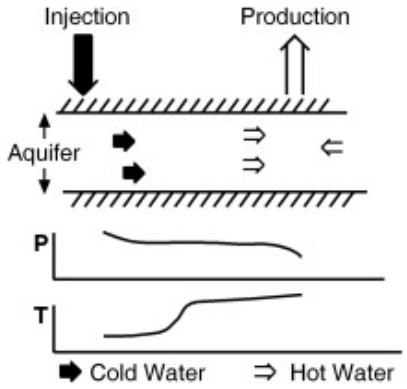

Figure 2.1: Fluid flow in an exploited geothermal reservoir (Grant, 2013).

Fracture development

The development of fractures around a geothermal well strongly depends on the in-situ rock stress. Assuming S_1, S_2 and S_3 are the principal (compressive) stresses of the rock, where S_1 is parallel to the direction of the wellbore axis and $S_2 \geq S_3$, then the maximum tensile stress at the edge of the wellbore (σ_θ) is given by (Hubbert and Willis, 1957)

$$(\sigma_\theta)_{max} = p + S_2 - 3S_3 \tag{2.1}$$

where p is the pressure of the injected fluid. The maximum tensile stress can be found at points B and B' at the edge of the wellbore shown in Figure 2.2. The wellbore has a radius equal to R_w, and the length of the cracks is indicated by a. It is assumed that fracturing occurs when σ_θ reaches the tensile strength of the rock.

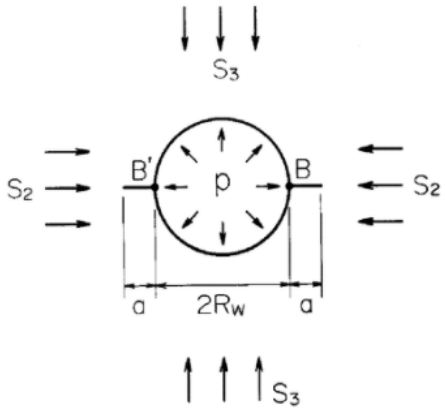

Figure 2.2: In-situ rock stresses and injected fluid pressure around a wellbore with cracks (Atkinson and Meredith, 1987).

If the tensile strength of the rock is reached, due to the increased fluid pressure in the wellbore, the rock will part most easily in the direction of the least compressive stress

(S_3). Consequently, a fracture develops orthogonal to this direction, thus in the direction of S_2 (Grant, 2013). See Figure 2.3 below for the visualisation of fracture development.

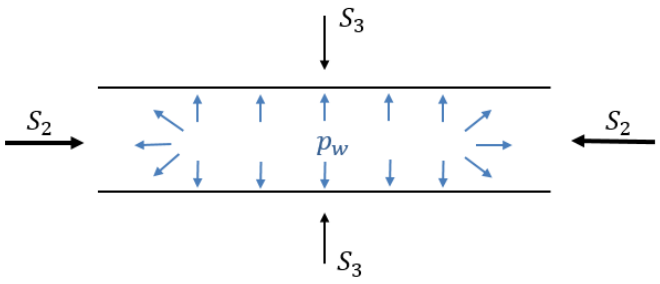

Figure 2.3: Fluid pressure causing the rock to part in the direction of the least stress.

During the extraction of geothermal energy, there are also thermal effects that play a role in the fracture development around a wellbore. As cold water is injected, the surface of the crack is cooled by the fluid leading to thermal contraction of the rock. The contraction may result in the formation of tension cracks perpendicular to the surface of the original fracture, consequently resulting in a loss of flow rate. Furthermore, the volume and thus the aperture of the original fracture may increase significantly due to the thermal contraction, increasing the local permeability. And finally, the thermal contraction poses additional thermal stresses on the rock, giving rise to an increasing stress intensity at the crack tip, which can result in fracture propagation (Atkinson and Meredith, 1987).

2.3 Thermo-Hydro-Mechanical modelling

The coupled processes in geothermal energy reservoirs can be represented by a Thermo-Hydro-Mechanical model (THM model). Correctly modelling processes in geothermal reservoirs can be a challenging task as it involves the coupling of many different components. Geothermal processes disturb the initial stress field as fluid gradients, and rock temperature differences cause additional stresses to the mechanical stress field in the rock. Increased local shear stresses and pore pressures cause the stress field to rearrange and to rotate the local principal stresses, which results in fracture initiation and propagation in highly stressed rock (Tomac and Sauter, 2018). Fracture properties, such as aperture, orientation, connectivity and length, are affected by the geomechanical response of the rock to the thermal and fluid-induced stresses. These fracture properties consequently govern the fluid and heat flow through the rock, thereby rearranging fluid and temperature gradients.

Many studies have been carried out in which an attempt is made to formulate a fully coupled THM model, where generally speaking the outline of the models is more or less the same. The THM model is subdivided into three sub-models: a geomechanical, thermal and a flow model. In a fully coupled model, these three models run simultaneously and continuously interact. In many THM models, the thermal and flow model are once again subdivided in a matrix and a fracture thermal/flow model. In some cases this distinction is also made for the geomechanical model, depending on the applied constitutive model. A schematic overview of a simplified THM model is given in Figure 2.4. This scheme has been assembled based on the models presented in the studies by Chen et al. (2007),

Adachi et al. (2007), Zhou et al. (2009), Kissling et al. (2015), Gan and Elsworth (2016 and Salimzadeh et al. (2018). The following physical quantities govern the coupling between the different mechanisms:

- Mechanical (in-situ) stress: Anisotropic stress field may lead to highly localised stresses and strains, resulting in the initiation and propagation of fractures. Stresses are affected by pore pressures and thermal influences;
- Pore pressure (gradient): Pore pressure affect the stress state, possibly causing the principal stresses to rearrange and the bulk to deform. The pore pressure gradient induces a fluid flow;
- Temperature (gradient): Temperature can induce thermal contraction of the rock resulting in additional (secondary) cracks and thermal stresses. Furthermore, temperatures affect the mechanical properties of the rock as well as the dynamic viscosity of the fluid. And a temperature gradient results in advective flow through the fractures and advective and conductive flow through the porous medium;
- Deformation: Deformation of the rock affects the fluid and thermal flow through the porous medium and fractures. Deformation can be caused by additional (thermal) stresses or increased fluid pressure;
- Aperture: Fracture development, and consequently an increase in fracture aperture, is a result of highly localised stresses and strains. A greater aperture increases the permeability of the fractures, thereby enhancing fluid flow and advective heat transport.

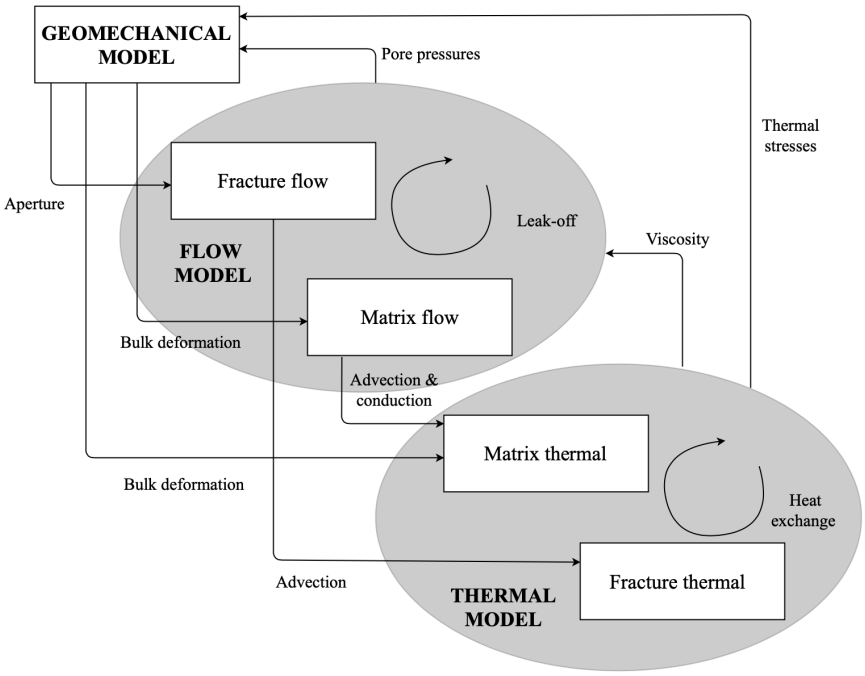

Figure 2.4: Schematic representation of a simplified THM model.

2.4 Conclusion

The rock forming the geothermal reservoir often has a low intrinsic permeability. In the case of Enhanced Geothermal Systems, the permeability of the formation is increased through hydraulic fracturing. The condition and direction of these induced fractures play an important role in the optimization of the geothermal energy reservoir.

Fracturing occurs when the injected fluid pressure is increased, and the maximum tensile stress at the edge of the wellbore exceeds the tensile strength of the rock. The fluid pressure pushes the rock in the direction of the least resistance (least compressive in-situ stress), and therefore the fracture propagates in the orthogonal direction. Temperature differences can induce additional thermal effects, such as thermal contraction and the occurrence of secondary tension cracks.

The modelling of a geothermal energy system is a complex challenge as the model should be able to represent the interplay between the geomechanical, hydraulic and thermal mechanisms occurring in the rock. A model of geothermal energy systems in the subsurface is thus formulated as a coupled Thermo-Hydro-Mechanical fracture problem. In short, a THM fracture problem consists of five main concepts (Gan and Elsworth, 2016; Salimzadeh et al., 2018):

1. Fracture mechanics;
2. Fluid flow in the fracture;
3. Fluid flow in the porous rock;
4. Advective heat transport through the fracture;
5. Conductive and advective heat transport through porous rock.

The continuously coupling between these aspects is governed by the stresses, pore pressures, temperatures, deformation and fractures of the rock.

3. Literature study

3.1 Introduction

This study focuses on the first three concepts of the THM fracture problem, being the fracture mechanics and the fluid flow through the fractures and the porous media. The function of this literature study is first of all to provide an overview of the available theory describing these concepts and providing insight into the coupling between them. Secondly, it discusses the fracture models and mixture analysis that are already available in Diana FEA software, as the new code that will be written for the simulation of the fluid flow through fractured rock will function as an addition to previously existing mixture analysis and material models in Diana.

3.2 Theory

For the outline of this section, three main subdivisions have been identified. First of all, the (classic) fracture mechanics is dealt with, discussing both linear elastic fracture mechanics as well as elastoplastic fracture mechanics. Secondly, the concept of smeared cracking is described, thereby also discussing its computational aspects. Next, the relevant laws and physical quantities governing the fluid flow through the porous, fractured media are discussed.

3.2.1 Fracture mechanics

Fracture-dominant failure in rock is related to highly localised plasticity. Fracture mechanics deals with why, how and when these points of highly localised plasticity occur in the rock leading to the initiation and propagation of cracks. Several approaches and methods have been developed over the years. The purpose of this section is to provide some insight into the fundamental theories necessary for the understanding of crack initiation and propagation in rock structures. The next sections, therefore, deal with the main methods that are grouped under the 'classical fracture mechanics'.

Classical fracture mechanics

Classical fracture mechanics starts with the concept of a single, ideal flat, perfectly sharp crack and the crack tip displacement is subdivided into three basic modes (Atkinson and Meredith, 1987, Janssen and Wanhill, 2004):

1. Mode I: tensile/opening mode;
2. Mode II: in-plane shear/sliding mode;
3. Mode III: anti-plane shear or tearing mode.

Superposition of these three modes can be used to describe a simple, general case of crack deformation. See Figure 3.1 for the illustration of the three fracture modes.

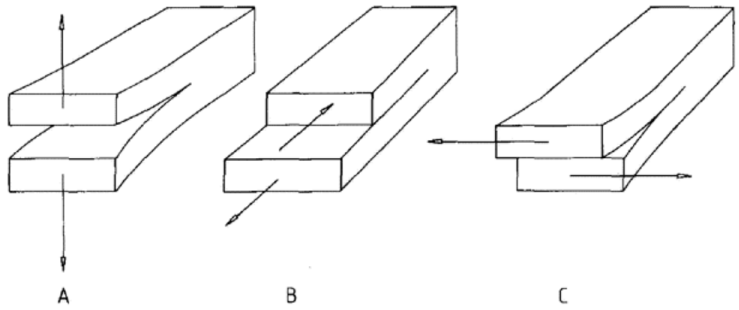

Figure 3.1: The three basic modes of tip displacement, where A corresponds to Mode I, B to mode II and C to mode III (Atkinson and Meredith, 1987).

The classical fracture mechanics approach (ideal, atomically sharp cracks behaving linear elastically) provides a suitable representation of cracks at a microscopic level. Nonetheless, at a more macroscopic level of study, for example, when considering fractured rock, the cracking shows more complex behaviour. Initially, upon loading, microcracks are formed. When loading is increased, the intensity of the microcracking also increases, and the behaviour in the crack tip becomes non-linear. Microcracks start linking in this non-linear zone resulting in the macrocrack extension. This zone is known as the process zone. The macrocracking propagates by taking with it microcracks and damage in the process zone. If the process zone is relatively small compared to the dimension of the cracked body, the assumption of linear elastic behaviour will still be valid. However, if the size of this plastic process becomes larger, then the application of non-linear elastic fracture mechanics is required.

The next sections deal with two different approaches: Linear Elastic Fracture Mechanics (LEFM) and Elastic-Plastic Fracture Mechanics (EPFM). Each approach is subsequently divided into two separate sub-methods defining crack criterion and parameters governing crack initiation and propagation. The different approaches and derivation of the criteria will be elaborated on in more detail in the coming sections.

Linear Elastic Fracture Mechanics (LFEM)

LEFM can be used to describe crack initiation and propagation in elastic material, having no or a limited plastic region (process zone) in the crack tip. The applicability of the LFEM approach depends on the size of the process zone compared to the smallest critical dimension of the structure. The critical dimension can be the length of the crack itself or possibly smaller; the distance from the true crack tip to the nearest free surface or joint, where the true crack tip is located at the end of the process zone indicating the beginning of the stress-free, true crack (see Figure 3.2).

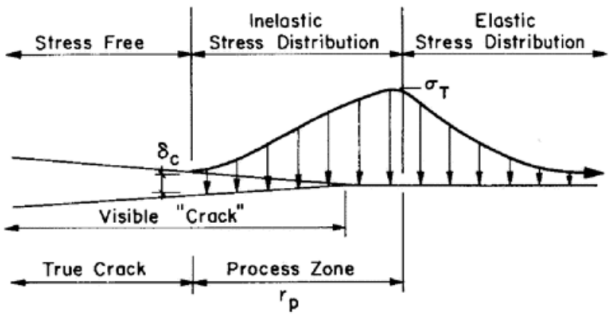

Figure 3.2: Illustration of a true crack consisting of a process zone and an effective crack (Atkinson and Meredith, 1987).

Two crucial parameters in the fracture mechanics are the stress intensity parameter K, and the stress extension force/strain energy release rate G. The stress intensity factor is the magnitude of crack tip stress field, for a particular mode (I, II or III), in a homogeneous linear elastic material. The crack extension force is more of a global parameter and is defined as the loss of energy per unit of new crack separation area formed during an increment of crack extension. It is therefore an energy release rate with respect to length and not time. These fracture mechanics parameters form the basis of the two crack propagation approaches in LEFM: The Stress Intensity approach and The Energy Balance approach.

The Stress Intensity Approach

Figure 3.3 shows the coordinate frame for the analysis of linear elastic stress tip field around a tensile mode I crack.

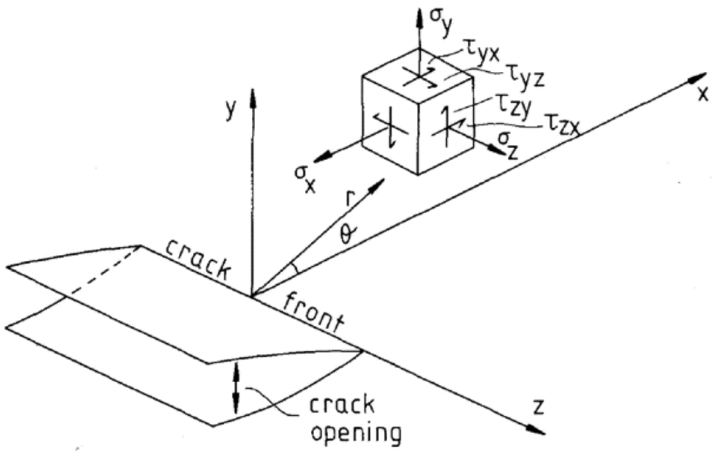

Figure 3.3: Coordinate frames for the analyses of linear elastic stress tip fields (Atkinson and Meredith, 1987). Cartesian (xyz) and polar (r, θ, z) coordinates are shown at the crack tip front.

For mode I, the stresses close to the crack tip are given by (Atkinson and Meredith, 1987)

$$\sigma_x = \frac{K_I}{(2\pi r)^{1/2}} \cos\frac{\theta}{2}(1 + \sin\frac{\theta}{2}\sin\frac{3\theta}{2}) \tag{3.1}$$

$$\sigma_y = \frac{K_I}{(2\pi r)^{1/2}} \cos\frac{\theta}{2}(1 - \sin\frac{\theta}{2}\sin\frac{3\theta}{2}) \tag{3.2}$$

$$\tau_{xy} = \frac{K_I}{(2\pi r)^{1/2}} \cos\frac{\theta}{2}\sin\frac{\theta}{2}\sin\frac{3\theta}{2} \tag{3.3}$$

where K_I is the magnitude of the crack tip stress field for mode I and can be defined as

$$K_I = lim[\sigma_y(2\pi r)^{1/2}]\text{as r} \rightarrow \text{on}\theta = 0 \tag{3.4}$$

with σ_y being the tensile stress normal to the crack plane. A similar expression can be obtained for the crack intensity for modes II and III (K_{II} and K_{III} respectively). The material property governing the fracture is stated as the critical stress intensity K_c. This critical stress intensity, also known as the fracture toughness, can thus be used to predict failure by adhering to the following fracture condition for crack mode I

$$K_I \geq K_{Ic} \tag{3.5}$$

The approach can be summarised according to the following key points (Atkinson and Meredith, 1987):

1. Crack extension starts at the crack tip and propagates in a radial direction;
2. Crack extension starts in a plane normal to the direction of the greatest tension at θ_0 (see Figure 3.3) such that $\tau_{r\theta} = 0$
3. Crack extension begins when K reaches a critical, material constant value K_c.

The Energy Balance Approach

Griffith (1921) was the first to define the crack criterion based on the 'theorem of minimum energy', which states that the equilibrium state of an elastic solid body, deformed by surface forces, is such that the potential energy of the whole system is at a minimum value. To create a crack, work must be done against the cohesive forces between the molecules on either side of the crack. This work is defined as the potential surface energy. Thus if the application of surface forces deforms an elastic body, the sum of the potential energy resulting from these forces is diminished by the formation of cracks, until an equilibrium state is reached. In other words, the energy balance condition (see Equation (3.6)) states that crack growth will occur when the energy available for crack extension (potential energy) due to an increase in forces and strains is larger than the energy required (crack resistance) to break the cohesive bonds between the molecules on either side of the crack (Atkinson and Meredith, 1987, Janssen and Wanhill, 2004). By balancing the potential energy available with the crack resistance the crack extension condition can be written as

$$\frac{dU_p}{da} > \frac{dU_\upsilon}{da} \tag{3.6}$$

where dU_p = The change in potential energy due to cracking, dU_υ = The change in surface energy due to cracking, and a = The distance along the crack length

The left-hand side of Equation (3.6) equals the decrease in potential energy if the crack would extend over a length da. The right-hand side represents the increase in surface energy during that same crack extension. The energy available per increment of crack extension has been defined as G, the energy release rate. The energy required per

increment of crack extension is defined as R, the crack resistance. Rewriting Equation (3.6) this results in the following extension condition (Janssen and Wanhill, 2004):

$$G > R \tag{3.7}$$

The energy release rate varies at a distance from the crack tip. Crack extension occurs in the direction along which R possesses a minimum value and G reaches a critical, material value (G_c). The critical energy release rate G_c as a material-specific parameter is related to the fracture toughness K_c.

Elastic-Plastic Fracture Mechanics (EPFM)

For brittle materials, and thus brittle cracking, it is assumed that the process zone (see Figure 3.2) is non-existent or insignificantly small compared to the critical dimensions of the structure. If this is the case, the LEFM can be used to describe crack initiation. Nonetheless, there are also classes of material which behaviour is categorised as ductile. The ductile behaviour results in a process zone that is too large compared to the critical dimensions of the structure in order for the material to be described by the LFEM. Another approach, which is better suited to deal with ductile material, however limited, is the Elastic-Plastic Fracture Mechanics (EPFM).
The EPFM can model the initiation of cracks (using one or two parameters similar to the ones used in the LEFM) in non-linear elastic materials, and to a limited amount, ductile materials. Within the EPFM, two main approaches can be identified: the J integral approach and the Crack Opening Displacement (COD) approach (Janssen and Wanhill, 2004). These two approaches will be described in the following sections.

J integral approach

The first primary approach in the EPFM is the J integral approach. The J integral is introduced as a parameter in fracture mechanics when the contribution of a non-linear elastic or inelastic process in the crack tip region is significantly large. J can be seen as the non-linear elastic equivalent of G and is therefore also defined as the decrease in potential energy per increment of crack extension. In the case of linear elastic stress-strain behaviour, J is even identical to G. J can either be derived based on the energy description (analogous to G) or it can be evaluated as a line integral along an arbitrary path surrounding the crack tip (Atkinson and Meredith, 1987, Janssen and Wanhill, 2004).

The definition J suggests that there is a critical value of J, J_c, at which crack extension is initiated. Thus, J values can be compared to J_c values (characteristic for certain material) enabling fracture mechanics analysis to be carried out. This approach is very similar to the energy balance approach in the LEFM.

Crack Opening Displacement (COD) approach

The second primary approach in the EPFM is the Crack Opening Displacement (COD). The reasoning behind the COD approach is as follows (Janssen and Wanhill, 2004): The stresses and the strain in the vicinity of the crack are responsible for failure. At crack tips, stresses exceed the yield strength, and therefore, plastic deformation occurs. It is argued that the stress at the crack tip always reaches the critical value. Thus the plastic strain in the crack tip region is the controlling factor of the crack. A measure of the amount of plastic strain at the crack tip is the opening of the crack flanks close to the tip. The COD at the initial crack tip is known as the Crack Tip Opening Displacement (CTOD). This CTOD represents finite displacement at the original crack tip, which is the result of an initially sharp crack that has been blunted due to plastic deformation (see Figure 3.4. It is assumed that at the onset of crack initiation, the CTOD has a critical value, which is material-specific and can therefore be used as a fracture criterion.

Several methods have been developed to determine the CTOD of cracks. In the case of LFEM, the CTOD can be related to the crack tip intensity or the strain energy release rate. A relationship between the J integral and the CTOD can also be expressed.

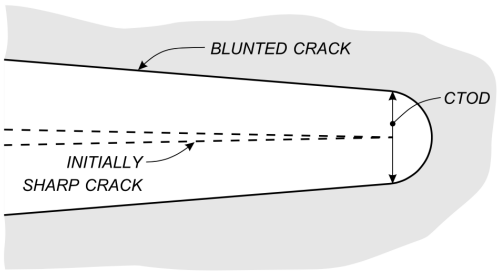

Figure 3.4: Crack tip opening displacement (Janssen and Wanhill, 2004).

An outline of the different methods that are grouped under either LEFM or EPFM is given in Figure 3.5. The modelling of crack initiation and propagation according to either one of these methods requires a discrete representation of cracks since it considers the occurrence of highly localised plasticity. A different approach for the simulation of fractures is the smeared crack concept. This concept and its computational aspects are discussed in the next section.

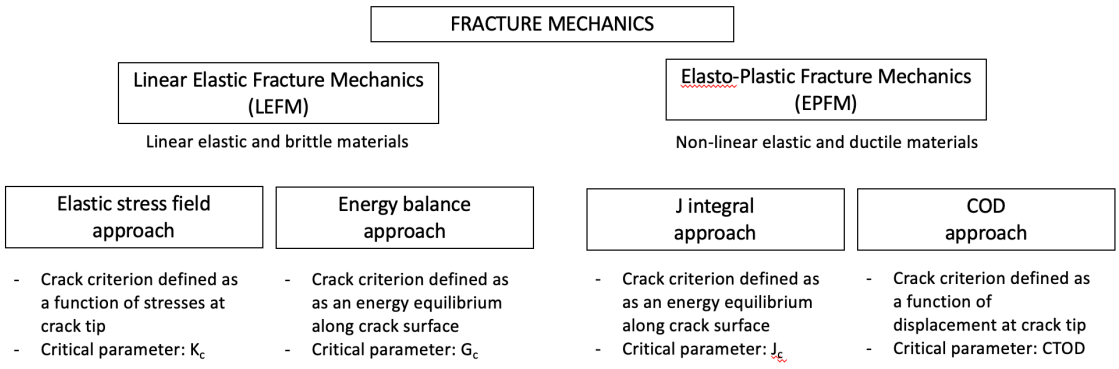

Figure 3.5: An overview of a subdivision of the main fracture mechanics approaches.

3.2.2 Smeared crack concept

A fractured rock mass can either be modelled as a network of discrete fractures (DFN concept or discontinuum approach) or as a smeared rock concept (continuum approach). The choice for either one of the two should consider the scale of the fractures with respect to the characteristic length of the structure that is evaluated. The DFN concept is a discrete approach, which considers fluid flow in fractured rock mass through a system of connected fractures, where the fractures are represented by discrete elements, or it is assumed that the rock is assembled of separate blocks, delimited by the fracture. The fracture is modelled as a single, true discontinuity. In the case of a smeared crack concept, the fractured medium, which includes the intact rock and the fractures, is considered to behave like a continuum, where the actual stresses and strain are averaged over a specific representative volume. According to this approach, a fracture is simulated by altering the physical and mechanical properties of the material. The smeared crack model thus expresses the cracked rock as a material with equivalent anisotropic continuum properties (Taghipoor et al., 2020).

Both models are capable of describing thermo-hydro-mechanical coupled processes using numerically based methods. The discontinuum approach, however, can characterise the rock and fractures more explicitly, as it is better capable of modelling small-scale fracture problems and thus more accurately simulating in-situ behaviour. The continuum approach, on the other hand, is better capable of simulating fracture branching, rotation and representing multiple cracks in non-predetermined directions. Even though a discrete approach might be more suited to represent the discrete nature of a crack, it also poses some computational difficulties. For example, fracturing increases the number of nodes and changes the connectivity of mesh elements (Taghipoor et al., 2020). This results in additional challenges for the automisation of the modelling approach. It can, therefore also, demand more computational efficiency and time for large scale reservoir simulations (Gan and Elsworth, 2016). For that reason, for the remaining part of this study, only the continuum model approach is considered, and it is assumed that the reservoir rock mass under consideration can be described to behave like a continuum.

Within the smeared crack concept, there is a subdivision with regards to computational aspects of the fracture orientation modelling. It is subdivided into three categories: fixed, multi-directional fixed crack or a rotating crack (Rots, 1988). These three categories will be discussed in more detail the following sections. However, before doing so, the fracture model of the smeared crack concept is explained.

Fracture model

The stress-strain law for smeared cracking in a traditional sense was set-up with reference to the *nst*-axes, which is set-up aligned with the crack. In this coordinate system n refers to the direction normal to the crack and s and t to the directions tangential to the crack, corresponding to crack modes I, II and II respectively (see Figure 3.6). The general stress-strain relation in the crack coordinate system is defined in Equation (3.8) with nine independent stiffness moduli. In the earliest versions of the application of this stress-strain relationship, the moduli are set equal to zero upon the formation of cracks. This is a rudimental approximation as it assumes that cracks are not at all capable of transmitting tension, which in reality is not the case. Furthermore, the abrupt switch from an initial isotropic linear-elastic law to an orthotropic law with stiffness moduli equal to

zero implies a strong discontinuity and results in computational difficulties. Therefore, researchers implanted reduction factors to account for the reduction in mode I stiffness μ and shear stiffness β upon cracking. This adjustment resulted in the orthotropic law according to Equation (3.9) (for a 2D configuration), where E is Young's modulus, ν is Poisson's ratio (Rots, 1988).

For these traditional stress-strain relations, the strain-vectors in Equations (3.8) and 3.9 represent the total strain of the cracked continuum, which includes the crack strain as well as the strain of the supposedly non-fractured rock material which is present between the cracks.

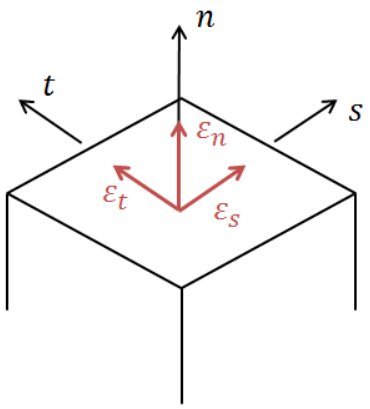

Figure 3.6: Illustration of crack plane and strain with the corresponding coordinate system (Rots, 1988).

$$\begin{bmatrix} \sigma_{nn} \\ \sigma_{ss} \\ \sigma_{tt} \\ \sigma_{ns} \\ \sigma_{st} \\ \sigma_{tn} \end{bmatrix} = \begin{bmatrix} E_{nn} & E_{ns} & E_{nt} & 0 & 0 & 0 \\ E_{ns} & E_{ss} & E_{st} & 0 & 0 & 0 \\ E_{nt} & E_{st} & E_{tt} & 0 & 0 & 0 \\ 0 & 0 & 0 & G_{ns} & 0 & 0 \\ 0 & 0 & 0 & 0 & G_{st} & 0 \\ 0 & 0 & 0 & 0 & 0 & G_{nt} \end{bmatrix} \begin{bmatrix} \varepsilon_{nn} \\ \varepsilon_{ss} \\ \varepsilon_{tt} \\ \gamma_{ns} \\ \gamma_{st} \\ \gamma_{tn} \end{bmatrix} \tag{3.8}$$

$$\begin{bmatrix} \sigma_{nn} \\ \sigma_{tt} \\ \sigma_{nt} \end{bmatrix} = \begin{bmatrix} \frac{\mu E}{1-\nu^2\mu} & \frac{\nu\mu E}{1-\nu^2\mu} & 0 \\ \frac{\nu\mu E}{1-\nu^2\mu} & \frac{E}{1-\nu^2\mu} & 0 \\ 0 & 0 & \frac{\beta E}{2(1+\nu)} \end{bmatrix} \begin{bmatrix} \varepsilon_{nn} \\ \varepsilon_{tt} \\ \gamma_{nt} \end{bmatrix} \tag{3.9}$$

A disadvantage of this total strain representation (see Equations (3.8) and (3.9)) is that some crack laws, which are based on the formulation of solely the crack strain, cannot be transparently incorporated using this model. A solution to this problem was introduced by decomposing the total strain into a crack strain $\Delta\varepsilon^{cr}$ and a strain corresponding to the solid material in between the cracks $\Delta\varepsilon^{co}$ (see Equation (3.10)). This decomposition is thereby a small movement in the direction of the discrete crack concept, where the modelling of the crack is performed entirely separate from the solid material. In the case of linear elastic material behaviour, $\Delta\varepsilon^{co}$ is equal to the elastic strain ($\Delta\varepsilon^{e}$), however, for non-linear elastoplastic material $\Delta\varepsilon^{co}$ can also include, for example, plastic or thermal strains.

$$\Delta\varepsilon = \Delta\varepsilon^{cr} + \Delta\varepsilon^{co} \tag{3.10}$$

When the strain is decomposed into $\Delta\varepsilon^{cr}$ and $\Delta\varepsilon^{co}$, the global crack strain vector in a 3D-configuration, which is aligned with the global x,y,z - axes reads

$$\Delta\varepsilon^{cr} = \begin{bmatrix} \Delta\varepsilon_{nn}^{cr} & \Delta\varepsilon_{yy}^{cr} & \Delta\varepsilon_{zz}^{cr} & \Delta\gamma_{xy}^{cr} & \Delta\gamma_{yz}^{cr} & \Delta\gamma_{zx}^{cr} \end{bmatrix}^T \tag{3.11}$$

Furthermore, a local crack strain vector can also be identified (Equation (3.12)). This local vector is aligned with the local *nst*-coordinate system, where ε_{nn}^{cr} corresponds to the normal mode I crack strain and γ_{ns}^{cr} and γ_{nt}^{cr} to the mode II and III shear crack strains respectively.

$$\Delta e^{cr} = \begin{bmatrix} \Delta\varepsilon_{nn}^{cr} & \Delta\gamma_{ns}^{cr} & \Delta\gamma_{nt}^{cr} \end{bmatrix}^T \tag{3.12}$$

The relation between the local and global crack strains is established according to Equation (3.13), where T is the transformation matrix representing the crack orientation with respect to the global system, ε^{cr} is the global crack strain and e^{cr} the local crack strain

$$\Delta\varepsilon^{cr} = [T]\Delta e^{cr} \tag{3.13}$$

Computational aspects

Fixed crack

The fixed crack approach assumes that the local crack axes remain unaltered throughout the analysis and the crack orientation is therefore determined upon initiation, i.e. the [T] matrix is fixed. The main features of the fixed crack computational approach are:

1. Maximum of three orthogonal cracks in one point;
2. Crack is defined if the tensile strength is exceeded;
3. Crack orientation is fixed upon initiation;
4. Permanent memory of damage orientation.

Multi-directional fixed crack

The multi-directional fixed crack further builds upon the concept of strain decomposition, whereby individual contributions of multi-directional cracks simultaneously occurring at one point are considered (see Equation (3.14)). Each individual crack strain increment contributes to the global crack strain ε^{cr}. A new crack is initiated when the tensile stress exceeds the tensile strength, and the direction of the principal stress exceeds a certain threshold angle with respect to the orientation of the already existing cracks.

$$\Delta\varepsilon^{cr} = \Delta\varepsilon_1^{cr} + \Delta\varepsilon_2^{cr} + ... \tag{3.14}$$

Besides this, each crack is also assigned a local crack strain vector e_i^{cr} and transformation matrix T_i, which are assembled into multi-directional crack vectors and matrices according to Equation (3.15) and (3.16). This yields the relation between local and global crack strain according to Equation (3.17).

$$\Delta\hat{e}^{cr} = \begin{bmatrix} \Delta e_1^{cr} & \Delta e_2^{cr} & ..... \end{bmatrix}^T \tag{3.15}$$

$$\hat{T} = \begin{bmatrix} T_1 & T_2 & ..... \end{bmatrix}^T \tag{3.16}$$

$$\Delta\varepsilon^{cr} = \hat{T}\Delta\hat{e}^{cr} \tag{3.17}$$

The main features of the multi-direction fixed crack approach can be summarized as following:

1. Multiple active cracks occurring simultaneously;
2. Crack is defined if the tensile strength and threshold angle are exceeded;
3. Crack orientation is fixed upon initiation;
4. Permanent memory of damage orientation.

Rotating crack

The main point of criticism with regards to the fixed single crack approach is the misalignment between the axes of principal stress and the fixed crack axes, as principal stresses tend to sometimes rotate after crack formation. The rotating crack approach eliminates this discrepancy as it forces coaxiality between the principal axes and crack axes by co-rotating the crack axes with the principal axes. Crack directions are therefore not fixed upon initiation, but instead are updated at the beginning of each incremental stage, so the axes of material orthotropy correspond with the principal axes, i.e. [T] is not fixed but updated continuously.

The following features describe the rotating crack approach:

1. Maximum of three orthogonal cracks in one point;
2. Crack is defined if the tensile strength is exceeded;
3. Crack orientation updated continuously at each stage of the incremental process;
4. No permanent memory of crack orientation, but the crack-opening history (maximum crack strain ever experienced) is kept as status parameter.

3.2.3 Flow through porous, fractured media

The following sections deal with the main concepts related to flow through porous, fractured media. Because accurately describing the permeability of a porous, fractured medium can be a difficult task, especially in the case of a THM coupled process, for simplifying means, the flow model is often subdivided into two: matrix flow and fracture flow, with both having there own contribution to the permeability of the system. Therefore, after having discussed the basics of Darcy's law, two sections deal with the description of matrix and fracture permeability separately.

Darcy's law

The fluid flow rate through a porous (fractured) medium can be described by Darcy's law, which is written as

$$q = -\frac{k}{\mu}\nabla\phi \tag{3.18}$$

where k is the permeability of the medium, μ is the fluid viscosity and ϕ is the pore pressure potential.

Permeability is an intrinsic property of a rock mass determined on its geometry. It thereby deviates from the hydraulic conductivity, which is also a function of the fluid viscosity, density and gravitational acceleration (Chen et al., 2007). The hydraulic conductivity is defined as a function of the permeability according to Equation (3.19), where ρ is the fluid density, g is the gravitational acceleration and μ is the fluid viscosity. In literature different notations for the intrinsic permeability and hydraulic conductivity are used. In this study, the permeability will be referred to with a small k, and for the hydraulic conductivity a capital K will be used.

$$K = \frac{\rho g}{\mu} k \tag{3.19}$$

Fluid viscosity

The fluid flow rate q through the rock is a function of the fluid viscosity μ. The viscosity of pure water is temperature-dependent: As temperature increases, the viscosity decreases (Lyons and Plisga, 2011). In geothermal energy systems, cold water is injected in the injection well, and hot water is extracted from the production well. Thus, as the water flows through the reservoir rock, its temperature increases, and thereby, the viscosity decreases. The viscosity of water can be defined as a function of temperature (Salimzadeh et al., 2018), where T_f is the fluid temperature in Kelvin

$$\mu = e^{(-52.643 + \frac{3703.6}{T_f} + 5.866 \cdot \ln(T_f) - 5.88 \cdot 10^{-29} \cdot T_f^{10})} \tag{3.20}$$

This relation between the fluid viscosity and temperature will result in a viscosity of $\mu \approx 0.001\ Pa \cdot s$ for T_f = 20°C = 293.15 K.

Permeability tensor

In a 3D-configuration the permeability tensor can be represented by a symmetric, positively defined 3x3 matrix (see Equation (3.21)). The diagonal components represent the dependence of the flow rate on the pressure difference in the same direction, whereas the off-diagonal components represent the dependence of the flow rate on the pressure difference in the orthogonal directions.

$$k = \begin{bmatrix} k_{xx} & k_{xy} & k_{xz} \\ k_{xy} & k_{yy} & k_{yz} \\ k_{xz} & k_{yz} & k_{zz} \end{bmatrix} \tag{3.21}$$

Matrix permeability

Generally speaking, the permeability of a porous medium can be expressed as the product of a pore geometry function G and a porosity function $f(n)$

$$k = Gf(n) \tag{3.22}$$

Several approaches have been developed to more specifically define this permeability-porosity relationship. One of the most well-known equations describing the relationship

between the permeability and the properties of the pores is the Kozeny-Carman equation. The relation was first proposed by Kozeny (1927) and later modified by Carman (1961), yet the authors never published together. The Kozeny-Carman law expresses the permeability of a porous medium in the following form (Latief and Fauzi, 2012)

$$k = \frac{n^3}{c\tau^2 S^2} \tag{3.23}$$

where n is the porosity, S is the surface area per unit volume, τ is the tortuosity and c is the so-called Kozeny constant, which depends on the geometry of the porous medium.

Fracture permeability

Cubic law

The simplest model of fluid flow through a single fracture is the parallel plate model, which assumes the fracture to consists of two smooth, parallel plates separated by the fracture aperture. Snow (1969) was the first one to show that the flow through a fracture under this assumption can be described as a cubic function of its aperture (b), hence the 'cubic-law'. The cubic law defines the transmissivity (T) of the fracture as a cubic function of the aperture and fracture width (w). The transmissivity is the product of the permeability (k) and the area (A), and the permeability of a single fracture is consequently defined as a quadratic function of the fracture aperture (b), see Equations (3.24) and (3.25) below.

$$T = kA = \frac{wb^3}{12} \tag{3.24}$$

$$k = \frac{b^2}{12} \tag{3.25}$$

The cubic law assumes a laminar fluid flow through a pair of smooth parallel plates with infinite lengths. The mechanical aperture gives the distance between these plates. However, for natural rock fractures, which have finite dimensions, rough walls and infill material, it is not appropriate to directly implement Equation (3.25) to describe the permeability of the fracture, where b is equal to the mechanical aperture. In order to account for this inconsistency with regards to the initial assumptions, the hydraulic aperture b^* is introduced to replace the mechanical aperture b (Zimmerman and Bodvarsson, 1996). The hydraulic aperture is generally smaller than the mechanical aperture due to fracture roughness and infill. Some studies introduce a factor (ξ) to account for the difference between the hydraulic and mechanical aperture (Chen et al., 2007). In that case, Equation (3.25) can be rewritten as

$$k = \xi \frac{b^2}{12} \tag{3.26}$$

Over the years, many empirical relationships between the hydraulic and mechanical aperture of rocks have been found. A collection of these relations can be found in Table 3.1. This collection has been put together by Chen and Zhou (2011) based on the work of many others.

Table 3.1: Overview of a collection of empirical relations between the hydraulic (b*) and mechanical aperture (b) (Chen and Zhou, 2011).

Authors	**Expression**
Lomize (1951)	$b^* = b(1.0+6.0(e/b)^{1.5})^{-1/3}$
Louis (1971)	$b^* = b(1.0+8.8(e_m/D_H)^{1.5})^{-1/3}$
Patir & Cheng (1978)	$b^* = b(1-0.9)exp(-0.56/C_v))^{1/3}$
Barton, et al. (1985)	$b^* = b^2 JRC^{-2.5}$
Olsson & Barton (2001)	$b^* = b^2 JRC_0^{-2.5}$ $\delta \leq 0.75\delta_p$ $b^* = b^{1/2} JRC_{mob}$ $\delta \geq \delta_p$

Symbol definition: e is the absolute asperity height, e_m the average asperity height, D_H the hydraulic radius, C_v the variation coefficient of b, JRC the Joint Roughness Coefficient, JRC_0 the initial value and JRC_{mob} the mobilized value, δ the shear displacement and δ_p the peak shear displacement.

One example of an empirical relation between the mechanical and hydraulic aperture is defined by Barton et al. (1985) (see Table 3.1 above). The relation between the two apertures is described using the Joint Roughness Coefficient (JRC), see Equation (3.27). The relation is defined for the aperture in microns. The JRC is a dimensionless parameter, which typically ranges from 0 - 15 (and to a maximum of 20), where a low JRC represents very smooth joint walls, and a high JRC indicates a rough surface (Barton et al., 1985).

$$b^* = b^2 JRC^{-2.5} \tag{3.27}$$

Strain-dependent permeability

Many models have been proposed for the formulation of either a stress- or a strain-dependent hydraulic conductivity of permeability tensor of a fracture network. Chen and Zhou (2007, 2011) formulate both stress- as well as strain-dependent hydraulic conductivity tensors. In comparing the two, it is stated that a strain-dependent formulation of the hydraulic permeability has the advantage of being able to account form more complex loading situations in comparison to stress-dependence as the formulation enables analysis to include the effect of material non-linearity in the hydro-mechanical coupling process.

It is approximately valid that the aperture, or the average crack width over the crack surface, is a function of the crack normal strain ε_n and the crack spacing (s) (Chen et al., 2007 Chen and Zhou, 2011 Vecchio and Collins, 1986):

$$\Delta b = \Delta\varepsilon_n \, s \tag{3.28}$$

Using Equation (3.28) Chen et al. (2007) proposes the following formulation for the strain-dependent hydraulic conductivity of the f_{th} set of fractures

$$k = k_{f0}(1 + \frac{s_{f0}}{b_{f0}} \Delta\varepsilon_{nf})^3 \tag{3.29}$$

where k_{f0}, s_{f0} and b_{f0} are the initial hydraulic conductivity, spacing and aperture of the f_{th} set of fractures respectively. Chen et al. (2007) showed that the hydraulic conductivity could be rather sensitive to $\frac{s_{f0}}{b_{f0}}$ and estimates should therefore be carefully developed.

According to Vecchio and Collins (1986), the mechanical aperture can be calculated as a function of the crack normal strain according to Equation (3.28), where s is the spacing for the particular set of cracks that depends on the direction angle θ of the set of cracks. The

crack spacing is estimated based on the direction of the crack and crack control parameters of the medium, see Equation (3.30). Vecchio and Collins (1986) give this description for the calculation of the crack width in concrete, where s_{mx} and s_{my} are indicators of the crack control characteristics of the x-reinforcement and y-reinforcement respectively.

$$s_\theta = \frac{1}{\frac{sin\theta}{s_{mx}} + \frac{cos\theta}{s_{my}}} \tag{3.30}$$

3.3 Fracture and fluid flow simulation in Diana

The next sections deal with the basics of the fracture material models, being the Total Strain crack model ad the Multi-Directional fixed crack model, and the mixture analysis that is available in Diana (DIANA FEA bv, 2019).

3.3.1 Fracture models

Cracks can be modelled by means or discrete cracking or smeared cracking using DIANA FEA software. In the case of the smeared cracking method, Diana supports five different material models of which two are non-concrete/masonry specific. These two are:

1. Total Strain crack model;
2. Multi-directional fixed crack model;

The next two sections deal with the implementation of the Total Strain crack model and the Multi-directional fixed crack model. After that, the two material models are discussed and reflected on their applicability and limitations.

Total Strain crack model

The constitutive model of the Total Strain crack model has been developed in Diana along the lines of the Modified Compression Field Theory, which has initially been proposed by Vecchio and Collins (1986). The Modified Compression Field Theory has been developed for reinforced concrete in torsion and shear. In contrast to the original compression-field theory, which ignores tension in cracked concrete, the modified theory does take the tensile stresses between cracks into account. In both the models, the cracked concrete is treated as new material having its own stress-strain characteristics. Overall relationships of the concrete are formulated in terms of average stresses and strains (Vecchio and Collins, 1986). Furthermore, the Modified Compression Field Theory assumes the coincidence of the principal stress and strain axes. The Total Strain crack model in Diana can employ the fixed and rotating crack model.

The basic concept of the Total Strain crack model is that the stress-strain relationships are evaluated in the direction of the principal strain vector ε_{xyz} and that the material characteristics are defined as a 1D stress-strain relation in tension and in compression. The strain vector in the element coordinate system (ε_{xyz}) is updated with the strain increment ($\Delta\varepsilon_{xyz}$) according to Equation (3.31). In the case of the rotating crack concept, the crack directions (nst) are continuously rotating with these directions according to Equation (3.32), where the strain transformation matrix [T] depends on the current principal strain vector ($\varepsilon_{xyz}^{t+\Delta t}$), see Equation (3.33). Figure 3.7 illustrates the rotation of the crack axis with respect to the element coordinate system.

If the crack is assumed to be fixed, then [T] is determined upon crack initiation and will remain constant throughout the whole analysis. In that case, Equation (3.33) does not apply. The strain transformation matrix is determined by calculating the eigenvectors of the strain tensor with the Jacobi method. The eigenvectors are stored in the rotating matrix R.

$$\varepsilon_{xyz}^{t+\Delta t} = \varepsilon_{xyz}^{t} + \Delta\varepsilon_{xyz}^{t+\Delta t} \tag{3.31}$$

$$\varepsilon_{nst}^{t+\Delta t} = [T]\,\varepsilon_{xyz}^{t+\Delta t} \tag{3.32}$$

$$[T] = T(\varepsilon_{xyz}^{t+\Delta t}) \tag{3.33}$$

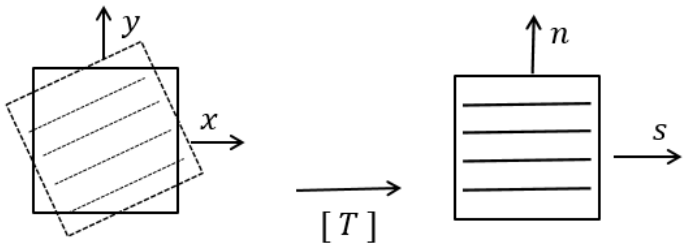

Figure 3.7: Rotation of the crack axis with respect to the element coordinates system.

The constitutive model in the crack coordinate system is given by Equation (3.34). And the updated stress vector in the element coordinate system is calculated according to Equation (3.35), where [T] is given by the current strain transformation matrix (Equation. (3.33)) in the case of the rotating crack concept, and [T] is determined upon the incipient of cracking for the fixed crack concept.

$$\sigma_{nst}^{t+\Delta t} = \sigma(\varepsilon_{nst}^{t+\Delta t}) \tag{3.34}$$

$$\sigma_{xyz}^{t+\Delta t} = [T]^{T}\,\sigma_{nst}^{t+\Delta t} \tag{3.35}$$

Multi-directional fixed crack model

The basics of the Multi-directional fixed crack model have already been described in Section 3.2.2, according to Rots (1988). The fundamental concept of the Multi-directional fixed crack model is the decomposition of the total strain into an elastic strain and a crack strain (see Equation (3.36)). This decomposition allows for a more transparent manner of combining the crack model with other models that depend on the crack strain. Furthermore, the decomposition of the total strain also gives the possibility of modelling several cracks that simultaneously occur, i.e. at the same time and location (integration point). The concept of multiple cracks co-occurring thus assumes that a stress s_i and a strain e_i^{cr} exist in the nst-coordinate system for each crack, with i representing the specific crack number. A new crack is initiated when the tensile stress exceeds the tensile strength

and the direction of the potentially new crack exceeds a certain threshold angle α_{TD} with respect to the direction of the other crack(s) (see Figure 3.8).

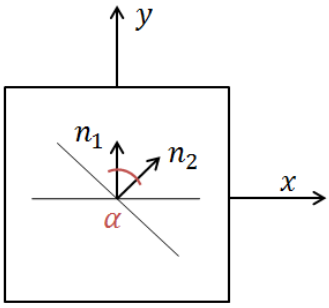

Figure 3.8: Illustration of the concept of two cracks occurring simultaneously (same time and location) with a threshold angle α DIANA FEA bv, 2019.

The vector e^{cr} assembles all the contributions of the individual cracks according to Equation (3.37), where $e_i^{cr} = [\varepsilon_{nn,i}^{cr}\ \gamma_{nt,i}^{cr}\ \gamma_{ns,i}^{cr}]$. The relationship between the global crack strain and the e^{cr} vector is given by Equation (3.38), where [T] is the assembled transformation matrix according to Equation (3.39). In the case of plane strain, the transformation matrix for crack i ($[T_i]$) is given by Equation (3.40), where $n^t = l_x, m_x, n_x$ is the normalized vector normal to the crack plane. As it concerns a multi-directional fixed crack model, $[T_i]$ is fixed upon initiation of crack i.

$$\varepsilon = \varepsilon^e + \varepsilon^{cr} \tag{3.36}$$

$$e^{cr} = \begin{bmatrix} e_1^{cr} & e_2^{cr} & \dots & e_i^{cr} & \dots & e_n^{cr} \end{bmatrix}^T \tag{3.37}$$

$$\varepsilon^{cr} = [T]e^{cr} \tag{3.38}$$

$$T = \begin{bmatrix} T_1 & T_2 & \dots & T_i & \dots & T_n \end{bmatrix} \tag{3.39}$$

$$T_i = \begin{bmatrix} l_x^2 & l_x l_y \\ m_x^2 & m_x m_y \\ n_x^2 & N_x n_y \\ 2l_x m_x & l_x m_y + l_y m_x \end{bmatrix} \tag{3.40}$$

Similar to the strain vector, a vector is assembled for the crack stress s^{cr} (see Equation (3.41)), where $s_i^{cr} = [\sigma_{nn,i}^{cr}\ \tau_{nt,i}^{cr}\ \tau_{ns,i}^{cr}]$. The relationship between the global stress and the stress vector s^{cr} is derived according to Equation (3.42), where [T] is given by Equation (3.39). This derivation gives rise to the assumption that the crack stresses are functions of the crack strains. Furthermore, it is assumed for computational purposes that there is no coupling between the occurring cracks. Thus the crack stresses are solely governed by the corresponding crack strain.

$$s^{cr} = \begin{bmatrix} s_1^{cr} & s_2^{cr} & \dots & s_i^{cr} & \dots & s_n^{cr} \end{bmatrix}^T \tag{3.41}$$

$$s^{cr} = [T]^T \sigma \tag{3.42}$$

Crack bandwidth

A common feature of smeared cracking models is their non-objectivity to the size of the elements when using regular continuum elements. A way to overcome this non-objectivity is by modifying constitutive relations and making them dependent on the mesh size by introducing a 'characteristic length' or 'crack bandwidth' (Oliver, 1989). Oliver proposes a direct characteristic length theory in order to define an expression of the otherwise rather intuitively employed crack bandwidth parameter, which is also applicable for irregular meshes having arbitrary crack directions. The basic idea of the theory is that the 'strain energy release rate' or 'fracture energy per unit area crack advance' G_f (see Section 3.2.1), which is a material property, is related to the energy dissipated per unit volume (g_c) in the continuum theory through the expression

$$g_c = \frac{G_c}{l^*} \tag{3.43}$$

where l^* is the characteristic length of the element or also referred to as the 'crack bandwidth'.

In smeared crack modelling the crack bandwidth (h_{cr}) is used to define the length of the fracture process zone, and it is thus related to the area or volume of the element. Two methods that can be applied in Diana to determine the crack bandwidth are (DIANA FEA bv, 2019):

1. Rots' element based method
2. Govindjee's projection method

Rots defined the crack bandwidth dependent on the size, shape and interpolation function of the finite element. According to Govindjee et al. (1995), the crack bandwidth is the projected length of the element onto the crack plane. It thereby does not only include the element size, but also includes the element ratio and the direction of the crack (DIANA FEA bv, 2019). Govindjee et al. (1995) derive a continuous definition of the crack bandwidth building on the theory proposed by Oliver (1989).

3.3.2 Mixture analysis

This section describes the mixture analysis that is available in Diana FEA software. In this particular context, mixture analysis means the simultaneous solution of deformation and pore pressures for the mixture of a fluid and a porous solid like soil or rock. It thus considers an extra degree of freedom in addition to the displacement (u) which can be specified as an input value in the form of a pore pressure potential (ϕ). The pore pressure potential can be split into a pore pressure (p) and a gravitational part and thus pore pressure can be determined using Equation (3.44), where ϕ is the pore pressure potential and $x_{init} - x_{ref}$ is the intial position vector, with $x = x_{init} + u$ (u being the displacement).

$$p = \phi + \rho_f g(x - x_{ref}) \tag{3.44}$$

Darcy's law relates the fluid flow in the porous media with the gradient in the pore pressure potential through the modified permeability k', see Equation (3.45). The modified permeability is a function of the permeability according to Equation (3.46), where μ is the dynamic viscosity.

$$q = k' \Delta\phi \tag{3.45}$$

$$k' = \frac{k}{\mu} \tag{3.46}$$

The modified initial permeability is a required input parameter for the mixture analysis in Diana. A single input value indicates isotropic permeability. Anisotropic permeability can be implied by introducing three (2D) or six (3D) terms. The mixture analysis also requires the initial porosity n_0. The porosity can be updated throughout the analysis if the porosity is specified as being deformation-dependent, i.e. as a function of the deformation gradient (see Equation (3.47)). Subsequently, the updated porosity can be used to determine the actual density.

$$n = 1 + \frac{n_0 - 1}{1 + det(F)} \tag{3.47}$$

with F being

$$F = det \nabla x \tag{3.48}$$

For mixture continuum elements, Diana supports a porosity- and a saturation-dependent permeability. The permeability is calculated accordingly

$$k' = k'_{rel,n}\, x\, k'_{rel,s}\, x\, k'_{init} \tag{3.49}$$

where $k_{rel,n}$ is a factor, which is a function of the porosity. This porosity dependence can be defined by the user preliminary to the analysis or determined according to the Kozeny-Carman law (Kozeny, 1927; Carman, 1961; Meijer, 1985; Latief and Fauzi, 2012). In the latter case, the relative permeability factor is expressed as

$$k_{rel} = \frac{n(\frac{n}{1-n})^2}{n_0(\frac{n_0}{1-n_0})^2} \tag{3.50}$$

If the porosity dependence of the permeability is defined in a user-specified diagram, Diana determines $k_{rel,n}$ utilising linear interpolation. The same holds for $k_{rel,s}$, which can also be defined in a user-specified diagram.

3.4 Conclusion

Theory

The purpose of the theoretical review is to provide a theoretical framework upon which the concept of a model allowing for the simulation of fracture-dependent mixture analysis can be built. The following main conclusions with regards to the model development were drawn based on the available theory:

- From a fracture mechanics point of view, it is arguably more appropriate to simulate fractures according to a discontinuum approach because of a crack's discrete nature, thereby following the lines of either a LEFM or EPFM approach depending on the mechanical behaviour of the material. However, when examining a THM fracture problem, adhering to a continuum approach could be considered to be suitable as well, as it can properly represent multiple cracks occurring simultaneously in non-predetermined directions. The smeared crack concept is furthermore also

favourable from a computational point of view as it is a more straightforward approach with regards to the automisation of the model.

- The fluid flow through a porous, fractured medium can be described by Darcy's law, whereby the permeability represents the permeability of the porous rock as well as the permeability of possible present fracture networks.
- A single fracture can be represented by two parallel plates separated by the fracture aperture. Fluid flow through this fracture can therefore be described through the cubic law, which assumes laminar fluid flow through a pair of smooth, parallel plates with infinite lengths.
- The cubic law forms the coupling link between the geomechanical response of the rock and the fluid flow as it leads to the definition of the fracture permeability as a function of the fracture aperture. The fracture aperture is subsequently defined as a function of the crack normal strain and a length parameter describing the width of the cracked material (when considering only crack mode I tensile opening) .

Fracture models and mixture analysis in Diana FEA software

The Diana software offers two different smeared fracture models: the Total Strain crack model and the Multi-directional Fixed crack model. Both these material models are considered to be smeared crack models, thus treating the cracked material as a continuum having anisotropic characteristics due to the presence of fractures. Concerning the computational aspects, the Total Strain Crack model can employ a fixed and rotating crack approach, whereas the Multi-directional Fixed crack model, employs, as its name suggests, the multi-directional fixed approach. Both the fixed and the rotating approach can simulate up to a limit of three orthogonal cracks in one point. From a physical point of view, the fixed approach appears more accurate and better suited at simulating in-situ behaviour as cracks are not expected to rotate due to a load or strain increment. However, from an engineering point of view, the rotating crack approach is more attractive as it ensures coincidence between the principal axes and crack axes. If no or limited rotation of the principal axes from the moment of crack initiation is expected, the rotating approach might be more convenient to employ than the fixed approach. Due to the monotonic loading conditions it is not expected that the differences between the rotating and the fixed approach will be very relevant with regards to the application of EGS.

The Multi-Directional Fixed approach allows for the simulation of multiple cracks occurring simultaneously in one point. The angle between the cracks is not constricted to 90° but instead depends on the defined threshold angle. Being able to simulate multiple cracks in one point might be more appropriate in some cases, however, when the coupling is made between the occurrence of cracks and the corresponding increase in permeability, it can be argued that the simulation of three orthogonal cracks is sufficient as the permeability is also limited to three orthogonal directions. Another important difference between the Total Strain Crack model and the Multi-direction Fixed Crack model is the decomposition of the total strain in an elastic strain and a crack strain in case of the latter. This decomposition allows for better and more transparent cooperation between the Multi-directional Fixed Crack model and other fracture-dependent models that require the definition of the separate crack strain.

The Diana code includes two different methods for estimating the crack bandwidth. When comparing the two definitions of the crack bandwidth, i.e. Rots' element based method and Govindjee's projection method, it can be argued that Govindjee's projection method might be better capable of defining the length of the fracture process zone as it does not only take into account the size of the element but also the direction of the cracks. This difference is of importance when non-uniform, elongated elements are used, and the direction of the fractures does not correspond with the main element axes. Furthermore, by taking into account the direction of the crack Govindjee's definition of the crack bandwidth shows similarities to the crack parameters (S_{mx} and S_{my}) as described by Vecchio and Collins (1986) in their modified compression field theory.

With regards to the mixture analysis, Diana can account for the coupling between deformations and changes in permeability for the porous medium, through the implementation of a porosity-dependent permeability. A similar approach could be incorporated for a fracture-dependent permeability, where the initial modified permeability is updated through a relative permeability factor, which depends on the aperture development of the cracks.

The derivation of the proposed model concept, based on the theory which has been outlined in this chapter, is described in a step-wise manner in the next chapter. Chapter 4 also includes a more practical description of the implementation of the model into the already existing Diana code through the creation of new subroutines, which form an extension to the mixture analysis in Diana.

4. Model concept and implementation

4.1 Introduction

In order to be able to simulate fluid flow through fractured rock, a new material model is created as a part of the Diana code. This model is capable of determining the direction and estimating the size of fractures based on the current stress state. Based on these fracture properties, it calculates the updated permeability of the rock material by means of a smeared crack approach. The material model will be further referred to as the fracture-dependent permeability model. It can be used in combination with smeared fracture models in Diana, such as the Total Strain crack model and the Multi-Directional Fixed crack model. These fracture models account for the strength and stiffness degradation of the rock due to the presence of fractures. By including the fracture-dependent permeability model in the description of the rock material, it is possible to simulate a mixture analysis in fractured rock.

This chapter explains how the framework of the fracture-dependent permeability model was established and implemented in the Diana code. First of all, Section 4.2 works through the derivation of the concept following the lines of the theory as described in Chapter 3. For the definition of the fracture-dependent permeability, two different methods are proposed. According to the first method, the permeability is updated in the presence of fractures by treating the rock mass a continuum, whereas the second method includes the effect of the crack by adding an extra fracture permeability. Section 4.3, provides an overview of how the new subroutines are linked to the previously existing mixture analysis in Diana, and describes the three subroutines (CRKPER, CRKDIR and CRKAPT) that have been written in order to accomplish a fracture-dependent permeability. The final Section (4.4) summarises and concludes on the model derivation.

4.2 Concept

The model concept proposes two different methods for defining the fracture-dependent permeability. Most of the steps in the definition of these two methods are the same. However, the essential difference between the two is that method 1 treats the medium as a continuum with fractures dependent properties, thereby expressing the change in permeability as an overall change in the permeability of the rock mass. Method 2, on the other hand, separately takes the effects of the fractures into account by adding a fracture permeability to the initial permeability of the rock mass.

The derivation of the fracture-dependent permeability consists of the following steps:

1. Stress/strain evaluation at the integration point level
2. Definition of the crack strain
3. Definition of the fracture aperture
4. Derivation of modified permeability according to the cubic law
5. Definition of relative permeability factor for method 1 and 2
6. Definition of permeability in crack coordinate system
7. Transformation of permeability to element coordinate system

1. Stress/strain evaluation at the integration point level

The definition of the fracture-dependent permeability takes place at the integration point level of each element (see Figure 4.1).

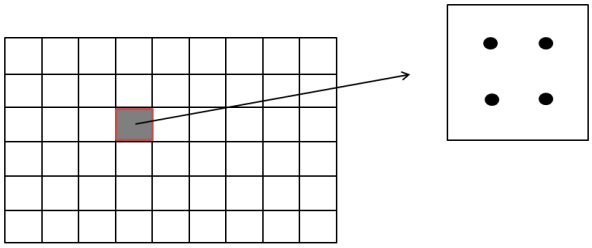

Figure 4.1: Evaluation of permeability at the integration point level.

At each integration point, the stress and strain state is evaluated and transformed into the principal stress and strain directions (see Figure 4.2). The occurrence of a crack at the integration point is defined based on the main principal strain. If the main principal strain exceeds a certain threshold, a crack is assumed to occur orthogonally to the main principal strain. The choice for a strain criterion rather than a stress criterion allows for the modelling of material non-linearity and post-peak behaviour.

The model has been formulated under the assumption of a rotating crack model, meaning that at each loading step, the principal stresses/strains are reevaluated, and the direction of the crack is determined. The principal strain axis thus always has the same directions as the crack axes (see Figure 4.3).

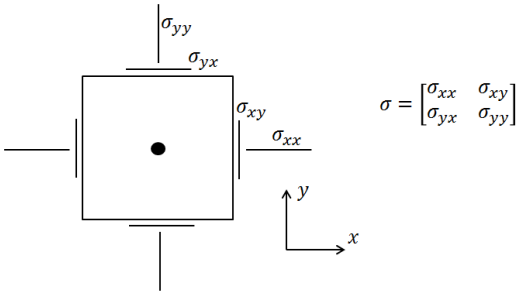

(a) Regular stress state.

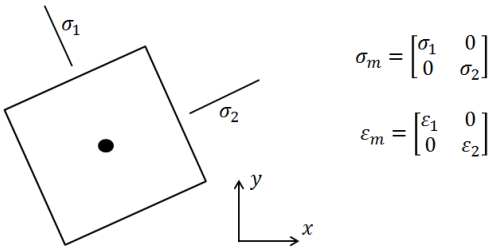

(b) Principal stress state.

Figure 4.2: Stress state defined along element and principal axes.

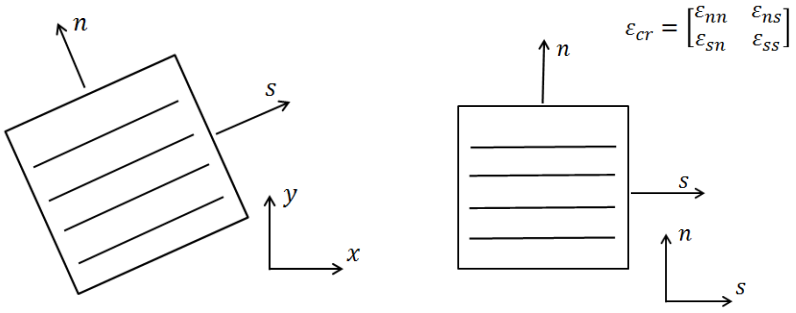

(a) Element axes.

(b) Crack axes.

Figure 4.3: Crack state defined along the element and crack axes.

2. Definition of the crack strain

Because the principal strain axes coincide with the crack axes, the direction of the main principal strain (ε_1) is equal to the crack normal strain (ε_n). For method 1, the crack normal strain (ε_n) is assumed to be equal to the main principal strain (ε_1) (Equation (4.1)), whereas, for method 2, the crack normal strain (ε_n) is defined as the main principal strain minus the strain criterion threshold (ε_t) (Equation (4.2)).

$$M1 : \varepsilon_n = \varepsilon_1 \tag{4.1}$$

$$M2 : \varepsilon_n = \varepsilon_1 - \varepsilon_t \tag{4.2}$$

3. Definition of the fracture aperture

The model only takes into account tensile fracture opening according to mode I (Atkinson and Meredith, 1987) as it is assumed that mode I cracks will contribute most significantly to the change in permeability around geothermal wellbores. The fracture opening, or aperture (b), is assumed to be constant along the fracture. The aperture depends on the crack normal strain and a spacing parameter as defined by Vecchio and Collins (1986) (see Equation (4.3)). Whereas Vecchio and Collins (1986) define the crack spacing parameters based on the reinforcement spacing in the concrete, this model employs an expression for the so-called crack bandwidth according to Govindjee's projection method (Govindjee et al., 1995). The crack bandwidth (h_{cr}) is an expression for the fracture zone, which is determined based on the element's size and the direction of the fracture.

$$b = \varepsilon_n \cdot h_{cr} \tag{4.3}$$

4. Derivation of modified permeability according to the cubic law

In order to create coupling between the geomechanical response of the rock, i.e. the initiation of cracking and crack growth (aperture increase), to a corresponding change in permeability, the cubic law has been employed. The cubic law expresses the transmissivity of a crack as a cubic function of the crack aperture (Equation (4.4)). The permeability is derived from this expression and is therefore defined as a quadratic function of the aperture (Equation (4.5).

$$T = kA = \frac{wb^3}{12} \tag{4.4}$$

$$k = \frac{b^2}{12} \tag{4.5}$$

Under the theory of the cubic law, the crack is assumed to consist of two smooth, parallel plates forming a pathway through the rock for the laminar fluid flow (Figure 4.4). Natural fractures do not have smooth, parallel walls, but are often rough and possibly contain infill material (Figure 4.5). In order to account for this deviation, a hydraulic aperture is implemented replacing the purely mechanical aperture. The hydraulic aperture is a function of the mechanical aperture and other rock fracture parameters, depending on the specific empirical relation that is adhered.

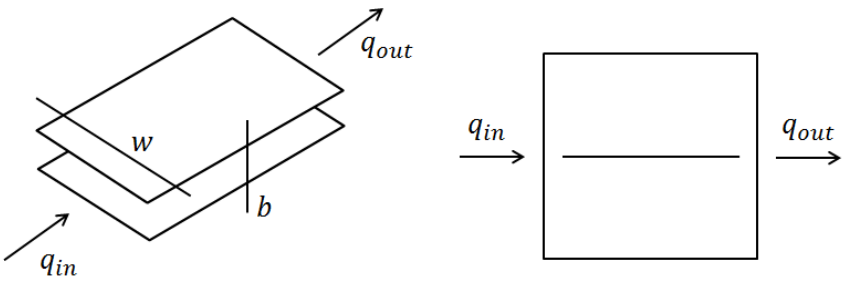

Figure 4.4: The parallel plate model for a fracture.

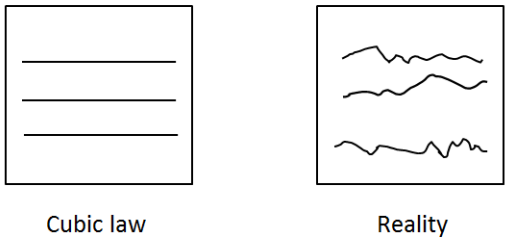

Figure 4.5: The difference between the assumptions under the cubic law and 'reality'.

5. Definition of relative permeability factor for method 1 and 2

The rock has an initial permeability as defined by the input value (k'_0). Once fracturing occurs, two different ways of expressing the updated modified permeability due to fracturing are implemented in the model concept:

- Method 1: The presence of fractures results in a change in the initial permeability (k_0), whereby k_0 is multiplied by a relative permeability factor (k_{rel}).
- Method 2: The presence of fractures results in an additional increase of the permeability (k_{fr}) on top of the initial permeability (k_0).

See Figure 4.6 for the visualisation of the two methods.

Figure 4.7 shows how fracture orientation affects the anisotropy of the permeability. If fractures are orientated purely in the x- or y-direction, this will lead to an increase in k'_{xx} or k'_{yy}. If the fractures are rotated with respect to the xy-coordinates, it results in an increase in both k'_{xx} as well as k'_{yy}, where the magnitude of the respective increase depends on the orientation of the crack axes.

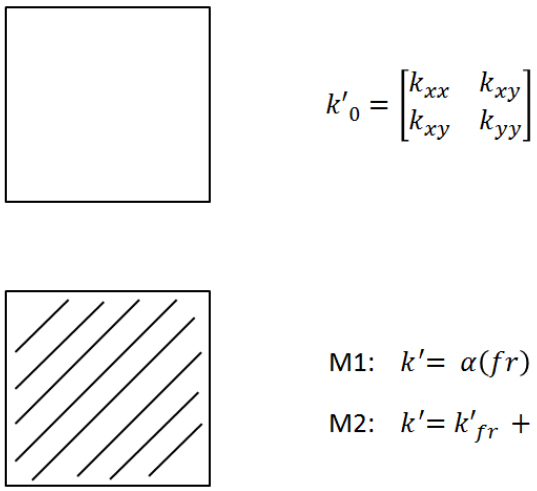

Figure 4.6: Definition of the updated modified permeability according to method 1 and 2.

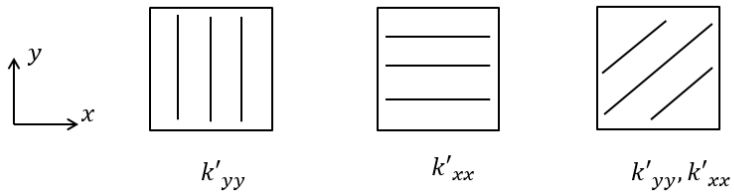

Figure 4.7: Effect of fracture orientation on the anisotropy of the modified permeability.

The permeability factor, according to method 1, is defined as the ratio between the mechanical aperture (b) and a theoretical initial aperture (b_0). This derivation is made under the assumption that the other parameters in the expression for the permeability remain constant during the analysis, thus defining k_{rel} as

$$k_{rel} = \frac{k'}{k'_0} = \frac{\frac{b^{*2}}{12\mu}}{\frac{b_0^{*2}}{12\mu}} = \frac{b^{*2}}{b_0^{*2}} = \frac{f(b,...)^2}{f(b_0,...)^2} = \frac{b^2}{b_0^2} \tag{4.6}$$

Method 2, in contrary to method 1, requires an appropriate expression of the aperture in the form of a hydraulic aperture. For this model, the hydraulic aperture is defined according to the empirical relation by Barton et al. (1985) (see Section 3.2.3). In order to preserve a similar flow in the model implementation, the updated modified permeability for method 2 is also expressed in terms of a relative permeability factor,

$$k' = k'_0 + k'_{fr} = k'_0 + \frac{b^{*2}}{12\mu} = k_{rel} \cdot k'_0, \tag{4.7}$$

where

$$k_{rel} = 1 + \frac{b^{*2}}{12\mu k'_0} \tag{4.8}$$

6. Definition of permeability in the crack coordinate system

The fracture permeability is initially defined in the crack coordinate system (see Figure 4.3). As the crack plane is assumed to be aligned orthogonal to the crack normal strain, this increases the permeability orthogonal to the n-direction

$$k_{fr}^{'ns} = \begin{bmatrix} 0 & 0 \\ 0 & f(b) \end{bmatrix} \tag{4.9}$$

The model allows for the definition of three orthogonal cracks (in the direction of the principal strains). Each crack contributes to an increase in permeability in specific directions. The fracture permeability along the crack axes is therefore defined according to Equation (4.10) and Equation (4.11) for method 1 and 2, respectively. b_1, b_2 and b_3 represent the relative apertures of the cracks in the three directions for method 1, and the absolute apertures of the cracks in the three directions for method 2. For method 1, if no cracking occurs, the relative aperture is equal to 1 and consequently $f(b) = 1$, thus the diagonal components of $k_{fr}^{'ns}$ are always ≥ 1. This is not the case for method 2, where if no cracking occurs $b = 0$, and thus $f(b) = 0$.

$$k_{fr}^{'ns} = \begin{bmatrix} f(b_2)\cdot f(b_3) & 0 & 0 \\ 0 & f(b_1)\cdot f(b_3) & 0 \\ 0 & 0 & f(b_1)\cdot f(b_2) \end{bmatrix} \tag{4.10}$$

$$k_{fr}^{'ns} = \begin{bmatrix} f(b_2)+f(b_3) & 0 & 0 \\ 0 & f(b_1)+f(b_3) & 0 \\ 0 & 0 & f(b_1)+f(b_2) \end{bmatrix} \tag{4.11}$$

7. Transformation of permeability to element coordinate system

Once the permeability tensor has been determined in the crack coordinate system, it is transformed back to the element coordinate system (xy) under the assumption that the crack coordinate system coincides with the principal axes, by making use of the same strain-transformation matrix [T] (see Equation (4.12)), which also performed the transformation to the principal stress/strain state. This rotation results in an expression for the fracture permeability in the direction of the element axes. For computational aspects, a rotating crack model is adopted, meaning that the direction of the crack axes is determined at each loading increment, i.e. the transformation matrix [T] does not remain fixed.

$$k_{fr}^{'xy} = [T]^{-1} k_{fr}^{'ns} \tag{4.12}$$

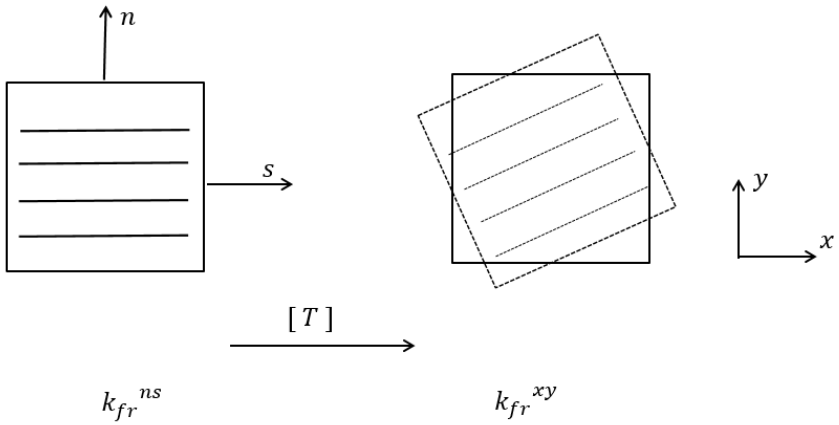

Figure 4.8: Crack transformation to the xy-coordinate system.

The definitions of the relative permeability according to methods 1 and 2 are given in Equations (4.13) and (4.14), respectively. It holds for both methods that if no cracking has occurred, then k_{rel} is equal to the identity matrix $[I]$. According to method 1, $k_{fr}^{'xy} = [I]$ in case of no cracking, because of the definition of the relative aperture (see previous section). And according to method 2, if no cracking has occurred $b = 0$ and thus $k_{fr}^{'xy} = 0$, consequently $k_{rel} = [I]$.

$$k_{rel} = k_{fr}^{'xy} \tag{4.13}$$

$$k_{rel} = [I] + \frac{k_{fr}^{'xy}}{k_0'} \tag{4.14}$$

4.3 Subroutine description

Diana FEA is an extensive finite element software package that can be used in a wide range of civil and geotechnical engineering sectors. For the modeling of THM-processes, the software includes mixture and thermo-poroelastic analysis. In these analyses, nodal degrees of freedom consists of not only displacements, but also pore pressures, for the mixture analysis, and pore pressures and temperatures, for the thermo-poroelastic analysis. For the description of fractured rock or concrete/masonry material, Diana provides several different fracture material models, adhering to either a discrete or smeared approach.

The model concept, as described in the previous section, has been formulated by creating three new subroutines: CRKPER, CRKDIR and CRKAPT. The combination of these subroutines, together with the YNMIXT subroutine in Diana FEA software allows for the simulation of a mixture analysis where the permeability is fracture dependent. The purpose of the YNMIXT subroutine is to determine the internal forces and the fluxes for mixture analysis. The nodal results consist of displacements and pressure potentials. A description of the tasks of subroutine YNMIXT is also provided in the next section. Figure 4.9 below shows an overview of the linking between the three new subroutines and the Diana mixture analysis subroutine.

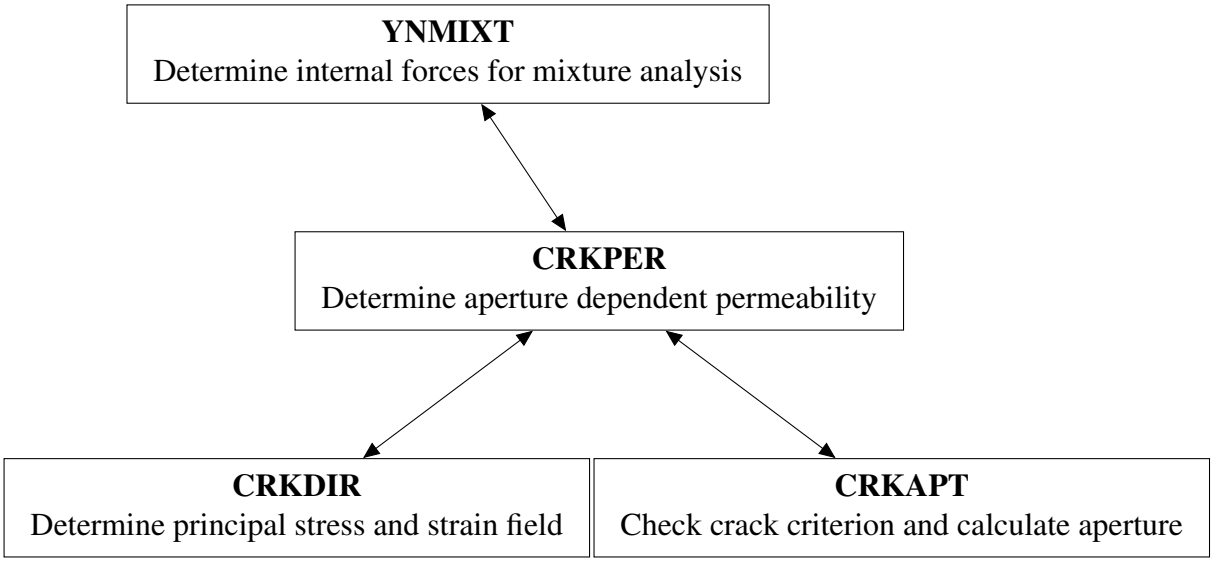

Figure 4.9: Overview of the fracture dependent mixture analysis model

The next section (Section 4.3) gives the task description of the YNMIXT subroutine and the new subroutines (CRKPER, CRKDIR and CRKAPT) in more detail. The three additional subroutines call on other already existing, subroutines in the Diana FEA software, these subroutines have been underlined in their corresponding task description.

4.3.1 YNMIXT

The purpose of the YNMIXT subroutine is to determine the internal forces and fluxes for mixture analysis. The nodal results consist of displacements and pressure potentials. An overview of the subroutine tasks is shown below.

Start subroutine YNMIXT

- Update nodal pressures from calculated pressure d.o.f. increment
- Update displacement d.o.f.
- Update pressure d.o.f., get/set pore pressure related data
- Start loop over integration points
  - Get/set general interpolation matrices and deformation data
  - Get/set pore pressure related data
  - Determine relative permeability
    - Porosity dependent
    - Saturation dependent
    - Aperture dependent $\rightarrow$ CRKPER
  - Apply relative permeability
  - Calculate pore pressure contribution to right hand-side
    - Material time derivative
    - Inertial effects
    - Mass/weight correction
    - Buoyancy force
  - Determine velocity divergence solid and pressure gradient
  - Store updated permeability
  - Calculate and store Darcy flow
  - Store pore pressure potential and pore pressures
  - Calculate internal forces
  - End loop over integration points

End subroutine YNMIXT

4.3.2 CRKPER

The purpose of the subroutine CRKPER is to calculate the relative permeability and determine the corresponding relative permeability factor in tensorial form. The relative permeability can be calculated according to two different methods. The subroutine calls on the other subroutines: CRKDIR and CRKAPT. The tasks of the subroutine are shown below.

Start subroutine CRKPER

- Determine crack direction, normal strain and transformation matrix → CRKDIR
- Calculate crack aperture → CRKAPT
- Calculate permeability increase in crack directions
  - Method 1: Calculate relative permeability as a function of the relative aperture increase
  - Method 2: Calculate the relative permeability as a function of the fracture permeability and the initial permeability
- Transform to element coordinate system
- Determine permeability factor tensor

End subroutine CRKPER

4.3.3 CRKDIR

The purpose of the subroutine CRKDIR is to determine the principal stress and strain field. It also calculates the crack bandwidth according to Govindjee's projection method. It calls on the following other subroutines in Diana: MSGAXI/MSGSOL, SORTRI, TEPSA/TEPS3 and CRACKB. The tasks of the subroutine are shown below.

Start subroutine CRKDIR

- Calculate and sort principal stress → MSGAXI/MSGSOL, SORTRI
- Calculate strain in principal stress direction → TEPSA/TEPS3
- Calculate crack bandwidth → CRACKB

End subroutine CRKDIR

4.3.4 CRKAPT

The purpose of the subroutine CRKAPT is to first of all define all the additional, required input parameters. Next, it checks the crack criterion, determines the crack strain and thereafter the (relative) aperture according to method 1 or 2. The tasks of the subroutine are shown below.

Start subroutine CRKAPT

- Define input parameters
- Check crack criterion
- Determine crack strain
- Determine (relative) crack aperture
  - Method 1: Determine the relative aperture increase with respect to the initial aperture
  - Method 2: Determine the hydraulic aperture as a function of the mechanical aperture according to an empirical relation

End subroutine CRKAPT

4.4 Conclusion

For the simulation of fluid flow through fractured rock, a new material model is developed that provides hydro-mechanical coupling by relating fracture direction and size to the permeability of the rock material. The model concept proposes two different methods for the definition of the fracture-dependent permeability, where method 1 treats the rock mass as a continuum containing fractures, resulting in an overall update in the permeability and method 2 separately adds the effects of the fractures by including a fracture permeability.

For the implementation of the fracture-dependent permeability into the Diana code, an extension to the subroutine YNMIXT (responsible for the mixture analysis) has been created. This extension consists of three new subroutines being: CRKPER, CRKDIR, CRKAPT. Generally speaking, CRKPER defines the permeability in the crack coordinate system (for both method 1 and 2) and performs the transformation to the element coordinate system. CRKDIR evaluates the stresses/strains at the integration point level, thereby defining the direction of the crack axes and corresponding crack bandwidth. CRKAPT calculates the crack strain and (relative) aperture for both methods.

To summarise, the proposed model has been developed in line with the following assumptions and concepts:

1. A single fracture is represented by two parallel plates separated by the fracture aperture. Fluid flow through this fracture can therefore be described using the cubic law, which assumes laminar fluid flow through a pair of smooth, parallel plates with infinite lengths;

2. Only tensile cracking (crack mode I) is considered, as it is assumed that this type of cracking will contribute most significantly to the increase in permeability around a geothermal borehole. The fracture aperture is thus defined as a function of the tensile strain and crack bandwidth;
3. The model treats the cracked material as new material having its own permeability characteristics. The model evaluates the hydro-mechanical relations in the direction of the principal strain vector and thus allows for the modelling of a maximum of three orthogonal cracks at one point.
4. It is assumed that fracturing occurs if the principal strain exceeds a tensile strain threshold. Consequently, a fracture will develop perpendicular to the direction of the principal strain, resulting in an increase in permeability in the fracture direction;
5. For computational purposes the rotating crack model has been employed, which reevaluates the crack direction at each load increment and therefore the strain-transformation matrix is not fixed, thereby ensuring coincidence between the principal strain and crack axes.

5. Model evaluation and verification

5.1 Introduction

This chapter aims to evaluate and verify the proposed model for a simple two-dimensional (plane-strain) and a three-dimensional test case analysis, thereby comparing and discussing the results generated by the two different methods as proposed in the model concept in the previous chapter (Chapter 4). The 2D test case is described in Section 5.2. It demonstrates the rotation of the crack axes with respect to the principal axes, and thus a permeability with a changing directionality. The correct implementation of the model is verified by comparing the numerical results with an analytical calculation. The 3D test case is described in Section 5.3 and demonstrates the agreement between the proposed fracture-dependent permeability model and the Total Strain crack model.

5.2 2D test case

The purpose of this first test case is to demonstrate the workings of the fracture-dependent permeability model and show how the rotation of the principal axes (and thus the crack axes) corresponds with changes in permeability. For verification, expectations with regards to the results generated by the model have been made on beforehand. Both methods 1 and 2, as described in the previous chapter, have been implemented. The results produced by the different methods will be evaluated and compared in the final section.

5.2.1 Analysis

This section discusses a two-dimensional test case, consisting of plane-strain elements, that is subjected to fracture-dependent permeability analysis. For this analysis, the pore pressure remains equal to zero (see Figure 5.1), and therefore, the effective stresses are equal to the total stresses.

Figure 5.1 shows the visualisation of the plane-strain test case. The dimensions of the block are 1 x 1 m. It is supported at the bottom edge in only the normal direction (y-direction), except for the left vertex, which is constrained in both directions. No flow (pore pressure potential) boundary conditions are imposed. The mesh consists of nine plane-strain, quadrilateral elements of equal size. A relatively rough mesh density was adopted because the primary purpose of this analysis is to demonstrate the capability of the model to determine the direction of the permeability with respect to direction of the applied loading. The mesh consisting of nine elements was considered sufficient to provide the qualitative assessment.

A linearly elastic, isotropic rock material is applied in combination with the fracture-dependent permeability model. A linearly elastic, isotropic rock material description was implemented such that the rotation of the crack axes would not be affected by any per-

manent deformations or heterogeneities. The material properties can be found in Table 5.1. The initial modified permeability (k_0') is equal to $1 \cdot 10^{-6}$ (isotropic). Table 5.1 also shows the values for the method-dependent input parameters (b_0 and JRC), which will be discussed in their corresponding sections. And finally, it should be noted, that the tensile strength has only been included in the fracture-dependent permeability model for the definition crack strain criterion, it thus does not affect the linearly, elastic rock material model.

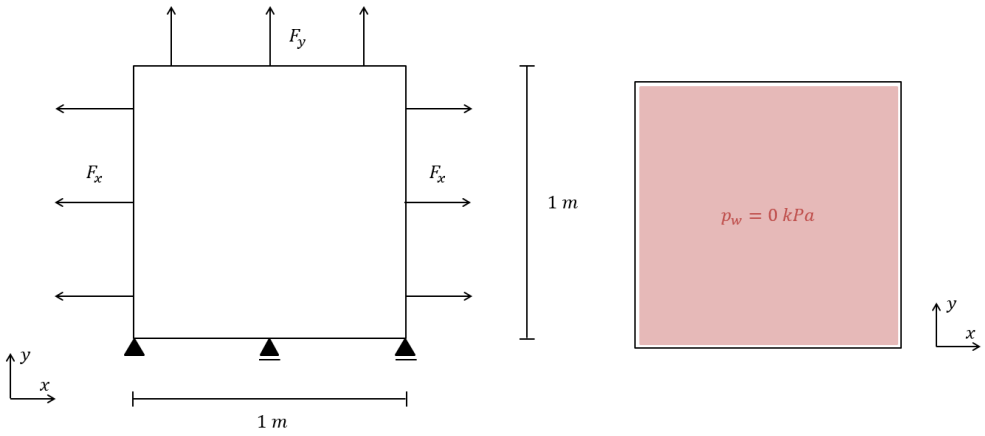

Figure 5.1: 2D test case dimensions, boundary conditions and loading.

Table 5.1: Material properties of the linear, elastic rock in combination with the fracture-dependent permeability model used in the 2D test case.

	Parameter	**Value**	**Unit**
General	Young's modulus E	$3 \cdot 10^4$	MPa
	Poisson's ratio ν	0	-
	Density γ	2.5	T/m^3
	Porosity n	0.2	-
Fracture-dependent permeability model	Initial modified permeability k_0'	$1 \cdot 10^{-6}$	$m^3 s/T$
	Dynamic vsicosity μ	$1 \cdot 10^{-6}$	T/ms
	Initial aperture b_0	$1 \cdot 10^{-5}$ / $1 \cdot 10^{-6}$	m
	JRC	2.5 / 13	
	Tensile strength f_t	800	kPa

The block is subjected to tensile loading in both the x- and y-direction. The total duration of the analysis is 20 seconds, during which the applied loading is varied. The time dependency of the tensile forces (F_x and F_y) can be found in Figure 5.2, where the development of the loading factors has been plotted versus time. The reason for applying this specific stress path is to illustrate how the dominant direction of the permeability can change over time following the direction of the applied loading. Both F_x and F_y are distributed forces having a magnitude of 100 kN/m. F_x is applied at the lateral edges of the block, and F_y at the top (see Figure 5.1).

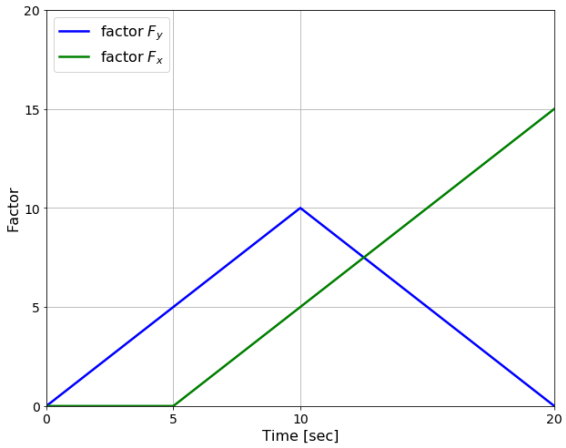

Figure 5.2: Loading factor applied to F_x and F_Y during the analysis.

5.2.2 Expected results

As defined in the proposed model, the rock will fracture if a tensile strain exceeds the fracture strain criterion. In this case, the strain criterion has been determined based on an assumption of the tensile strength and the Young's modulus of the material (see Equation (5.1)). For this analysis f_t = *800 KPa* and E = *3E+07 KPa*, and therefore, the crack strain criterion is equal to $800/3 \cdot 10^{-7} = 2.67 \cdot 10^{-5}$. Note that the linearly elastic, isotropic material model description of the material does not include a tensile strength parameter. Tensile stresses can therefore exceed the *800 KPa* without this resulting in failure or plastic deformation. However, the fracture-dependent permeability model will update the permeability if during the analysis the tensile strain exceeds the crack strain criterion.

$$\varepsilon \geq \varepsilon_t = \frac{f_t}{E} \tag{5.1}$$

Rotation of the crack axes

Following the definition of the model, a crack will occur in the direction orthogonal to the main principal direction. Consequently, the modified permeability will increase in the direction of the crack and thus orthogonal to the principal direction. Assuming a rotating crack model, the direction of the crack axes is not fixed upon initiation but instead rotates along with the direction of the principal axes.

Initially, a tensile force is applied only in the y-direction (F_y) resulting in a principal vertical stress. The principal stress exceeds the 800 kPa at t = 8 s (see Figure 5.3a), a first increase of the permeability in the x-direction (k'_{xx}) is therefore expected to occur at this moment. At t = 10 s, F_y reaches its maximum (see Figure 5.3b) after which it starts decreasing, while F_x continues to increase until t = 20 s. This results in a rotation of the principal axes and thus also a corresponding rotation of the crack axes. An increase of k'_{yy} relative to k'_{xx} should be observed. At t = 20 s, F_x has reached its maximum, while F_y is 0. This results in a principal stress in the x-direction (see Figure 5.3c). Consequently, crack formation is entirely vertical, and k'_{yy} is dominant over k'_{xx}.

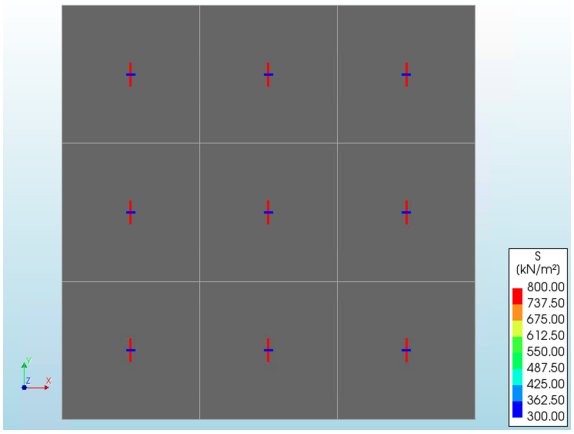

(a) t = 8 s

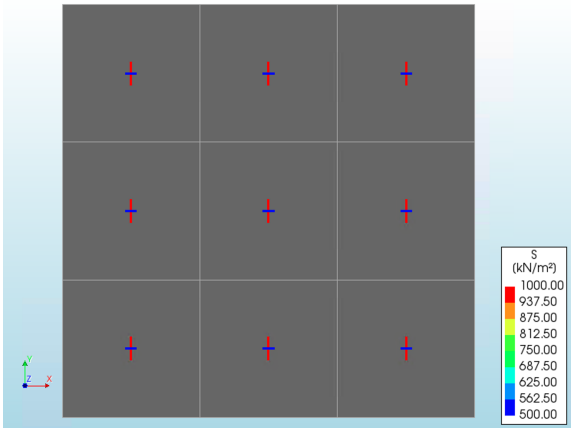

(b) t = 10 s

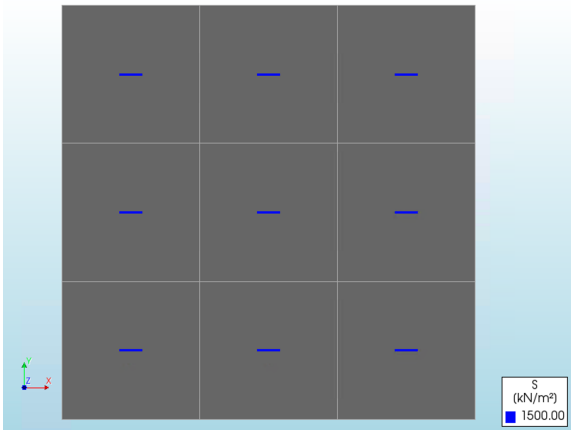

(c) t = 20 s

Figure 5.3: Direction of principal stresses for t = 8, 10 and 20 seconds.

Analytical verification

For the verification of the numerical solution, a simple analytical analysis is executed. Due to the imposed boundary conditions and symmetrical loading, the stress-strain field in the domain is homogeneous, which consequently results in a homogeneous permeability development.

For example, the final solution at t = 20 s is evaluated. At that moment, the main principal direction is parallel to the x-axis (see Figure 5.3c), and thus a crack will occur

in the orthogonal direction, i.e. in the y-direction. As a consequence, the permeability will also increase in the direction of the crack. At t = 20 s, the main principal strain (ε_1) is equal to $5 \cdot 10^{-5}$ ($> \varepsilon_t$), see Figure 5.4 below, and the crack bandwidth is equal to the height of the element, which is $3.33 \cdot 10^{-3}$ m.

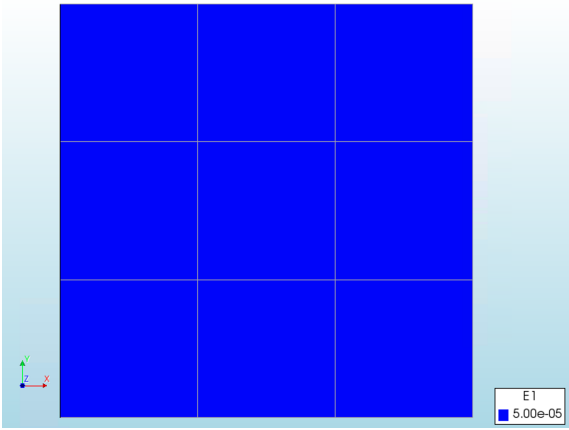

Figure 5.4: The principal strain (ε_1) at t = 20 s.

This results in the following derivation of the modified permeability according to both methods:

According to method 1, assuming $b_0 = 1 \cdot 10^{-6}$ m:

$$\varepsilon_n = \varepsilon_1 = 5.00 \cdot 10^{-5}$$

$$b = \varepsilon_n \cdot h_{cr} = 1.67 \cdot 10^{-5}\ m$$

$$k' = \frac{b^2}{b_0^2} \cdot k'_0 = 2.78 \cdot 10^{-4}\ m^3 s/T$$

According to method 2, assuming JRC = 2.5:

$$\varepsilon_n = \varepsilon_1 - \varepsilon_t = 2.33 \cdot 10^{-5}$$

$$b = \varepsilon_n \cdot h_{cr} = 7.78 \cdot 10^{-6}\ m$$

$$b^* = b^2 \cdot JRC^{-2.5} = 6.12\ \mu m = 6.12 \cdot 10^{-6}\ m$$

$$k' = k'_0 + \frac{b^{*2}}{12\mu} = 1 \cdot 10^{-6} + 3.12 \cdot 10^{-6} = 4.12 \cdot 10^{-6}\ m^3 s/T$$

Note that the empirical relation for calculating the hydraulic aperture for method 2, considers the aperture expressed in micrometers. Moreover, interesting to see is that if method 2 is employed with, for example, JRC = 10, the hydraulic aperture b^* equals $1.97 \cdot 10^{-7}$ m. This results in a fracture permeability k'_{fr} equal to $3.05 \cdot 10^{-9}$ $m^3 s/T$. This fracture permeability only has a minimal contribution to the initial modified permeability in this case. However, if the initial modified permeability was assumed to be much lower, than its contribution would have been more significant.

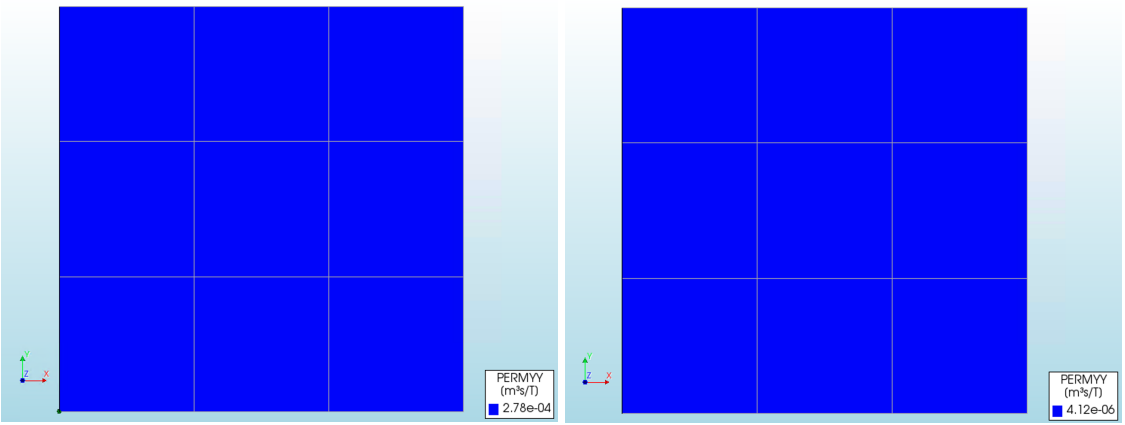

(a) Method 1 $b_0 = 1 \cdot 10^{-6}$ *m* (b) Method 2 *JRC* = *2.5*

Figure 5.5: The maximum permeability (k'_{yy}) at t = 20 seconds.

5.2.3 Results

The next sections discuss the results of the two-dimensional test case that is subjected to fracture-dependent permeability analysis according to the two proposed methods. The imposed boundary conditions and the symmetrical loading created a homogeneous stress-strain field. Results are therefore evaluated in one node (node 36) as it can represent the development of the whole domain. The location of this node can be seen in Figure 5.6 below.

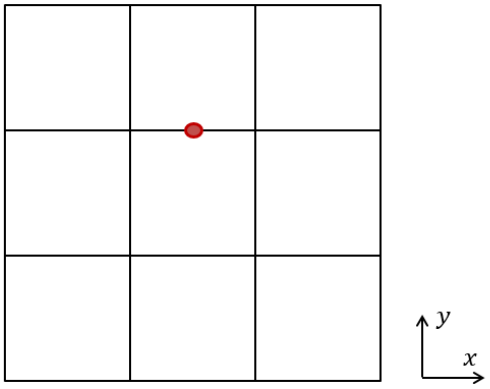

Figure 5.6: The 2D test case consists of nine elements. The location of the node 36 has been indicated.

Method 1

Figure 5.7 shows the development of the modified permeability for the total duration of the analysis according to method 1. The analysis has been performed for two values of b_0: $1 \cdot 10^{-5}$ m (Figure 5.7a) and $1 \cdot 10^{-6}$ m (Figure 5.7b).

The results show the initial increase in k'_{xx} at t = 8 s when $b_0 = 1 \cdot 10^{-6}$ m and at t = 9 s when $b_0 = 1 \cdot 10^{-5}$ m. This difference in onset of permeability increase can be explained by the difference in b_0, which also functions as a threshold parameter. Due to

the formulation of the crack strain criterion, crack formation will already occur at t = 8 in both cases. However, the corresponding aperture is $1 \cdot 10^{-6} \leq b < 1 \cdot 10^{-5}$ m and therefore a increase in the permeability can only be observed when $b_0 = 1 \cdot 10^{-6}$ m. k'_{xx} reaches its maximum value at t = 10 s for both cases. The difference in the absolute maximum value for k'_{xx} can also be attributed to the difference in b_0. The parameter thus affects the initiation of the permeability increase as well as the magnitude of the solution.

At t = 12 s, the principal stress has dropped below 800 KPa and thus the permeability is equal to its initial value. From that moment on wards as F_x continues to increase, the development of k'_{yy} can be observed. This increase once again shows a slight delay when $b_0 = 1 \cdot 10^{-5}$ m compared to $b_0 = 1 \cdot 10^{-6}$ m and also reaches a lower final value. The final result at t = 20 s shows that for $b_0 = 1 \cdot 10^{-6}$ k'_{yy} has reached a value of $2.78 \cdot 10^{-4}$ $m^3 s/T$, which is in agreement with the analytical calculation.

The model appears to behave more sensitive for a lower value of b_0, showing a greater response to a small change. Furthermore, noticeable is the drop in k'_{xx} to its initial value of k'_0. This has two reasons. First of all, a linearly elastic material model has been employed, and therefore no permanent deformation will occur. Secondly, the model adheres a rotating crack model, meaning that the occurrence and direction of the fractures are reevaluated at each load increment, and thus fractures can 'disappear' if the strain drops below the crack criterion.

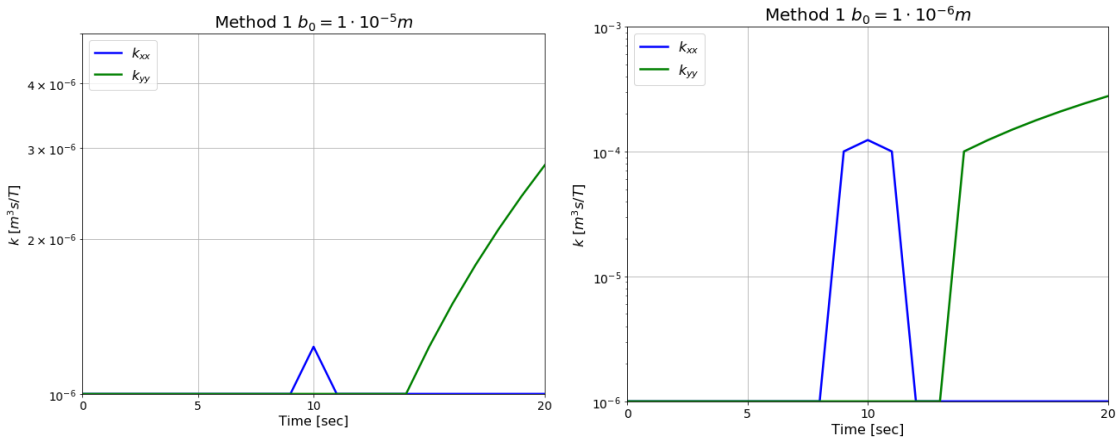

(a) k' for $b_0 = 1 \cdot 10^{-5}m$

(b) k' for $b_0 = 1 \cdot 10^{-6}m$

Figure 5.7: Development of the modified permeability according to method 1.

Method 2

Figure 5.8 shows the development of the modified permeability for the total duration of the analysis according to method 2. The analysis has been performed for two values of the input parameter: JRC = 10 (Figures 5.8a) and JRC = 2.5 (Figures 5.8b).

For JRC = 10, the changes in permeability are minimal. The maximum of k'_{xx} at t = 10 s can not be observed, and thus k'_{xx} remains more or less constant at its initial value throughout the analysis. k'_{yy} does increase slightly, however, this increase is minimal as well. For JRC = 2.5, an increase in k_{xx} is observed starting at t = 9 s, consequently dropping to the initial value at t = 12 s value after having reached its peak at t = 10 s. This observation is in line with the expected result. The final result at t = 20 s shows that for JRC = 2.5 k'_{yy} has reached a value of $4.12 \cdot 10^{-6}$ $m^3 s/T$, which is in agreement with the analytical calculation. The very minimal increase in k' for JRC = 10 might

be explained by the relatively high k'_0, resulting in an insignificant contribution of the fracture permeability to the overall permeability. This phenomenon was also observed in the analytical calculation.

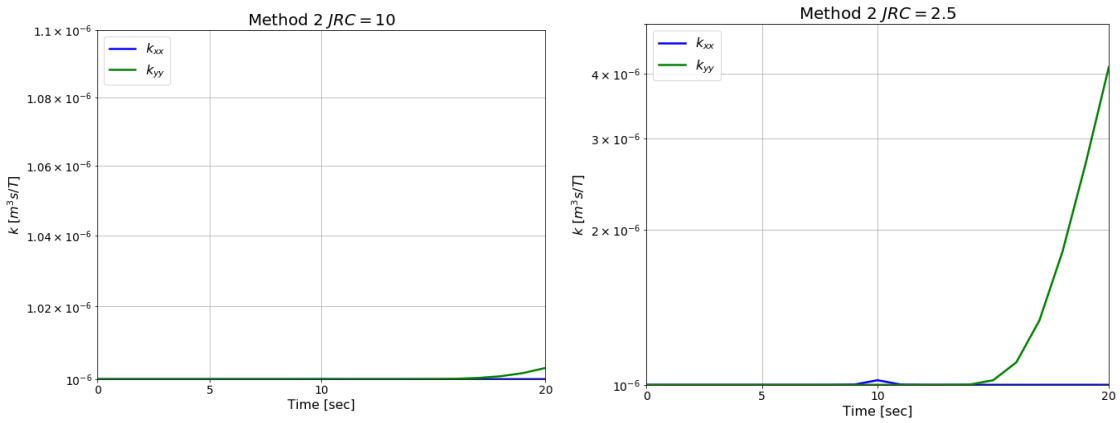

(a) k' for JRC = 10

(b) k' for JRC = 2.5

Figure 5.8: Development of the modified permeability according to method 2.

The results of both analyses show the rotation of the crack axes and the corresponding changes in permeability as expected, where k'_{xx} reaches its maximum at t = 10 s, after which, k'_{yy} becomes dominant over time due to the rotation of the crack axes. The final values of k'_{yy} at t = 20 s have been verified by comparing the results with a simple analytical solution. For method 1 and $b_0 = 1 \cdot 10^{-6}$ m, $k'_{yy} = 2.78 \cdot 10^{-4}\ m^3 s/T$, and for method 2 and JRC = 2.5, $k'_{yy} = 4.12 \cdot 10^{-6}\ m^3 s/T$ at t = 20 s. The simulations correspond with the expected results, and thus it can be concluded that the methods have been implemented correctly.

When comparing the simulations according to the two methods, one thing that can be observed, is a difference in permeability development, meaning that simulations for method 1 show a sudden, jump-like increase or decrease in permeability, whereas the results for method 2 display a much more gradual change. Apart from that, the permeability development is quite comparable. However, the quantitative results between the two methods, as well as the different input values for b_0 and JRC, vary significantly. Hence, the results display an indication of the model's sensitivity to the method-specific input parameters. Moreover, it is expected that the results generated by method 2 are also quite dependent on k'_0. This expectation is expressed because for JRC = 10 barely any increase in permeability is observed. It could be explained by the fact that the permeability change in method 2 is defined as an additional permeability increase due to cracking instead of an overall increase in the rock permeability. Thus if the initial permeability is relatively high, an increase in permeability due to the presence of a fracture is less significant, especially when the JRC is higher, indicating a smaller hydraulic aperture.

5.3 3D test case

This section discusses a three-dimensional test case that is subjected to fracture-dependent permeability analysis. The purpose of this test case is to demonstrate that the fracture-dependent permeability model can be used in combination with the Total Strain crack model, and therefore, both models are combined to describe the rock material. The analysis shows the development of a fracture plane in a three-dimensional domain.

5.3.1 Analysis

A three-dimensional block of 10 x 10 x 10 m is subjected to a fracture-dependent mixture analysis. The block is supported in x- and y-direction at its eight vertices, see Figure 5.9 below. Pore pressure constraints are imposed on two domain boundaries; the left and right yz-plane. A pore pressure potential of 0 kPa is applied on both boundaries. This will remain constant throughout the entire analysis. The block is also subjected to a tensile load. The tensile load consists of a distributed force of 100 kPa applied at the top and bottom xy-plane in the z-direction. The total duration of the non-linear analysis is four seconds. For each second, the tensile load is increased by a factor one.

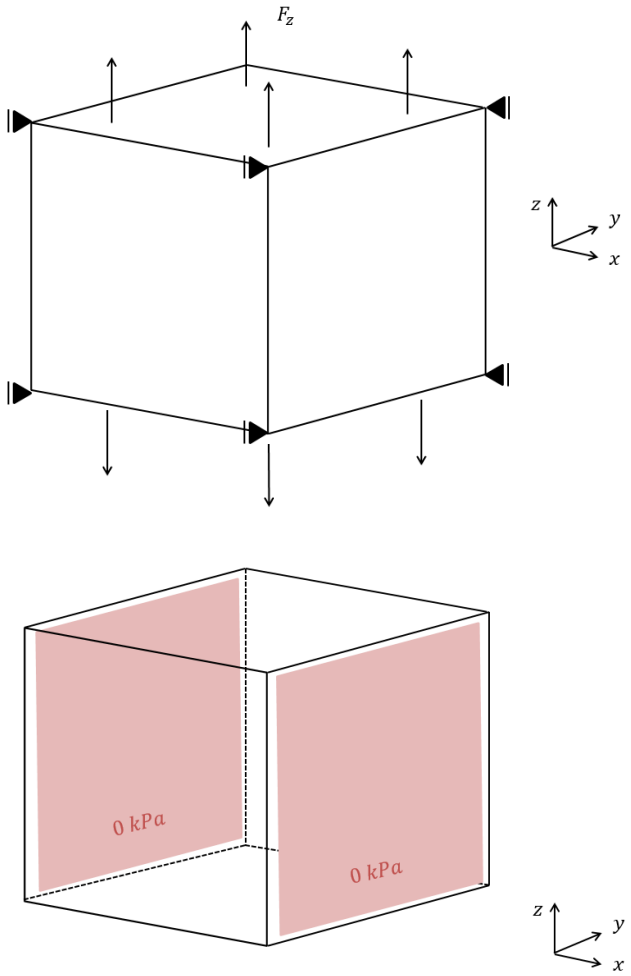

Figure 5.9: The boundary conditions and applied loading of the 3D test case.

The block is subdivided into three layers (for dimensions see Figure 5.10). The top

and bottom layer are considered to consist of 'strong' rock (see Table 5.2 for the material properties), both layers being made up of a total of 500 equal-size, quadrilateral elements of 0.9 x 0.9 x 0.9 m. The middle layer, that lays in between the 'strong' rock formation, is 1 m thick and consists of a 'weak' rock (see Table 5.2 for the material properties). It is made up of a total of 100 equal-size quadrilateral elements of 1 x 1 x 1 m. A relatively rough mesh was considered to be appropriate, because the analysis concerns a qualitative evaluation of the results by combining it with the Total Strain crack model. The material of the block (both for the 'strong' as well as the 'weak' rock) is described by the fracture-dependent permeability model in combination with a rotating, Total Strain crack model, assuming brittle failure behaviour. The crack bandwidth is determined according to Govindjee's projection method.

The fracture-dependent material model requires additional method-dependent input parameters (b_0 and JRC) on top of the ones required for a regular mixture analysis (k' and μ). These parameters can also be found in Table 5.2. A slightly higher initial modified permeability ($1 \cdot 10^{-10}\ m^3 s/T$) has been chosen than in the 2D analysis, so results generated by method 2 could also be properly evaluated. Even though the fracture-dependent permeability model also takes into account the tensile strength and Young's modulus of the material for the determination of the crack strain criterion. These parameters have been gathered under the 'Total Strain crack model' and 'General' sections in Table 5.2.

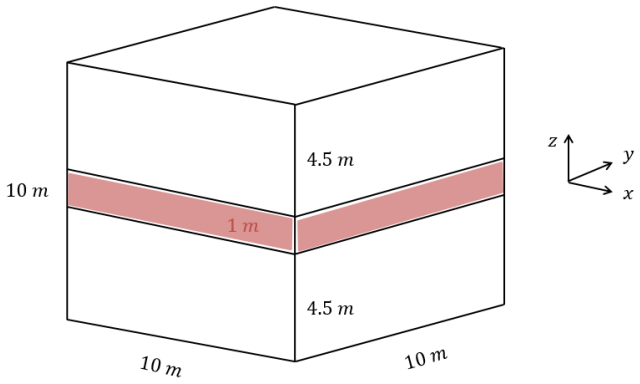

Figure 5.10: The three layers in the model consisting of 'strong' and 'weak' (red layer) rock.

Table 5.2: Material properties of the 'strong' and 'weak' rock.

	Parameter	'Strong' rock	'Weak' rock	Unit
General	Young's modulus E	$3 \cdot 10^4$	$3 \cdot 10^4$	MPa
	Poison's ratio ν	0	0	-
	Density ρ	2.5	2.5	$kg \cdot dm^3$
	Porosity n	0.1	0.1	-
Total Strain crack model	Tensile strength f_t	2.5	0.2	MPa
	Tension softening	Brittle	Brittle	-
	Residual tensile strength f_r	-	0.05	MPa
	Compressive strength f_c	200	200	MPa
Fracture-dependent permeability model	Dynamic vsicosity μ	$1 \cdot 10^{-6}$	$1 \cdot 10^{-6}$	T/ms
	Initial modified permeability k'_0	$1 \cdot 10^{-10}$	$1 \cdot 10^{-10}$	$m^3 s/T$
	Initial aperture b_0	$5 \cdot 10^{-6}$	$5 \cdot 10^{-6}$	m
	JRC	13	13	-

The only difference between the two rocks is the difference in tensile strength. For the 'strong' rock this is equal to 2.5 MPa, and for the 'weak' rock it is equal to 200 kPa. Apart from that, the properties do not differ, see Table 5.2 above. However, the difference in tensile strength affects the crack criterion for the Total Strain crack model as well as the fracture-dependent permeability model. For the fracture-dependent permeability model, the crack criterion is defined as tensile strain criterion, which consequently is defined as function of the tensile strength and the Young's modulus. For that reason, the 'weak' layer is expected to start cracking earlier that the stronger formations when subjected to the tensile loading. Because the tensile loading is applied solely in the z-direction, a horizontal fracture plane is expected to develop parallel to the xy-plane. This should lead to an increase in permeability in both k'_{xx} and k'_{yy}. The results are discussed in the next section.

5.3.2 Results

This section will first of all show the development of the principal strain and pore pressures during the analysis if no cracking occurs. After that, the results according to method 1 and method 2 are discussed. Results are evaluated along a contour probe. This contour probe is located in the middle of the 'weak' layer, parallel to the x-axis. The red line indicates the location in Figure 5.11 below.

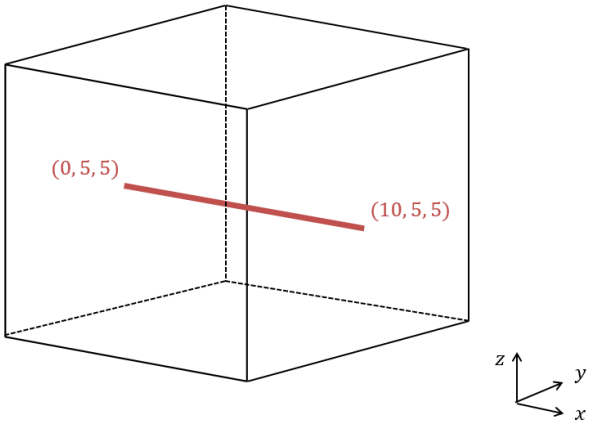

Figure 5.11: The model showing the direction of the evaluation probe along the defined axis (red line).

No cracking

If all three layers in the model are assigned the 'strong' rock properties, no cracking will occur during the analysis. For this analysis, no modifications have been made with respect to the boundary or loading conditions (tensile loading and prescribed pore pressure potential). Only in this particular case, the middle layer has been assigned the 'strong' rock material properties.

Figure 5.12 shows the evolution of the principal strain (ε_1), permeability, pore pressure and Darcy flux along the contour probe. The dotted black line in Figure 5.12a indicates the strain crack criterion (ε_t). For the 'strong' rock, this is equal to $f_t/E = 2500/3 \cdot 10^{-7}$ $= 8.33 \cdot 10^{-5}$. It can be observed that the principal strain does not exceed this threshold, and thus, no cracking occurs. The permeability will therefore remain at its initial value (Figure 5.12b). Due to the tensile loading, the pore pressures will become more negative during the analysis. Pore pressure development is constraint at the boundaries (x = 0 m and x = 10 m), because of the prescribed pore pressure potential. The pore pressure gradient induced a Darcy flux in the x-direction towards the centre of the plane (Figure 5.12d).

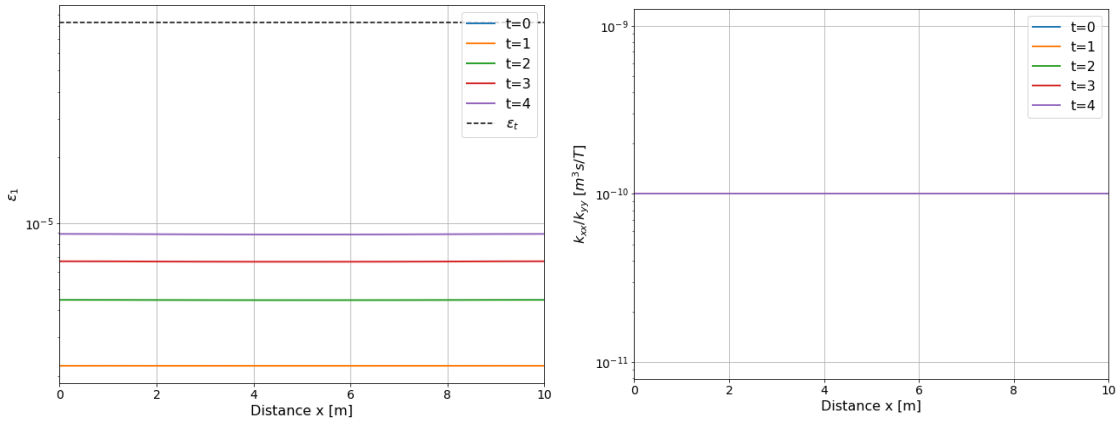

(a) ε_1

(b) k_{xx}/k_{yy}

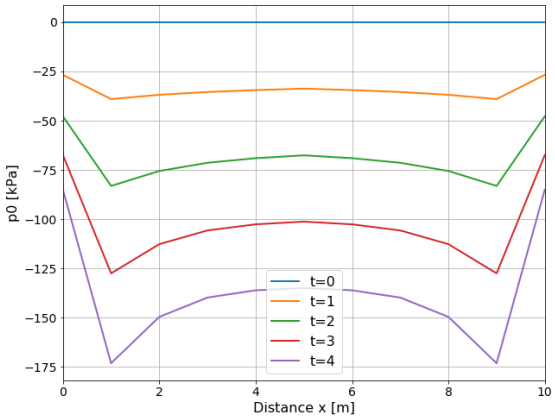

(c) p_0 $[kPa]$

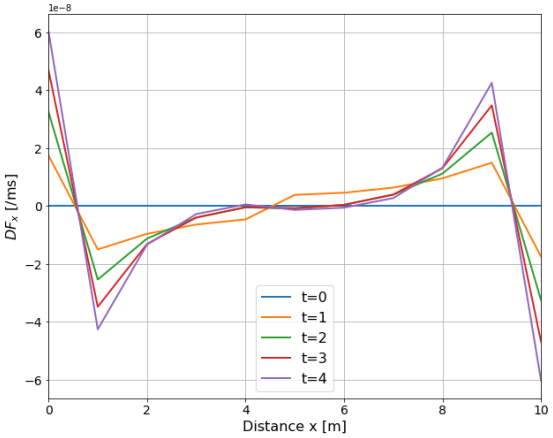

(d) DF_x

Figure 5.12: Development of principal strain, permeability, pore pressure, and Darcy flux along the contour probe if no cracking occurs.

Method 1

For the analysis according to method 1, the middle layer is assigned the 'weak' rock properties and the initial aperture has been set at $5 \cdot 10^{-6}$ m. Figure 5.13 shows the evolution of the principal strain (ε_1), permeability, pore pressure and Darcy flux along the contour probe. Moreover, Figure 5.14 shows the formation of a horizontal crack plane in the middle layer according to the Total Strain crack model. This crack plane first starts developing at t = 3 s.

The dotted black line in Figure 5.13a indicates the strain crack criterion (ε_t) for the 'weak' rock. This is equal to $f_t/E = 200/3 \cdot 10^{-7} = 6.67 \cdot 10^{-6}$. In Figure 5.13a, it can be observed that this threshold value is first exceeded at t = 3 seconds at the outer edges of the contour probe. Consequently, an increase in the permeability can be seen in Figure 5.13. At t = 4 s, a crack plane along the entire length of the contour probe has evolved, showing a corresponding increase in permeability. Assuming brittle tension failure, the effective stresses in the rock instantaneously drop to their prescribed residual value (0.05 MPa in this case, see Table 5.2) upon crack formation. As a result, the pore pressures in the fractured elements will become more negative (see Figure 5.13c). This pore pressure gradient induces an increase in the Darcy flux in the x-direction (Figure 5.13d) when comparing it to the non-cracked situation.

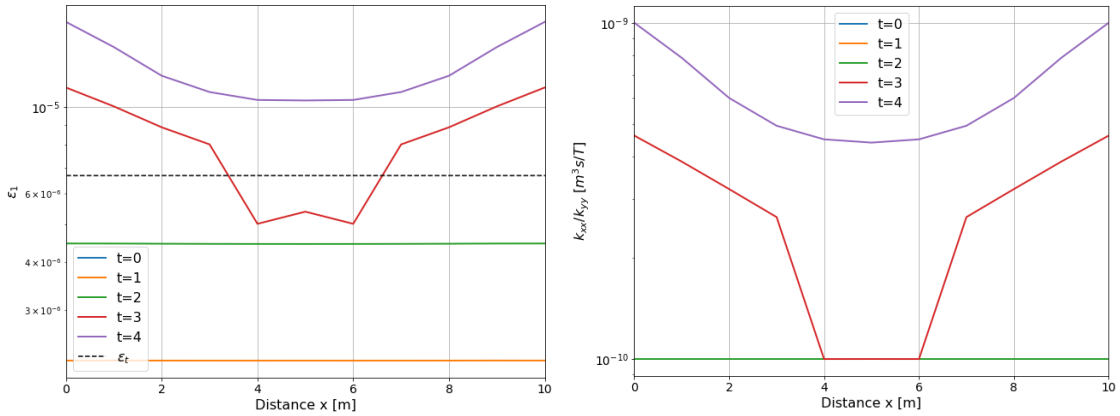

(a) ε_1

(b) k_{xx}/k_{yy}

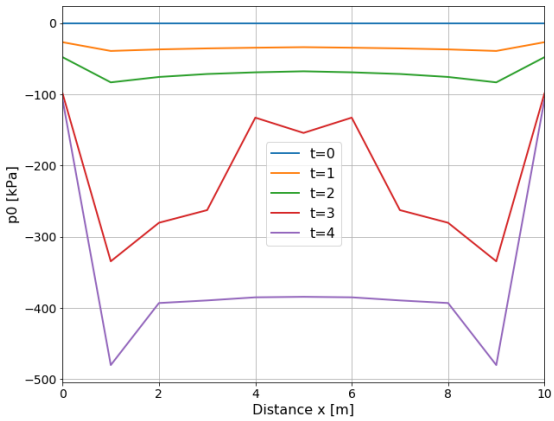

(c) p_0

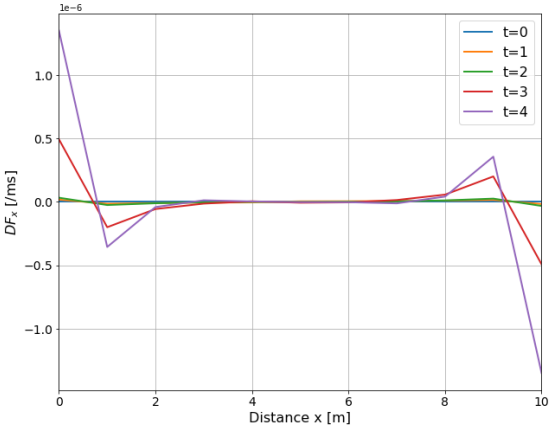

(d) DF_x

Figure 5.13: Development of principal strain, permeability, pore pressure, and Darcy flux along the contour probe for method 1.

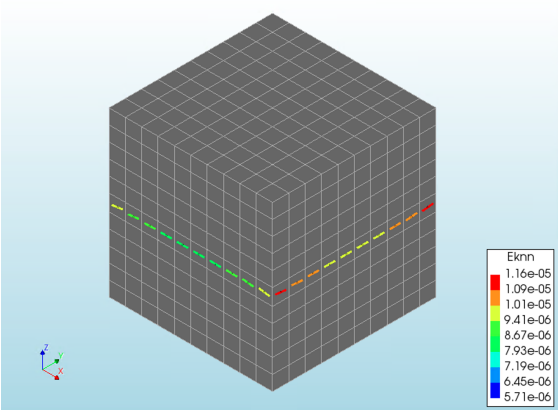

(a) t = 3 s

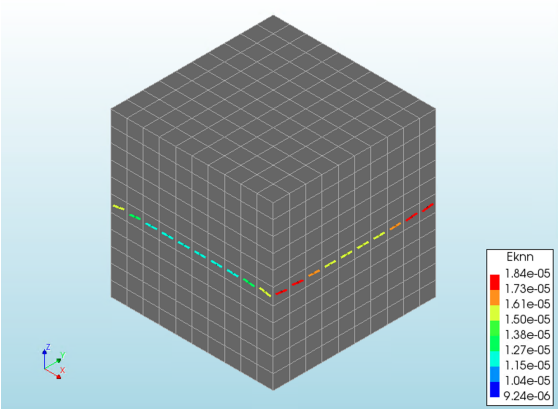

(b) t = 4 s

Figure 5.14: Crack strain development (ε_n) for method 1.

Method 2

For the analysis according to method 2, the middle layer is assigned the 'weak' rock properties and the JRC has been set at 13. Figure 5.15 shows the evolution of the principal strain (ε_1), permeability, pore pressure and Darcy flux along the contour probe. And Figure 5.16 shows the formation of a horizontal crack plane in the middle layer according to the Total Strain crack model. This crack plane first starts developing at t = 3 s.

The results generated by method 2 are very similar to the simulation according to method 1. Absolute values in permeability increase and Darcy flux differ a little bit but this can most likely be attributed to the choice in method-dependent input parameters. The simulation according to method 2 also shows the first crack development at t = 3 seconds (see Figure 5.15a when ε_1 exceeds ε_1) and a corresponding increase in the permeability can be observed (Figure 5.15b).

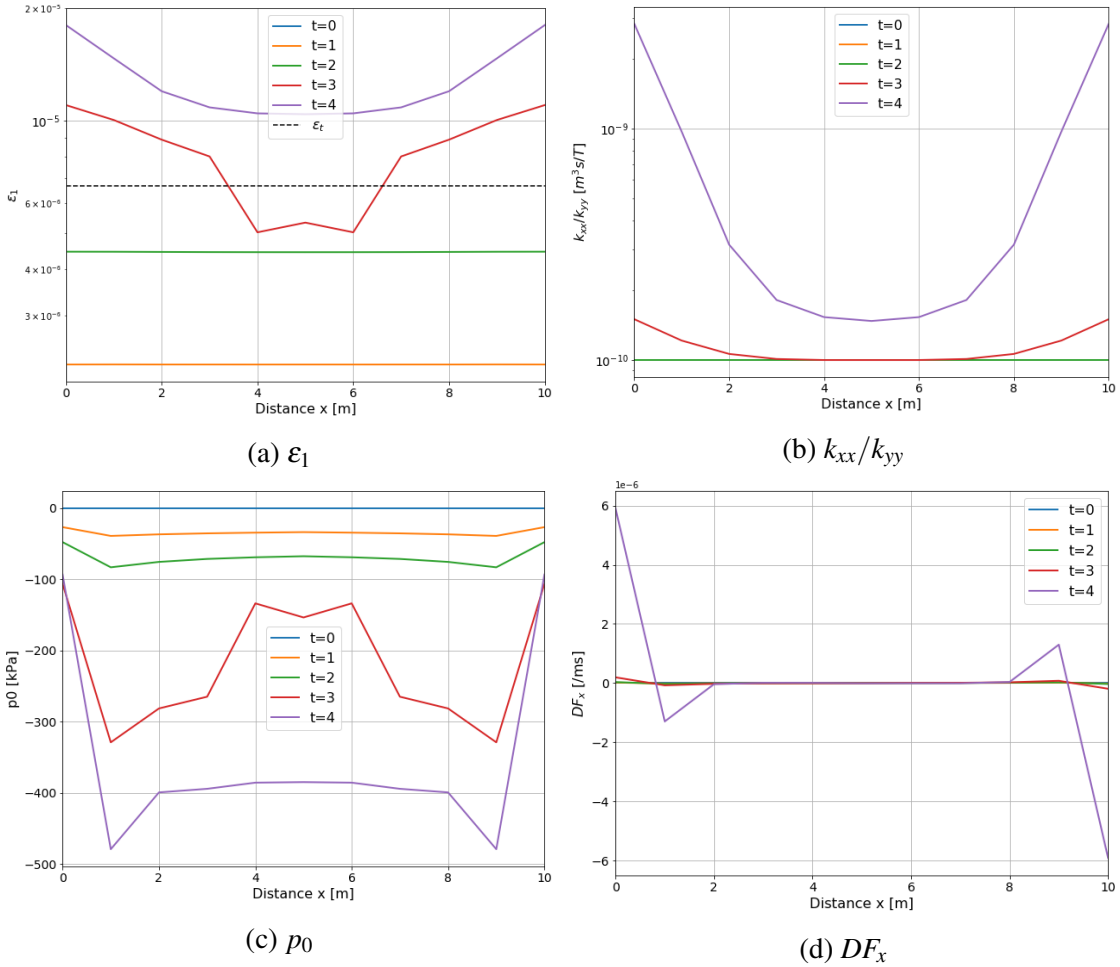

(a) ε_1

(b) k_{xx}/k_{yy}

(c) p_0

(d) DF_x

Figure 5.15: Development of principal strain, permeability, pore pressure, and Darcy flux along the contour probe for method 1.

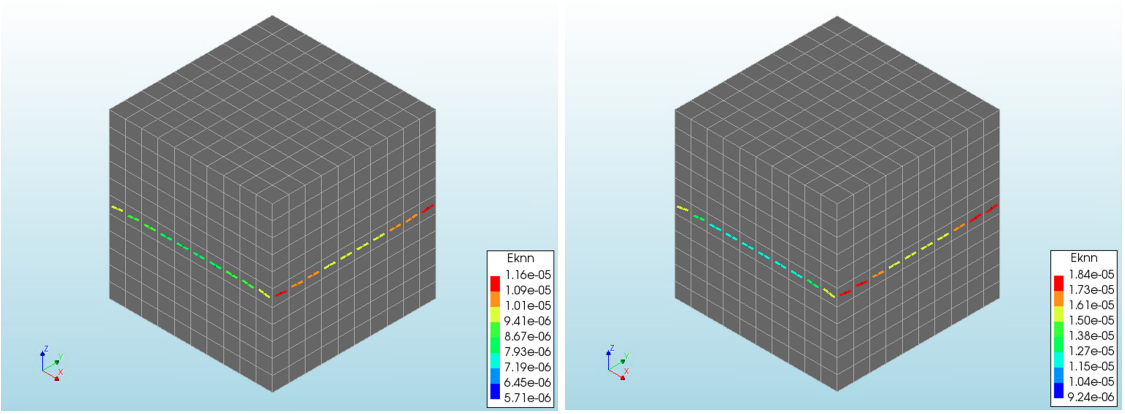

(a) t = 3 s (b) t = 4 s

Figure 5.16: Crack strain development (ε_n) for method 1.

The results according to both methods show that the development and the directionality of the permeability increase is in accordance with the direction of cracking as indicated by the Total Strain crack model. Both the fracture-dependent permeability model and the Total Strain crack model show the development of a horizontal fracture plane in the middle layer, which leads to an increase in both k_{xx} and k_{yy}. Although it has not been illustrated in the diagrams, k_{zz} remains constant at its initial for both methods 1 and 2 during the analysis. This is as expected, since a crack is formed orthogonal to the z-direction, and thus the permeability will not increase in this direction.

When comparing the results generated by the two methods, the simulations show many similarities, apart from small differences in absolute values for the permeability and Darcy flux increase. However, it should be noted that this most likely can be attributed to the definition of the method-dependent input parameters b_0 and JRC. Furthermore, it is also expected that the definition of the initial modified permeability field might influence the results, especially for method 2. A second thing that can be observed, is that the evolution of the permeability in space (along the contour probe) is a little more gradual for method 2 than for method 2. This is especially noticeable at the onset of cracking (t = 3 s).

5.4 Conclusion

The results of this chapter demonstrate and verify the workings of the model as proposed in Chapter 4 for both method 1 and 2. A 2D test case consisting of plane-strain elements is evaluated in Section 5.2, showing the rotation of the crack axes and hence the modified permeability during the analysis. The absolute values in permeability increase at the end of the analysis according to the numerical simulations by the fracture-dependent permeability model are verified by comparing them to a simple analytical analysis. A 3D test case is evaluated in Section 5.3, showing that the simulations by the fracture-dependent permeability model can be used alongside with the Total Strain crack model. Both models showed the development of a horizontal fracture plane through the middle layer of the block.

The important takeaways that can be concluded from the results of these first simple test cases are:

1. The fracture-dependent permeability model, including its two methods, has been implemented correctly. Simulation first of all show the expected rotation of the crack axes and corresponding increase in permeability with a rotating stress-strain field, and secondly, the absolute values of the permeability increase at the end of the analysis have been verified by comparing them with an analytical calculation.
2. The fracture-dependent permeability model can be assigned in combination with the rotating, Total Strain crack model, showing similar crack development during the three-dimensional analysis.
3. A noticeable qualitative difference between the two methods is the difference in permeability evolution, whereas method 1 shows a very responsive jump in permeability increase at the onset of cracking, method 2 shows a more gradual increase. It could be argued that either one of the representations of the permeability increase is correct depending on the type of fracture development.
4. These first results have also provided an indication of the model sensitivity to its input parameters: b_0 and JRC. Qualitative results between the two methods and between simulations having different input values can differ notably. A sensitivity analysis is therefore required to more appropriately map the influence of the input parameters on the solutions. The results of the sensitivity analysis will be discussed in the next chapter (Chapter 6). These first analyses also gave the impression that the model, primarily if defined according to method 2, might be fairly dependent on k_0'. The sensitivity analysis will therefore evaluate the extent of influence of the parameters: b_0 for method 1, JRC for method 2, and k_0' for both methods.

6. Hydraulic-fracturing analysis

6.1 Introduction

The purpose of this chapter is to compare the simulations of the fracture-dependent permeability model with a different numerical study on hydraulic fracturing, and to evaluate the objectivity of the generated results by investigating the mesh-dependency and the parameter sensitivity of the model.

The case description of the analysis, which forms the basis of this chapter, is based on the numerical study and field data which were part of a research on hydraulic fracturing in Lac du Bonnet granite by Souley et al. (2001) and AbuAisha et al. (2016). The results generated the numerical model developed by AbuAisha et al. (2016) are compared with the simulations produced by the fracture-dependent permeability model for both methods. Next, the analysis is re-executed (in Section 6.4) for a variety of mesh densities, thereby evaluating the response of the solution to different element sizes. And in Section 6.5 the influence of the method-dependent input parameters b_0 and JRC on the simulations is investigated. Besides that, the sensitivity analysis also looks at how the initial modified permeability affects the results for both methods. The main findings with respect to the model's objectivity are summarised and concluded on in the final section.

6.2 Simulations by Abuaisha et al. (2016)

The following sections describe a hydraulic-fracturing model (HFM) and a test case which has been employed for model verification by AbuAisha et al. (2016). The HF model forms part of a study on hydraulic fracturing in a thermo-poroelastic framework, and can simulate stable mode I fracture evolution. The findings of this numerical study, which incorporates an elaborate definition of fracture initiation and propagation, will be compared to simulations generated by the fracture-dependent permeability model in order to illustrate its applicability and identify its shortcomings.

6.2.1 Model description

For the illustration of the HF model, the author considers a situation as depicted in Figure 6.1. The vertical borehole crosses a rock formation, which is assumed to be homogeneous and isotropic regarding its elastic and transport properties.

Hydraulic fracturing is achieved by pumping pressurized fluid into the borehole until the maximum principal effective stress becomes tensile and exceeds the tensile strength of the rock. If cold fluid is injected in the rock, the consequent cooling of the rock mitigates the compressive stresses and will lead to an even more tensile effective tangential stress (σ'_ξ), resulting in fracturing of the rock if the tensile strength is exceeded. This process is illustrated in Figure 6.2.

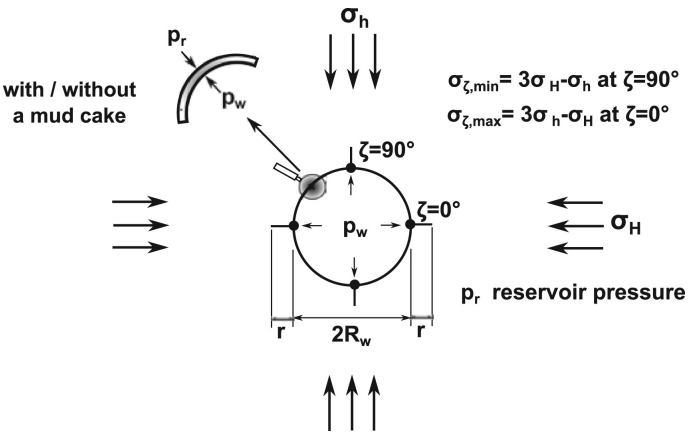

Figure 6.1: Hydraulic-fracturing situation displaying vertical wellbore and fractures (AbuAisha et al.).

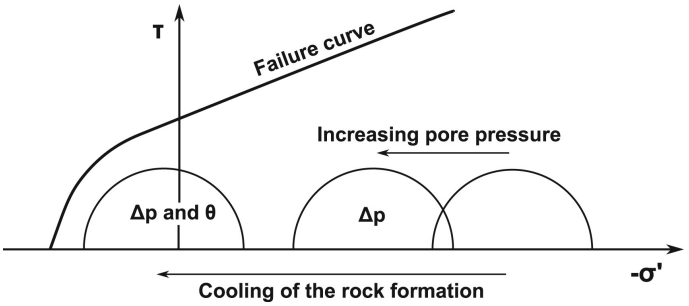

Figure 6.2: The effect of increasing pore pressure and decreasing temperature on hydraulic-fracturing, illustrated using Mohr's circles and a failure curve (AbuAisha et al., 2016).

AbuAisha et al. (2016) assume an initial group of fractures having an arbitrary average length (l) and a normal direction (n) in the horizontal plane. If the effective tangential stress in the fracture tip becomes tensile due to the increasing pore pressure and exceeds the rock material strength, the group of fractures is assumed to start propagating, and their apertures are expected to increase. The material strength is formulated in terms of material toughness parameter (K_{Ic}) because the stresses are evaluated in the crack tip, assuming only cracking mode I. The fracture criterion that is adopted to examine the initiation and propagation of the group of fractures is

$$F(\sigma'_n, l) = f(l)\sigma'_n\sqrt{\pi l} - K_{Ic} = 0, \tag{6.1}$$

where K_{Ic} is the material toughness of the material for mode I fracturing and $f(l)$ is a function that controls the fracture propagation and depends on l, l_f (critical fracture length) and η (fracture growth stabilization parameter). The fracture aperture is assumed to be a power function of the fracture length.

The overall permeability tensor of the fractured medium is defined as a summation of two separate parts: an initial permeability tensor (k_0) and a fracture-induced permeability tensor (k_{fr}). k_0 is assumed to remain constant throughout the analysis. Under the assumption that individual fractures are viewed as channels with parallel boundaries that can develop in any spatial direction (n), k_{fr} is obtained by averaging the individual flows over the considered spatial directions (assuming a local uniform pressure).

6.2.2 Analysis

AbuAisha et al. (2016) defined the following test case to validate its hydraulic-fracturing model (HFM) against experimental results by Souley et al. (2001) on the Lac du Bonnet granite:

A sample of the Lac du Bonnet granite is subjected to a triaxial compressive stress state (see Figure 6.3). The '-' sign indicates the compressive stresses. The sample is drilled at the centre, where pressurised fluid is injected. The pressure of the fluid is increased from 0 to 60 MPa. The parameters that were used in the HFM can be found in Table 6.1.

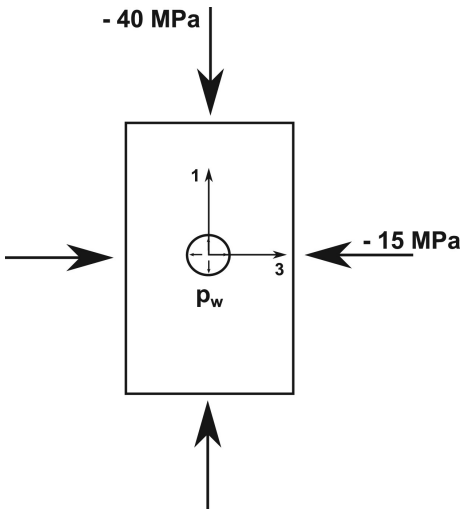

Figure 6.3: A parallelepiped sample of Lac du Bonnet granite is subjected to a triaxial compressive stress state. The out of plane stress is equal to -10 MPa (AbuAisha et al., 2016).

Table 6.1: Parameters used in the HF model (AbuAisha et al., 2016).

Parameter	**Value**	**Unit**
Drained Young's modulus E	68	GPa
Drained Poisson's ratio ν	0.21	-
Initial length of fractures l_0	3.0	mm
Final length of fractures l_f	9.0	mm
Material tensile strength T_c	8.3	MPa
Material toughness K_{Ic}	1.87	$MPa\sqrt{m}$
Fracture growth stabilizing parameter η	1.6	-
Fracture density	$2 \cdot 10^6$	$1/m^3$
Constant c_c*	0.0001	-
Initial permeability k_0	10^{-21}	m^2

*The positive constant c_c is a value that defines the microstructure of the damaged material. For this HFM it is used in an attempt to indicate that the connectivity of the fractures increases as they propagate.

The analytical solution that defines the initiation of hydraulic fracturing in the presence of a mud cake is formulated as following (Fjar et al., 2008):

$$p_w^{HF} - p_r^{\infty} = \sigma_H - 3\sigma_h - p_r^{\infty} + \frac{E}{1-\nu}\frac{\alpha}{3}\theta + T_c \tag{6.2}$$

where θ is the change in temperature in the rock and p_r^{∞} is the geostatic rock formation pressure. The pore pressure required to initiate the fracturing is calculated using Equation (6.2). Assuming no temperature change, σ_H = -40 MPa, σ_h = -15 MPa and T_c = 8.3 MPa, p_w^{HF} thus equals -40 - - 3 · 15 + 8.3 = 13.3 MPa. AbuAisha et al. (2016) determined the stabilizing parameter η at 1.6 such that the fractures start propagating at a pore pressure of 13.3 MPa. This stabilizing parameter controls the fracture propagation function ($f(l)$) (see Equation (6.1)).

6.2.3 Results

Figure 6.4 shows the results of the analysis that were produced by the HF model, where k_{11} is the permeability in the major principal direction and k_{33} in the minor principal direction. From 6.4a it is visible that hydraulic fracturing initiates at p_w = 13.3 MPa, showing an increase in permeability from 10^{-21} to approximately 10^{-16} when at point B fractures in all directions have reached their final length ($l = l_f$). The most notable increase in permeability takes place within the interval $p_w \in [15, 24]$ MPa. There is an initial preference for fracture propagation in the direction of the major principal stress, resulting in k_{11} to increase significantly with respect to k_{33}. The ratio k_{11}/k_{33} reaches a maximum of 1.6 at point C and decreases to 1 as the pore pressure increases and is dominant over the anisotropic stress field.

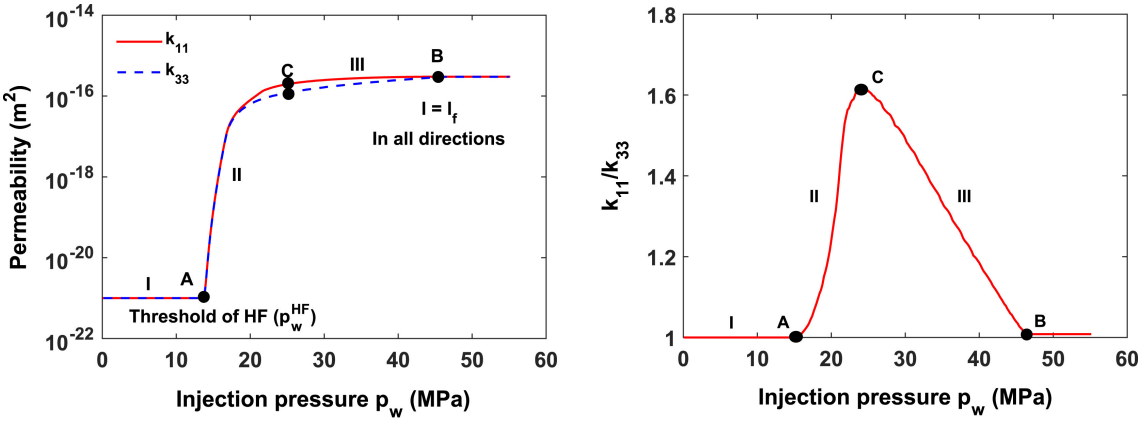

(a) (b)

Figure 6.4: The results generated by the HF model (AbuAisha et al., 2016), where (a) shows the permeability development with increasing fluid pressure and (b) the ratio between the permeability evolution in the major principal (k_{11}) and minor principal (k_{33}) direction.

The HF model, as defined by AbuAisha et al. (2016), is capable of simulating stable fracture evolution and corresponding fracture-induced permeability increase near a borehole. It assumes an initially fractured state, with fractures having an arbitrary direction n. The contributions to the overall permeability of groups of fractures with different directions are averaged. The fracture-dependent model proposed in this study can model a maximum of three orthogonal cracks directions (two in a 2D case) at one point. However, the directions in different points do not depend on one another. The total number of directions is therefore endless, but the model does not account for possible crack connectivity. Furthermore, the contribution of individual cracks to the overall permeability is not

averaged but instead is evaluated separately.

Fracture initiation and propagation are evaluated in the crack tip, and for that reason, the fracture criterion is formulated as a function of the material toughness parameter (K_{Ic}). The employed fracture criterion requires several additional input parameters such as an initial fracture length (l_0), final fracture length (l_f), growth stabilising parameter (η), fracture density and a constant (c_c) defining the microstructure of the damaged material. The growth stabilising parameter is calibrated such that the numerical solution for the initiation of hydraulic fracturing matches the analytically determined hydraulic-fracturing pressure (p_w^{HF}). The fracture-dependent model, as proposed in this study, does not evaluate crack initiation in the tip but instead evaluates cracking based on the tensile strength of the material. For method 1, it similarly assumes an initially crack state of the medium and therefore requires an additional state variable in the form of an initial aperture (b_0). This parameter is comparable to the initial fracture length (l_0). Method 2, on the other hand, does not necessarily assume an initial presence of fractures. The definition of the permeability tensor as a summation of the initial and fracture-induced permeability for the HF model is similar to method 2.

The description of the numerical boundary value problem in the study by AbuAisha et al. (2016) is fairly brief and does not include a mentioning of the model discretisation and dimensions. This makes it slightly more challenging to replicate the study and enforces the assumption of certain conditions.

6.3 Simulations by fracture-dependent permeability model

This section covers the simulation of the simplified hydraulic fracturing test case according to the fracture-dependent permeability model as proposed in this study. The analysis will be performed for both method 1 and 2 and compared to the findings of the numerical simulation executed by AbuAisha et al. (2016). The purpose of the comparison is to examine to what extent the results generated by two different methods show similarities with the more detailed numerical study. By doing so, the applicability of the model can be illustrated and its shortcomings identified.

Due to the in some cases limited information that was provided by AbuAisha et al. (2016) with regards to the description its numerical analysis, assumptions have been made concerning specific parameters and problem dimensions. These will be explained in the next section.

6.3.1 Analysis

The triaxial test state and the fluid injection of the granite sample are represented by circular domain with a radius of 1 m and the borehole having a radius of 0.1 m. The total vertical depth of the borehole is 1 m, and it has an inclination angle of 0°. The model is represented by a full mesh consisting of 'complete plane strain' elements (12 elements in the radial direction and 32 in the tangential direction, with a size factor of 10 in the radial direction). See Figure 6.5 for the model dimensions. The smallest elements are found at the edge of a borehole having dimensions of approximately 0.02 x 0.02 m. The elements increase in size in the radial direction. The largest elements can be found at the model boundary. These elements have dimensions of 0.15 x 0.2 m (width x height).

The complete plane strain assumption is a generalisation from the standard plane strain assumption and satisfies the following conditions (DIANA FEA bv, 2019):

1. Every cross-section is a plane of symmetry for the geometry of the structure;
2. The stresses and strains are independent of the coordinate along the out-of-plane axis.

Complete plane strain elements are an assumption to pseudo three-dimensional problems and differ from standard plane strain elements by removing the restriction on out-of-plane displacements and shear stresses, meaning that the out-of-plane strain does not necessarily equal zero, but can be defined as a constant value or a function. The 'complete plane strain concept' therefore produces a full three-dimensional stress and strain tensors (DIANA FEA bv, 2019).

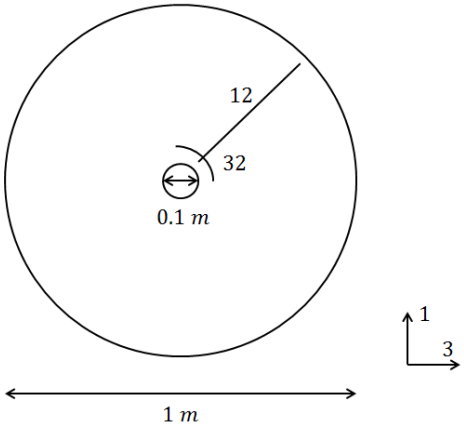

Figure 6.5: Model dimensions. The mesh consists of 12 elements in the radial direction and 32 in the tangential direction.

The initial conditions and rock stresses are given in Table 6.2. The mud pressure in the borehole is increased from 0 MPa at t = 0 days to 60.0 MPa at t = 60 days (install time) by increasing the applied pressure potential linearly with time at the inner boundary of the domain. The pore pressure at the outer boundary of the domain is kept constant at 0 MPa. For illustration, the pore pressure potential distribution at t = 10 days is given in Figure 6.6. It can be seen that at t = 10 days, the pore pressure potential at the borehole edge is equal to 10 MPa, and at the outer edge, the pore pressure is and will remain constant at 0 MPa.

Table 6.2: Initial conditions and rock stresses of the borehole analysis.

Parameter	**Value**	**Unit**
Pore pressure gradient	0.0	MN/m^3
Vertical total stress gradient	10	MN/m^3
Horizontal total stress gradient in x-direction	15	MN/m^3
Horizontal total stress gradient in y-direction	40	MN/m^3

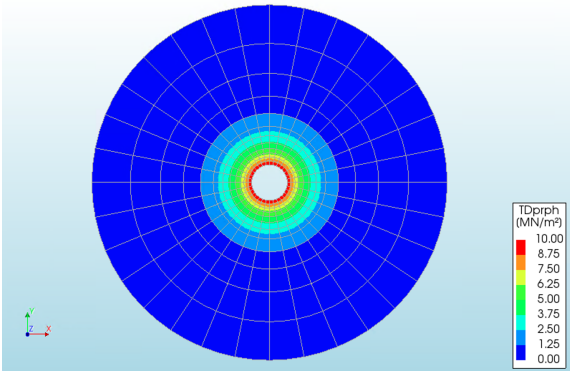

Figure 6.6: Pore pressure potential distribution in the domain at t = 10 days.

The fracture-dependent permeability model as proposed by this study requires different input parameters than the HFM by AbuAisha et al. (2016). These input values were based on the parameters used in the numerical studies on granite by Souley et al. (2001), Shao et al. (2005) and AbuAisha et al. (2016)). The parameters can be found in Table 6.3. The choice for the method-specific parameters b_0 and JRC, will be discussed in more detail in their corresponding sections.

Table 6.3: Material properties used to describe the isotropic rock material in combination with the fracture-dependent permeability model (Souley et al., 2001; Shao et al., 2005 and AbuAisha et al., 2016).

	Parameter	**Value**	**Unit**
General	Young's modulus E	68	GPa
	Poisson's ratio ν	0.21	-
	Porosity n	0.1	-
	Bulk modulus solid K_s	50	GPa
	Bulk modulus fluid K_f	2.2	GPa
Fracture-dependent permeability model	Initial permeability k_0	$1 \cdot 10^{-21}$	m^2
	Dynamic vsicosity μ	$3 \cdot 10^{-10}$	MPa s
	Initial aperture b_0	$3 \cdot 10^{-8}$	m
	JRC	9	
	Tensile strength f_t	8.3	MPa

The fracture criterion is formulated as a strain criterion, being a function of the material's tensile strength and Young's modulus,

$$\varepsilon \geq \varepsilon_t = \frac{f_t}{E}, \tag{6.3}$$

6.3.2 Results

The results according to method 1 and 2 have been evaluated in the major and minor principal stress direction for the total duration of the analysis. See Figure 6.5 in the previous section for the direction of the major and minor principal stresses. k_{11} indicates the permeability in the major direction and k_{33} in the minor direction. For clarification, unless stated otherwise, if the results refers to either k_{11} or k_{33}, the number indicates the observed maximum value of the permeability in the entire domain in the major or minor direction respectively.

Anisotropic stress field

The in-situ stress field is anisotropic. The degree and direction of the anisotropy influences the fracture development and the corresponding permeability evolution. The crack criterion is strain-dependent and has been defined as a function of the tensile strength of the rock and its Young's modulus (see Equation (6.3)). Because f_t = 8.3 MPa and E = 68 GPa, the tensile strain threshold for fracturing is equal to 8.3/6800 = $1.22 \cdot 10^{-4}$. Extensional fractures are expected to occur in the direction of the maximum principal stress (σ_H) when the principal strain exceeds this threshold. This observation is in agreement with the development of fractures at the edge of a borehole, as explained in Chapter 2. A large maximum principal confinement (σ_H) and a considerable formation pressure (σ_v) advance fracture growth in the direction of σ_H, whereas a large minimum principal confinement (σ_h) and high tensile strength hinder fracture development (AbuAisha et al., 2016). The influence of the existing stress field on fracture development has been illustrated in the Figures 6.7a, 6.7b and 6.7c below. The figures illustrated the development of the deformation zone in terms of the primary principal strain (E_1). Because the fracture criterion has been defined as a strain threshold, fractures and permeability development will be observed in high deformation zones. The figures correspond with the following stress fields:

- Figure 6.7a: The maximum principal confinement (σ_H) coincides with the y-direction. Extensional fractures will therefore develop (mainly) in the direction of the y-axis resulting in an increase in k_{11}.
- Figure 6.7b: The maximum principal confinement (σ_H) coincides with the x-direction. Extensional fractures will therefore develop (mainly) in the direction of the x-axis resulting in an increase in k_{33}.
- Figure 6.7c: The maximum principal confinement (σ_H) coincides with the y-direction, nonetheless, due to a relatively greater in confinement in the minor principal direction (x-direction), the development of the extensional fractures in the direction of the y-axis will be less distinct.

Note that Figure 6.7a is a representation of the test case presented in this analysis.

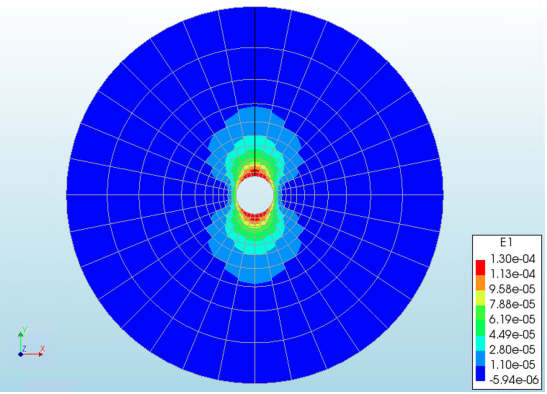

(a) σ_H (y) = -40 MPa, σ_h (x) = -15 MPa and σ_v = -10 MPa.

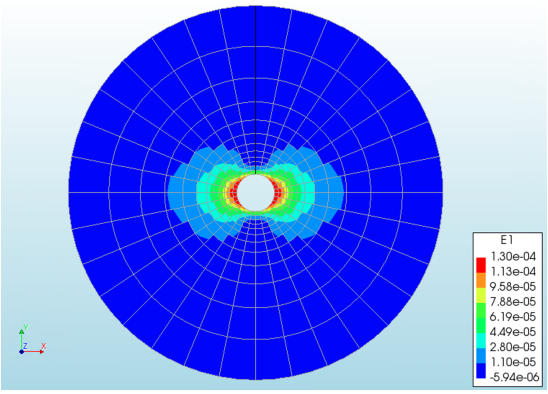

(b) σ_H (x) = -40 MPa, σ_h (y) = -15 MPa and σ_v = -10 MPa.

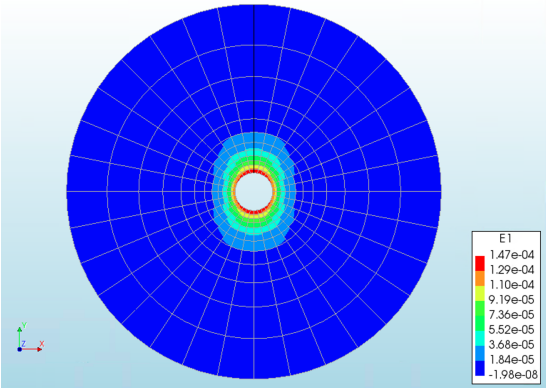

(c) σ_H (y) = -40 MPa, σ_h (x) = -30 MPa and σ_v = -10 MPa.

Figure 6.7: Principal strain at the onset of fracturing.

Method 1

The definition of the fracture-dependent permeability according to method 1, requires an additional input parameter in the form of a theoretical initial aperture b_0. Shao et al. (2005) state that due to the formation history of brittle rocks, it is not unlikely for them to have pre-existing cracks, which actually should be taken into consideration. In their study they, therefore, define an initial fracture length (l_0), which is estimated at 3 mm, in correspondence with the average grain size of the Lac du Bonnet granite (Shao et al., 2005). According to Kranz (1983), the length/width ratio of microcracks generally lies between 10^-3 and 10^{-5}. For that reason, if l_0 is determined at 3 mm, an estimation of b_0 would lie between $3 \cdot 10^{-6}$ and $3 \cdot 10^{-8}$ m.

When the analysis is performed for $b_0 = 3 \cdot 10^{-8}$ m, the simulation shows quite some agreement with the results produced by the HFM by AbuAisha et al. (2016), see Figure 6.8a. The permeability development in the major (k_{11}) and minor (k_{33}) principal direction as the fluid pressure in the borehole increases from 0 to 60 MPa has been plotted separately in Figure 6.8b, and the ratio between k_{11} and k_{33} can be seen in Figure 6.8c.

Hydraulic fracturing occurs at p_w = 15-16 MPa (point A in Figure 6.8b) when the initial increase in permeability is observed. k_{11} jumps to a value of around $1 \cdot 10^{-17}$ m^2 in point C at the onset of fracturing. k_{33} shows a smaller increase, reaching an initial value of approximately $3 \cdot 10^{-20}$ m^2. At that moment, the ratio between k_{11} and k_{33} reaches

its maximum value of a little over 400. From point C to B, both permeabilities display a stagnating increase, reaching almost equal final values of $1.7 \cdot 10^{-16}$ and $1.4 \cdot 10^{-16}$ m^2 for k_{11} and k_{33} respectively. These values result in a ratio of approximately 1.2 at the end of the analysis.

When comparing these results with the result generated by the HFM by AbuAisha et al. (2016), see Figure 6.8a, similarities that show are, first of all, the increase in permeability to a final value of approximately $1 \cdot 10^{-16}$ m^2. Second of all, both simulations show the most significant increase in permeability within the interval $p_w \in [15, 24]$ MPa, and thirdly, the stagnating increase in the final phase is valid for both analyses. On the other hand, a notable difference is the slower development of k_{33} compared to k_{11}. At the initial moment of hydraulic fracturing, the increase in k_{33} is significantly smaller than k_{11}. They do approach almost equal values at t = 60 days, but the ratio is not entirely reduced to 1 again, even though this was expected to occur when the pore pressure in the borehole becomes greater than 40 MPa, and therefore should become dominant over the existing anisotropic stress field.

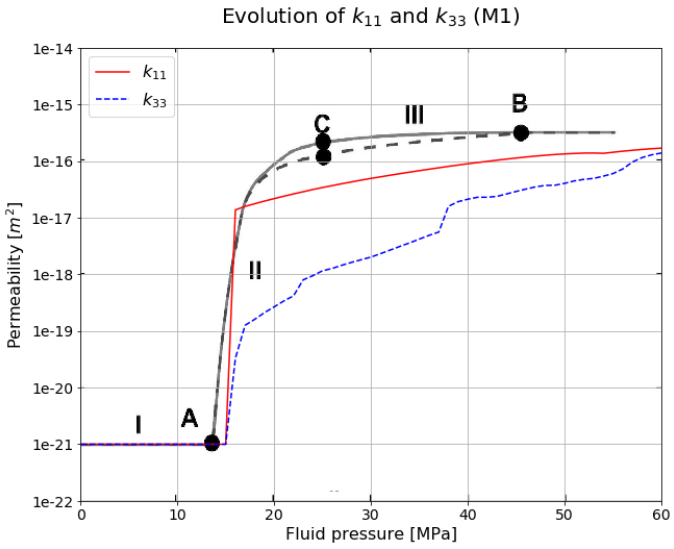

(a) Comparison of k_{11} and k_{33} evolution with simulations by AbuAisha et al. (2016).

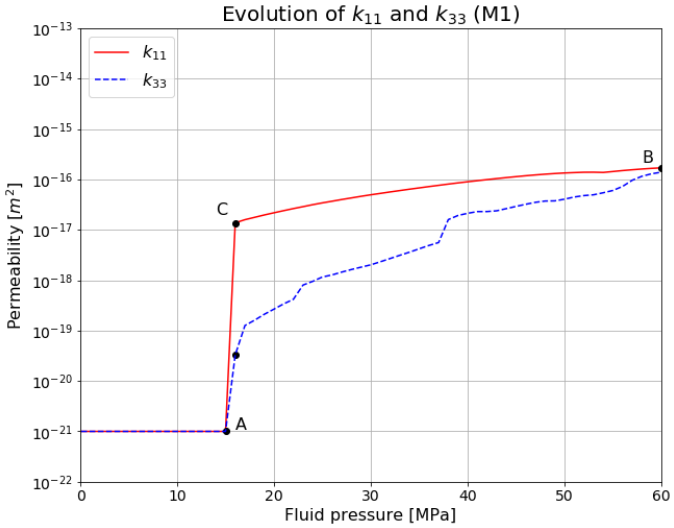

(b) Evolution of k_{11} and k_{33} with increasing fluid pressure.

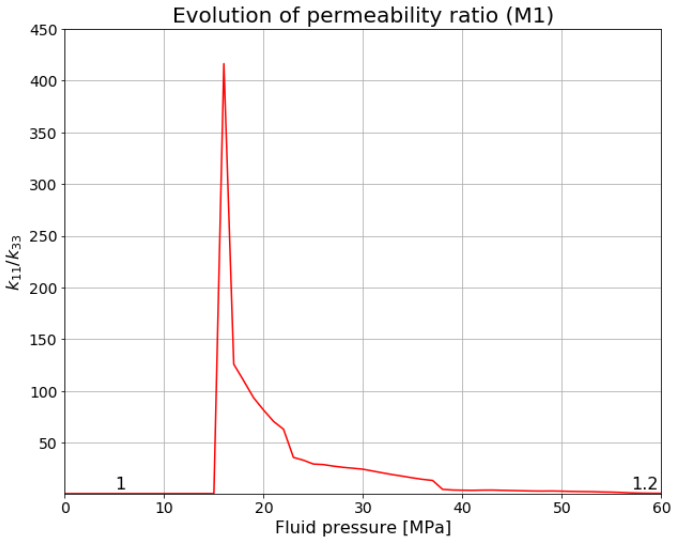

(c) Evolution of ratio k_{11} over k_{33} with increasing fluid pressure.

Figure 6.8: Results of HF analysis according to method 1 for $b_0 = 3 \cdot 10^{-8}$ m.

Figure 6.9 shows the pore pressure development along the contour probe at different times throughout the analysis for method 1. The applied pore pressure potential at the borehole edge (distance in y-direction = 0 m in Figure 6.9) is increased linearly with time: At t = 0 days it equals 0 MPa and at t = 60 days it is equal to 60 MPa. The pore pressure potential at the domain boundary (y = 0.9 m) will remain constant and equal to zero throughout the entire analysis. These boundary conditions correspond to the pore pressure development which is displayed in Figure 6.9. Furthermore, the fracture initiation and development can also be observed. At t = 16 days, the first cracks will form predominantly in the major principal direction. From that moment onward, a constant pore pressure is visible at the edge of the borehole propagating till a certain distance in the y-direction. This distance illustrates the crack length development, which is approximately equal to 0.1 m at t = 30 days and reaches a final length of 0.2 m at t = 60 days. Figures 6.10a and 6.10b show the contour plot of the pore pressure distribution over the entire domain at times t = 30 days and t = 60 days, respectively. These figures show that the initially crack development is predominantly in the y-direction (see Figure 6.10a). However, this becomes less pronounced as the analysis continues, which can be observed in Figure 6.10b, where pore pressure evolution is also observed in other directions.

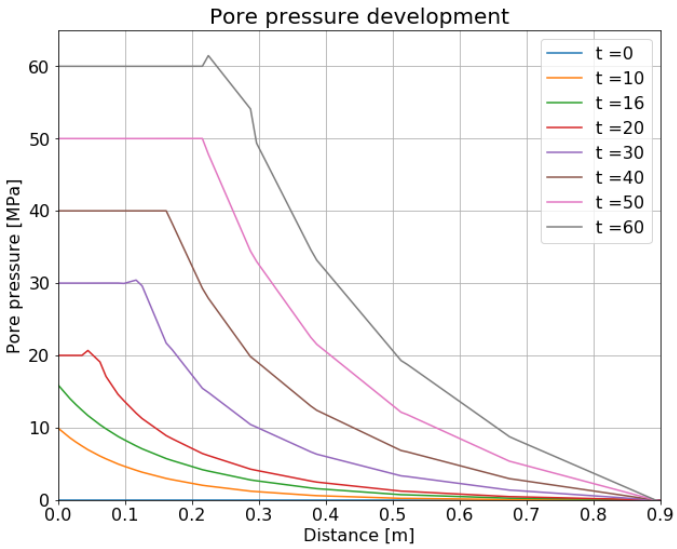

Figure 6.9: Pore pressure development along contour probe over time for method 1.

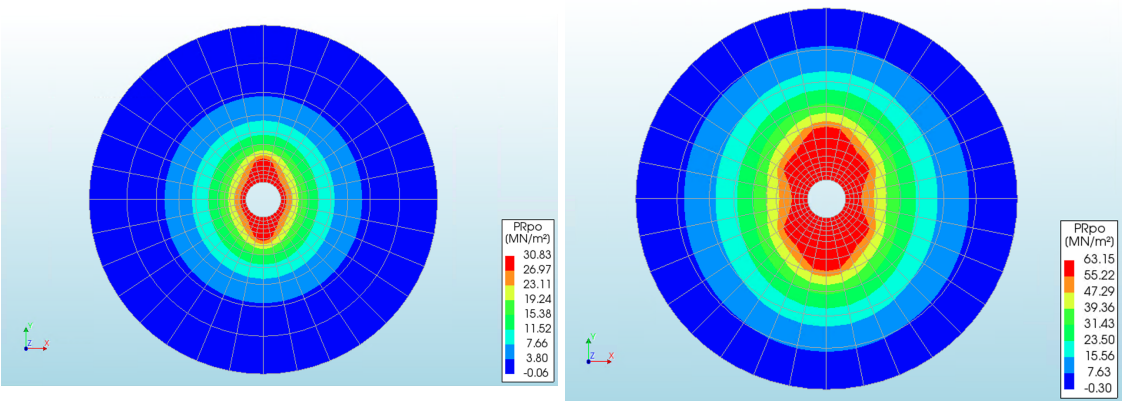

(a) t = 30 days

(b) t = 60 days

Figure 6.10: Pore pressures in the domain at different times for method 1.

Method 2

The definition of the fracture-dependent permeability according to method 2, requires an additional input parameter in the form of the joint roughness coefficient. The JRC has been estimated at an average value of 9 for granite (Barton and Choubey, 1977). The results of the corresponding analysis can be seen in Figure 6.11, where Figure 6.11a shows the comparison with the simulation performed by AbuAisha et al. (2016). The permeability development in the major (k_{11}) and minor (k_{33}) principal stress direction as the fluid pressure in the borehole increases from 0 to 60 MPa has been plotted separately in Figure 6.11b, and the ratio between k_{11} and k_{33} has been plotted in Figure 6.11c.

Hydraulic fracturing and a corresponding increase in permeability for both k_{11} and k_{33} are first observed when p_w = 15-16 MPa (point A in Figure 6.11b). However, the increase in k_{33} is less significant. The change in permeability shows less of a jump, in contrast to the results produced by method 1, but instead displays a more gradual increase, which stagnates when the fluid pressure approaches 60 MPa. k_{11} reaches a final value of approximately $1 \cdot 10^{-14}$ m^2 and k_{33} of $6 \cdot 10^{-15}$ m^2. The ratio reaches a maximum value of 300 at p_w = 20 MPa, after which it finally drops to a value of around 1.6.

When comparing it to simulations by AbuAisha et al. (2016), see Figure 6.11a, and to the results generated by method 1, this simulation shows a higher increase in permeability (factor 100 approximately) and a more notable difference between k_{11} and k_{33}. This greater increase in permeability can most likely be attributed to the estimation of the JRC. For method 1, b_0 has been calibrated to match the results of the numerical analysis by AbuAisha et al. (2016), whereas for method 2, an average value for the JRC for granite (Barton and Choubey, 1977) has been adopted. Furthermore, the permeability development at the onset of fracturing does not show a jump but instead follows a more steady increase. The most significant increase however is again observed within the interval $p_w \in [15, 24]$ MPa after which the progression stagnates.

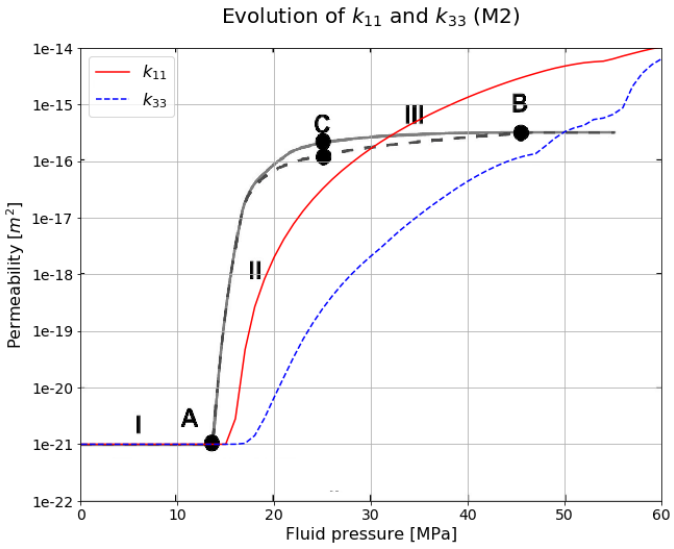

(a) Comparison of k_{11} and k_{33} evolution with simulations by AbuAisha et al. (2016).

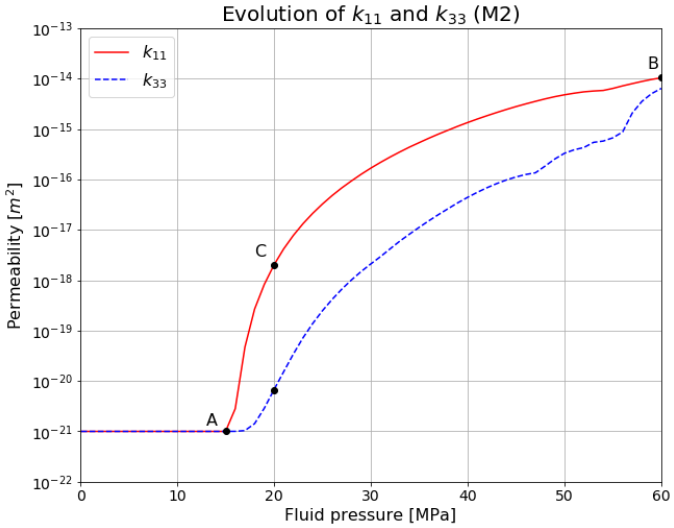

(b) Evolution of k_{11} and k_{33} with increasing fluid pressure.

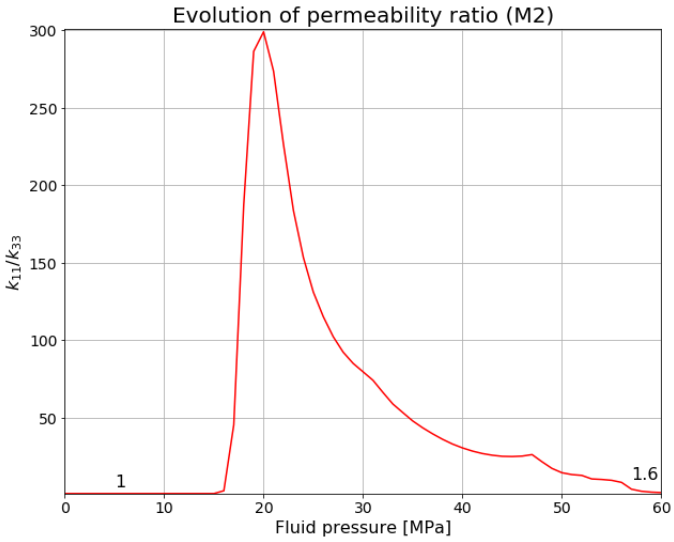

(c) Evolution of ratio k_{11} over k_{33} with increasing fluid pressure.

Figure 6.11: Results of HF analysis according to method 2 for JRC = 9.

Figure 6.12 shows the pore pressure development along the contour probe at different times throughout the analysis for method 2. This pore pressure development is very similar to the development according to method 1 (shown in Figure 6.12), where the same pore pressure development corresponding to propagating fractures at the edge of the borehole (y = 0 m) is observed from the moment of crack initiation onward (t = 16 days). The contour plots of the pore pressure development in the entire domain at t = 30 days and t = 60 days are displayed in Figures 6.13a and 6.13b, respectively. These diagrams depict the same fracture propagation, which is initially dominant in the major principal direction.

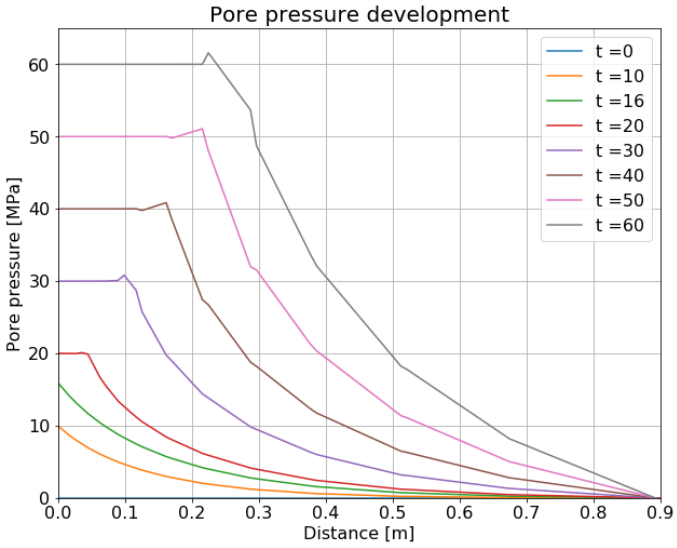

Figure 6.12: Pore pressure development along contour probe over time for method 2.

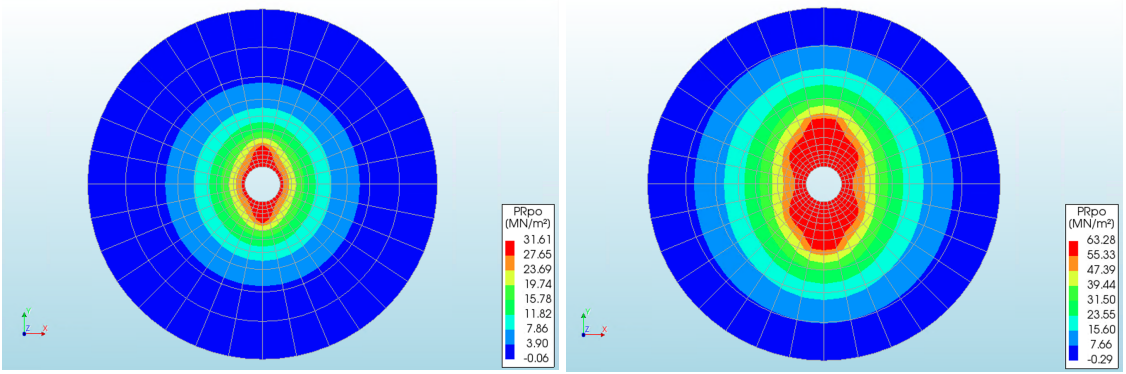

(a) t = 30 days (b) t = 60 days

Figure 6.13: Pore pressures in the domain at different times for method 2.

6.4 Mesh-dependency evaluation

An analysis will be performed evaluating the dependency of the solution on the definition of the element mesh. The number of elements is varied in the radial and tangential direction. Furthermore, a size factor is also applied to the mesh altering the size of the elements in the radial direction. The mesh elements are thus not of equal size, but are smaller near the borehole and increase in size when moving towards the perimeter of the model. The mesh dependency analysis is executed, and convergence of the solution is determined according to the following steps:

1. A rough mesh is created, using the fewest, yet reasonable number of elements and the corresponding solution of the model is analysed.
2. A finer mesh is created, consisting of smaller elements in both the radial and tangential direction. The solution is re-analysed, and results are compared with the simulation of the previous mesh.
3. The mesh density is increased, repeating the second step, until the change in results between meshes are limited, and hence the convergence of the solution is satisfactory.

The analysis has been performed for both method 1 and 2. For method 1, b_0 equals $3 \cdot 10^{-8}$ m, and for method 2 the JRC is equal to 9. The results; k_{11} and k_{33} at the initiation of hydraulic fracturing (the moment when the first change in permeability is observed) and the corresponding fluid pressure in the borehole are displayed in Table 6.4 for different mesh sizes. The results for different mesh sizes at the end of the analysis (t = 60 days and p_w = 60 MPa) can be found in Table 6.5. In Tables 6.4 and 6.4 M1/M2 corresponds to the results for method 1 and method 2, respectively.

The findings for k_{11} and k_{33} at t = 60 days have been visualised for both methods. In Figure 6.14a, the solution has been plotted versus the total amount of elements. When looking at these diagrams, it appears that the solution generated by method 1 converges slightly better than the solution according to method 2. Simulations according to both methods show that a finer mesh will consequently lead to a smaller increase in permeability. No complete convergence of the solution was found, not even for very fine meshes consisting of elements near the borehole having dimensions of 0.005 x 0.005 m (not indicated in the diagram).

The initiation of hydraulic fracturing (when the first changes in permeability are observed) is method-independent, and only deviates for very rough meshes. The hydraulic fracturing initiation pressure quickly converges to a value of 16/15 MPa when the mesh size is refined. The results are displayed in Figure 6.14b. This mesh-objectivity can be explained by the fact that the initiation of hydraulic fracturing mainly depends on the defined crack criterion. Cracking is initiated if the occurring strain exceeds the strain crack criterion, which depends on the tensile strength and Young's modulus of the material. Because those two material properties and the calculated strain field are mesh-independent, the initiation of hydraulic fracturing also shows no (to a little) mesh-dependency.

Table 6.4: Different mesh sizes and corresponding results of the permeability at the initiation of hydraulic fracturing (p_w^{HF}).

Mesh size	**Size factor (radial)**	**Nr. of nodes**	p_w^{HF} **[MPa]**	**M1:** k_{11} $[m^2]$	**M1:** k_{33} $[m^2]$	**M2:** k_{11} $[m^2]$	**M2:** k_{33} $[m^2]$
2x8	1	80	31	3.93E-15	2.23E-17	3.63E-19	3.06E-21
3x8	3	112	20	6.96E-16	2.48E-18	9.00E-20	1.27E-21
4x16	4	288	17	2.47E-16	1.32E-19	1.62E-21	1.00E-21
6x12	5	312	16	1.16E-16	4.80E-20	1.55E-21	1.00E-21
8x20	5	680	16	5.97E-17	7.23E-21	1.14E-20	1.00E-21
10x24	10	1008	16	2.21E-17	4.20E-20	3.48E-21	1.00E-21
12x32	10	1600	16	1.37E-17	3.30E-20	2.82E-21	1.00E-21
15x32	10	1984	16	1.01E-17	1.98E-20	2.51E-21	1.00E-21
18x36	12	2664	15	5.04E-18	3.42E-21	1.70E-21	1.00E-21
20x40	12	3280	15	4.98E-18	5.34E-21	1.68E-21	1.00E-21

Table 6.5: Different mesh sizes and corresponding results of the permeability at t = 60 sec and p_w = 60 MPa.

Mesh size	**Size factor (radial)**	**Nr. of nodes**	**M1:** k_{11} $[m^2]$	**M1:** k_{33} $[m^2]$	**M2:** k_{11} $[m^2]$	**M2:** k_{33} $[m^2]$
2x8	1	80	1.29E-14	1.07E-15	1.06E-11	8.79E-13
3x8	3	112	2.90E-15	1.75E-15	9.81E-13	3.24E-13
4x16	4	288	1.13E-15	1.04E-15	1.40E-13	1.01E-13
6x12	5	312	6.81E-16	6.36E-16	1.08E-13	7.89E-14
8x20	5	680	5.01E-16	3.90E-16	9.00E-14	3.93E-14
10x24	10	1008	2.69E-16	1.84E-16	2.25E-14	1.14E-14
12x32	10	1600	1.70E-16	1.39E-16	1.04E-14	6.39E-15
15x32	10	1984	1.25E-16	1.04E-16	5.34E-15	3.63E-15
18x36	12	2664	9.24E-17	6.12E-17	3.06E-15	1.27E-15
20x40	12	3280	6.84E-17	5.07E-17	1.58E-15	9.03E-16

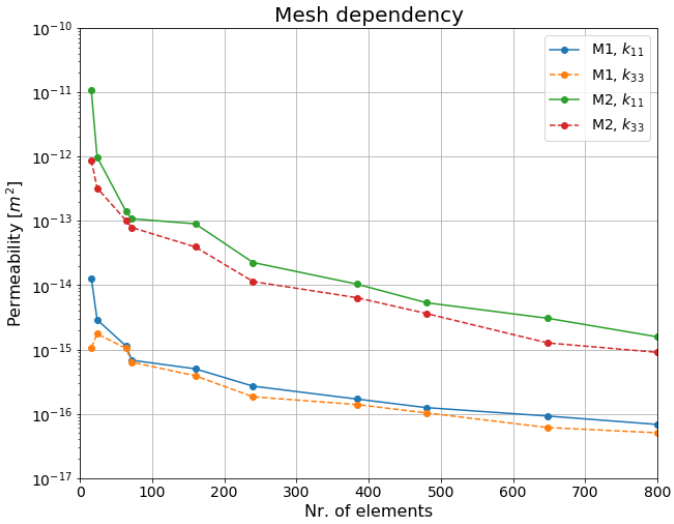

(a) Permeability solution at t=60 days.

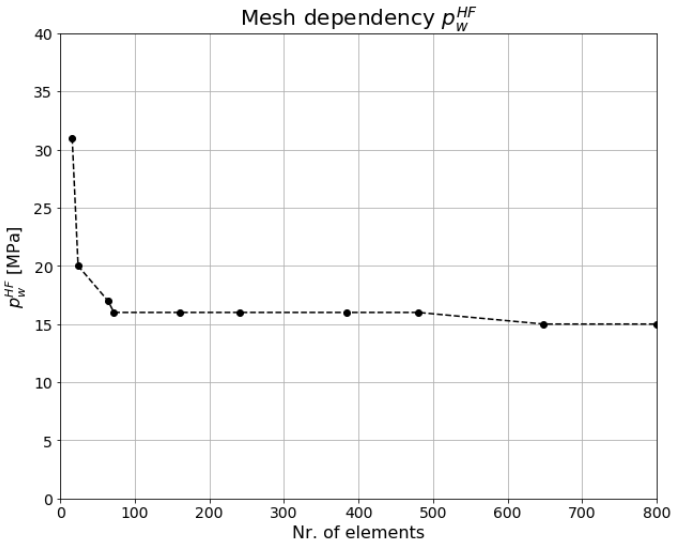

(b) p_w^{HF} solution for different mesh sizes.

Figure 6.14: Mesh dependency analysis.

A way of improving the model's mesh objectivity is investigated for method 1. Such an improvement is only considered for method 1, because an element size dependency can more straightforwardly be incorporated in the definition of b_0 than in the JRC value for method 2. This enhanced mesh-objectivity for method 1 is achieved by redefining b_0 as a function rather than a constant parameter. In this case, the parameter is formulated as a function of tensile strain and crack bandwidth,

$$b_0 = \varepsilon_t \cdot h_{crack} \cdot 0.01, \tag{6.4}$$

where the factor 0.01 has been applied for calibration. Because of the dependency on the crack bandwidth, which is a function of the element dimension and crack direction (according to Govindjee's projection method), b_0 differs per element in the model and has a smaller value for the smaller elements in the vicinity of the borehole. Figure 6.15 displays the results simulated by this solution. It can be argued whether it is appropriate to define a non-homogeneous value for b_0 if other initial state flow parameters, such as

k_0, are considered to be homogeneous in the entire domain. Nonetheless, this solution converges better than when b_0 is defined as a constant value for the whole model. The solution appears to have converged satisfactorily when a mesh consisting of 10x24 elements is used. The smallest dimension of the elements near the borehole is approximately 0.026 x 0.026 m (width x height), whereas the largest elements, which can be found at the perimeter of the model, have a dimension of 0.2 x 0.26 m.

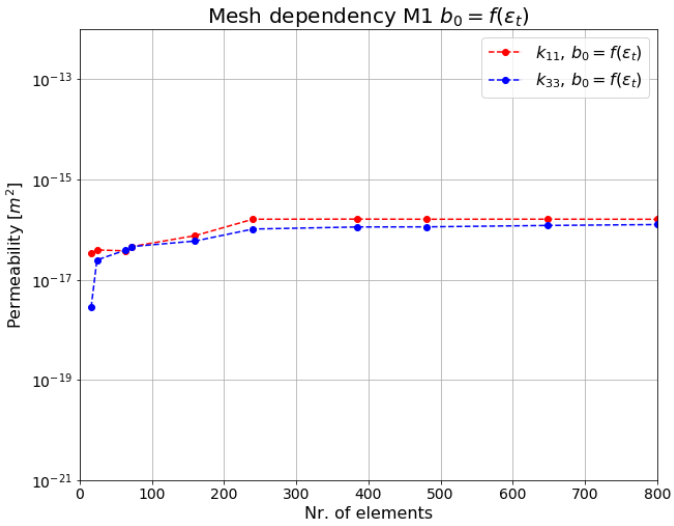

Figure 6.15: Permeability solution at t=60 days and p_w = 60 MPa for different mesh sizes when b_0 is defined as a function according to Equation (6.4).

6.5 Parameter-sensitivity evaluation

A parameter investigation has been performed to evaluate the sensitivity of the model to the method-dependent additional parameters, being the initial aperture (b_0) and the Joint Roughness Coefficient (JRC). Furthermore, the dependence on the definition of the initial permeability has also been evaluated. The analyses have been executed using the mesh consisting of 12x32 elements (as described in the previous section).

The results have been evaluated along a contour probe, which starts at the edge of the borehole in node 401, and continues to the perimeter of the model in the y-direction (see Figure 6.16). The permeability results are investigated at the end of the 'install time' (t = 60 days) when the fluid pressure inside the borehole equals 60 MPa.

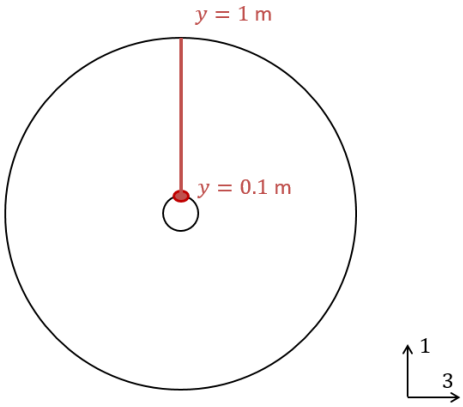

Figure 6.16: Model showing the defined y-axis along which results are evaluated.

Initial aperture

For method 1, the influence of the initial aperture on the results has been evaluated. b_0 ranges from $1 \cdot 10^{-5}$ m - $1 \cdot 10^{-9}$ m while keeping all other parameters constant. Because of the uncertainty in determining this (theoretical) parameter a broad range has been defined, thereby also accounting for the definition of the length/width ratio 10^{-3} - 10^{-5} of microcracks, as suggested by Kranz (1983).

The results of k_{11} and k_{33} along the defined contour probe have been plotted for the different input values of b_0 in Figure 6.17. The graph shows that magnitude of the permeability input is very sensitive to b_0, which was not unexpected, as it had already been suggested by Chen et al. (2007) and because the permeability is defined as a quadratic function of b_0 in the proposed model. Furthermore, the graph shows that the radial distance to which the increase in permeability (and hydraulic fracturing) extends, almost does not depend on b_0, but is fixated at 0.4 m. Except for the largest value of $b_0 = 1 \cdot 10^{-5}$ m, when only a minimal increase in k_{11} is indicated in approximately the first 0.15 to 0.3 m (different for k_{11} and k_{33}). It can be observed that if the initial aperture value is sufficiently small (smaller than $b_0 = 1 \cdot 10^{-5}$ m in this case), the spatial extent of the permeability development only depends on the defined strain crack criterion, which is the same for all the analyses. And thus the spatial extent of the permeability evolution is not affected by b_0.

Figure 6.18 shows the development of k_{11} and k_{33} when b_0 is defined as a function instead of a constant value, where n is a factor as applied in Equation (6.4). These results indicate similar sensitivity and contour plots to previous findings when b_0 is defined as a model constant input parameter.

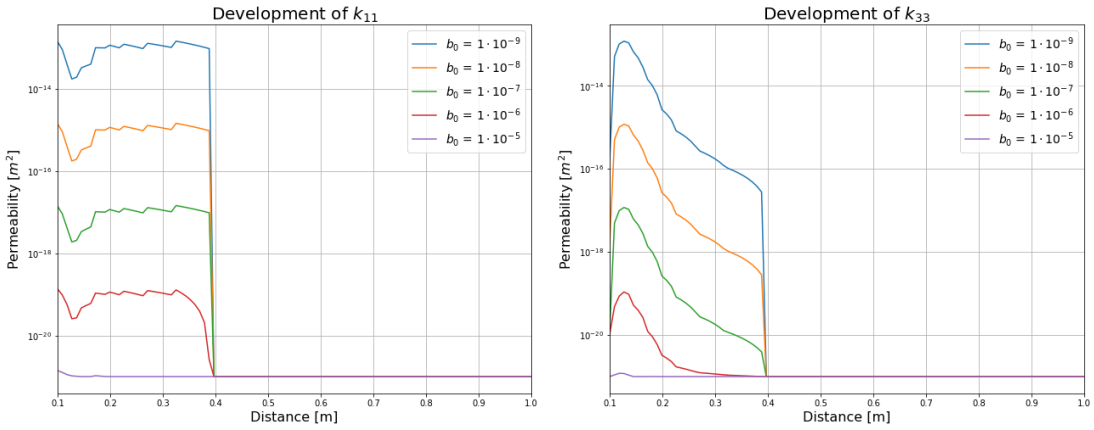

(a) k_{11} (b) k_{33}

Figure 6.17: Development of permeability along the defined axis for b_0 is constant in the model.

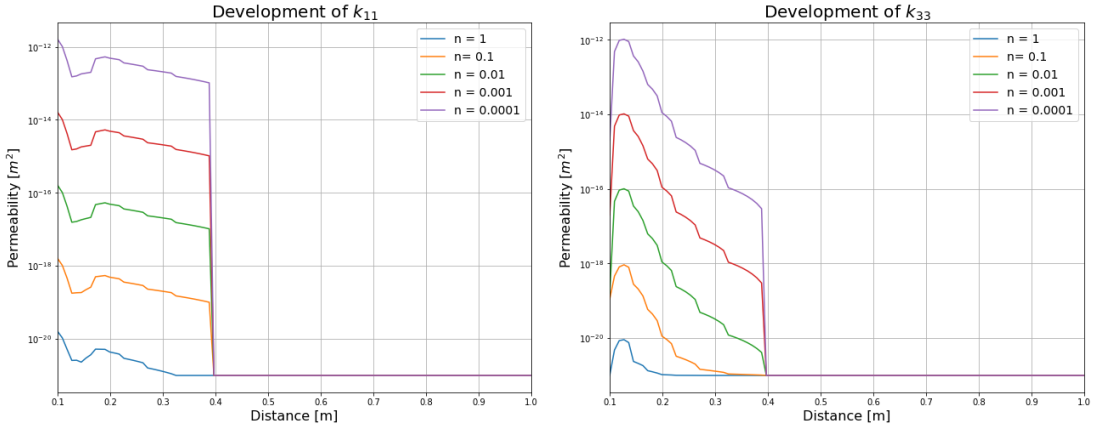

(a) k_{11} (b) k_{33}

Figure 6.18: Development of permeability along the defined axis for b_0 as a function of the tensile strain and crack bandwidth (n is a factor as defined in Equation (6.4)).

Figure 6.19 clearly shows the linear relation between b_0 and k_{11}, as well as k_{33}, in the log-log space. In this case, b_0 is defined as a singular value. The maximum values for k_{11} and k_{33} located along the defined axis at t = 60 days have been taken into account for this analysis. Moreover, interesting to observe is that the maximum values for k_{11} and k_{33} are almost equal, even though they do not occur at the same distance from the borehole (see Figure 6.17).

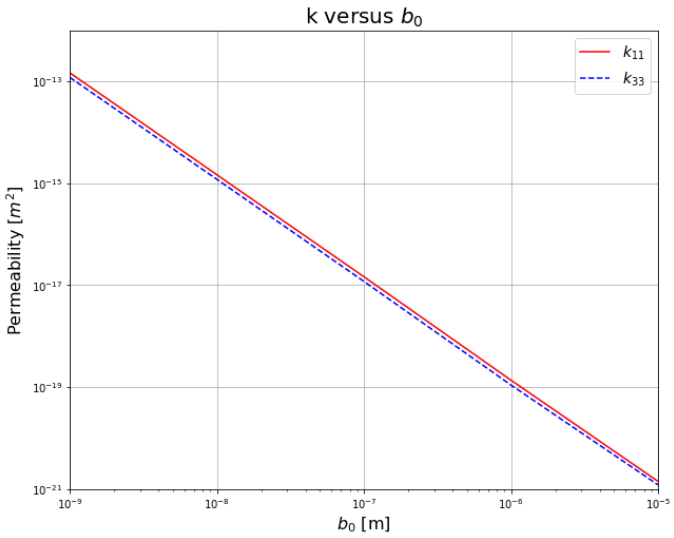

Figure 6.19: Maximum permeability along the defined axis at the end of install time for different values of b_0.

Joint roughness coefficient

For method 2 the influence of the joint roughness coefficient on the results has been evaluated. The JRC ranges from 1 (smooth, parallel walls) - 20 (rough, undulating walls), while keeping all other parameters constant.

The results have been plotted for k_{11} and k_{33} along the contour probe for different values of JRC (see Figure 6.20). It can be observed that the model is quite sensitive to the JRC, displaying a range in simulated permeabilities approximately 10^{-10} m^2 and 10^{-16} m^2. However, as JRC increases, the difference in results becomes less pronounced, and the solution seems to approach a value of approximately 10^{-16} m^2 for both k_{11} and k_{33}. The range to which the permeability increase extends is constant and reaches a maximum value of 0.4 m. However, a permeability decline is observed for all values of the JRC when moving further away from the borehole.

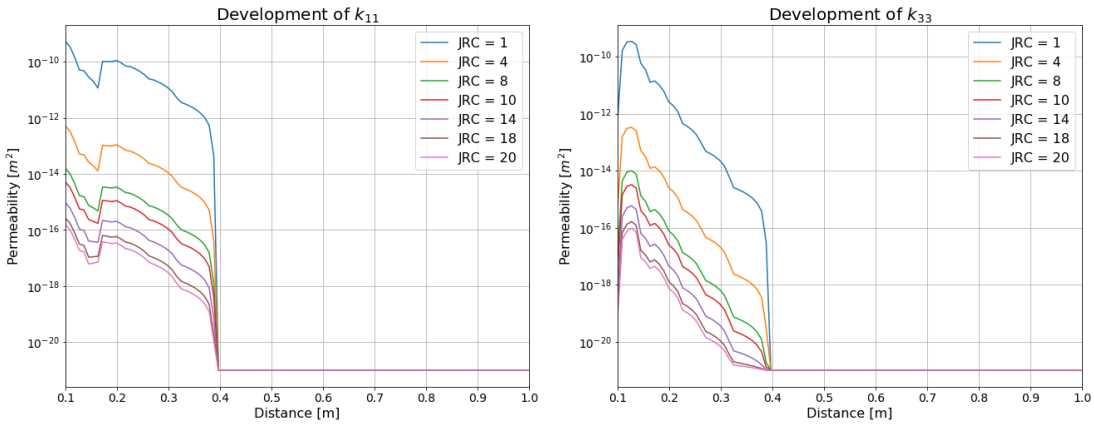

(a) k_{11} (b) k_{33}

Figure 6.20: Development of permeability along the defined axis.

The maximum values of k_{11} and k_{33} along the defined contour probe at t = 60 days have been taken into account for the analysis. Figure 6.21 also shows that the sensitivity

of the model to the input parameter becomes less pronounced when the JRC increases (when JRC is larger than 8). The permeability solution even shows no dependency on the JRC when small values are employed. This independency is valid for both k_{11} as well as k_{33}.

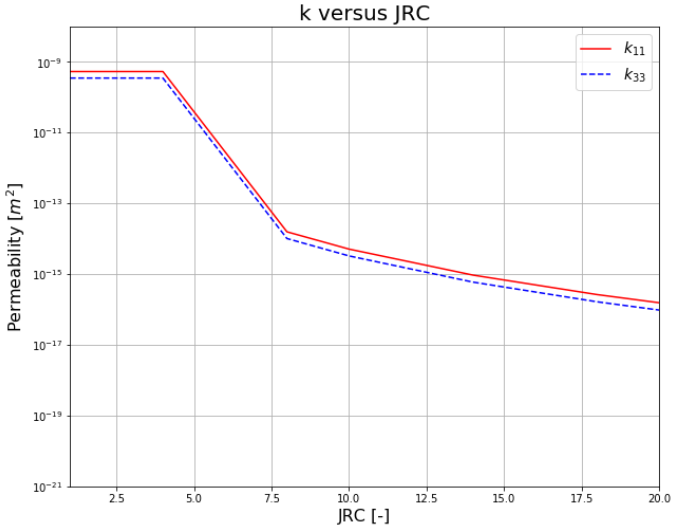

Figure 6.21: Maximum permeability along the defined axis at the end of install time for different values of JRC.

Initial permeability

In this final section of the sensitivity analysis, the dependence on the initial permeability is evaluated for both methods. Figure 6.22 shows k_{max} versus k_0 for different values of b_0, where k_{max} is the maximum permeability value which is observed along the contour probe at t = 60 days irrespective of its direction (could be k_{11} or k_{33}). This diagram displays a clear and constant (linear) relation between the two parameters in the log-log space.

Figure 6.23, on the other hand, displaying the relation between JRC, k_0 and k_{max}, shows a very different relationship. For larger initial permeabilities, the influence of the JRC reduces to zero. Moreover, no increase in permeability is even observed when k_0 is equal to $1 \cdot 10^{-12}$ m^2 and JRC is larger than 1. The opposite is true for smaller values of k_0 when k_0 does not appear to show or shows a minimal influence on the maximum final permeability k_{max}.

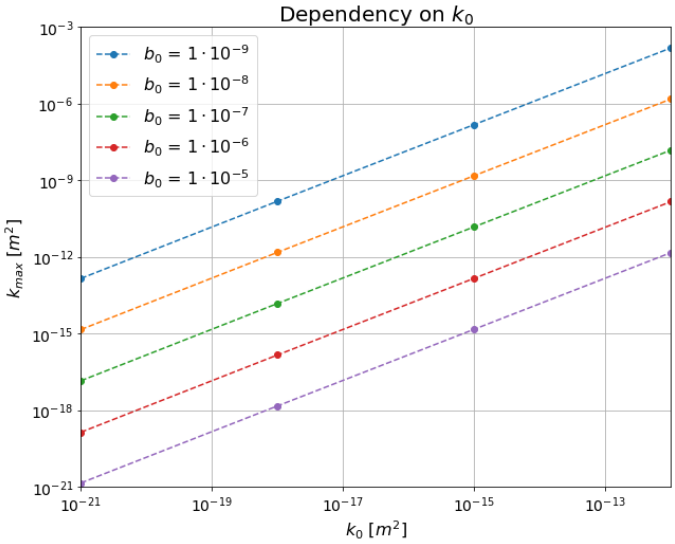

Figure 6.22: Development of maximum permeability versus the initial permeability for different values of b_0.

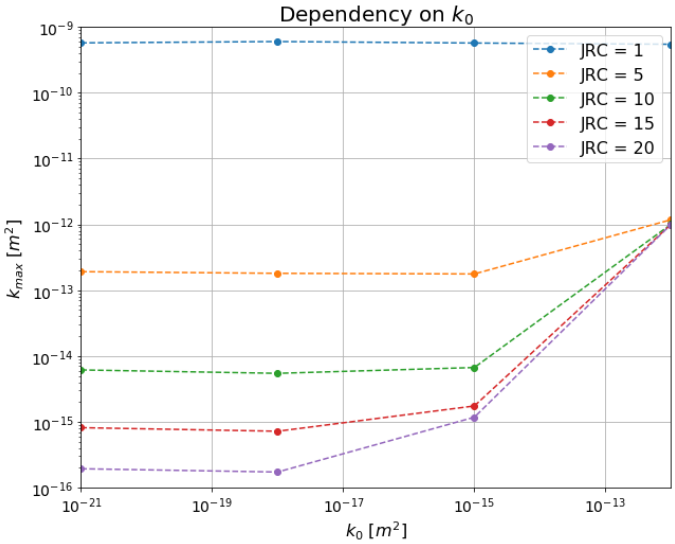

Figure 6.23: Development of maximum permeability versus the initial permeability for different values of JRC.

6.6 Conclusion

The purpose of this chapter was to first of all compare simulations generated by the fracture-dependent permeability model to a different numerical study performed by AbuAisha et al. (2016) which investigates the changes in permeability in the vicinity of a borehole due to hydraulic fracturing. And secondly, to evaluate the objectivity of these results, by performing a mesh-dependency and parameter-sensitivity analysis. The key points of the evaluations are presented and discussed in the corresponding sections.

Comparison of numerical simulations

When comparing the comparing simulations of the fracture-dependent permeability model with the results according to the numerical study by AbuAisha et al. (2016) the following should be taken into consideration:

- For the evaluation of the results, the maximum value of the permeability (both k_{11} and k_{33}) at each load step was considered. The observations were not restricted to a specific location in the model. Based on the description provided in the study by AbuAisha et al. (2016), it was assumed that they too evaluated maximum values in arbitrary directions, but this is not entirely certain.

- The description of the numerical test case by AbuAisha et al. (2016) did not include model dimensions or any mentioning of the mesh size. Because the anisotropy of the in-situ stress field influences the fracture evolution, as described in Section 6.3.2, assumptions that were made regarding the model dimensions could have affected the solution.

Nonetheless, simulations, according to both methods, show similarities to the hydraulic fracturing model (HFM) presented by AbuAisha et al. (2016) with regards to the permeability evolution. Both indicate an initially dominant evolution of k_{11} over k_{33}, which later on becomes less prominent as the pore pressure increases. The predominant extensional fracture development in the direction of the major principal confinement and a corresponding increase in k_{11} is as expected and can be attributed to the in-situ anisotropic stress field. A difference between the two methods in the permeability evolution is observed once again, where method 1 shows a clear jump at the onset of cracking and method 2 displays a more gradual increase. Moreover, absolute values in permeability increase differ, where method 2 depicts the greatest increase in permeability at the end of the analysis. It should, however, be noted that a rough estimation was made for the JRC, whereas the value of b_0 has slightly been calibrated to match the results generated by AbuAisha et al. (2016).

Finally, the comparison with the more detailed numerical model for the simulation of hydraulic fracturing identified the following shortcomings of the fracture-dependent permeability model:

- The existence of pre-existing cracks is only taken into account in a limited amount for method 1, where method 2 does not include any influence of an initially cracked state of the material. The initial aperture (b_0) is defined for method 1. However, this input parameter does not consider the direction of the cracks. If cracks are present prior to the hydraulic fracturing, this will most likely influence the development of

the permeability, especially if these cracks have a pronounced direction. There is less resistance for the pressurised fluid to reach these cracks surface and cause them to further propagate in their initial direction.

- The numerical study presented by AbuAisha et al. (2016) validates the working of its HFM as part of a more extensive research and model development for the simulation of enhanced geothermal energy reservoirs. It thus also takes into account the influence of temperature on the coupling mechanisms that occur in the thermo-poroelastic framework of a geothermal energy reservoir. The fracture-dependent permeability model as proposed in this study, on the other hand, does not include the effect of temperature on the fracture and permeability evolution, and is therefore limited in its description of a geothermal energy reservoir.

Mesh-dependency evaluation

When evaluating the magnitudes of the permeabilities at t = 60 days, both methods show a mesh dependency, resulting in smaller values of k for finer meshes, where method 1 appears to converge slightly quicker than method 2. Because of the observed trend with increasing mesh size, it is difficult to conclude the definition of an appropriate mesh density and corresponding element size based on only the mesh-dependency analysis for k_{11} and k_{33} at t = 60 days. On the other hand, the solution for the initiation of the hydraulic fracturing pressure (p_w^{HF}) converges quite quickly, showing a constant value of around 15/16 MPa for relatively rough meshes. This solution was first found with a mesh consisting of 6x12 elements. Taken the latter into account, as well as the fact that the solution (in order of magnitude) that is found for the permeability increase is comparable to results generated by AbuAisha et al. (2016), for method 1 a mesh consisting of 12x32 elements is considered to be appropriate in this case. For method 2, the employment of a finer mesh might be more appropriate, consisting of, for example 20x40 elements. In this case, the smallest element size is equal to 0.099 x 0.012 m (width x height). The computational time increases with a factor 1.6 when comparing it to the mesh consisting of 12x32 elements.

Nonetheless, the convergence of method 1 can be improved significantly when a different definition of b_0 is implemented, thereby defining it as a function of the tensile strain criterion and the crack bandwidth. In this case, a satisfactory converged solution is found for mesh consisting of 10x24 elements. However, from a physical point of view, it can be argued whether this definition of the initial aperture is appropriate, as it defines cracks in the vicinity of the borehole having a smaller initial aperture than the cracks further away from the borehole. Moreover, it is also arguable whether a non-homogeneous definition of b_0 is appropriate at all if k_0 is considered to be homogeneous in the entire domain. A similar modification for method 2 was not considered because its expression can less straightforwardly be made element size dependent.

To summarise:

- Both methods show a decreasing trend in the permeability increase with a finer mesh. Nonetheless, method 1 appears to converge slightly better than method 2. It might therefore be recommended to apply a more refined mesh for method 2 than for method 1.
- The convergence of method 1 can significantly be improved if b_0 is defined as a function of the tensile strain criterion (ε_t) and the crack bandwidth. Because

the crack bandwidth in its definition according to Govindjee et al. (1995) depends on the element size, b_0 is not homogeneous for this problem as the element size increases in the radial direction moving away from the borehole. It can be argued whether a non-homogeneous definition of b_0 is appropriate if k_0, on the other hand, is homogeneous.

Parameter-sensitivity evaluation

Based on the sensitivity analysis that has been performed, it can be concluded that both methods are quite sensitive to the newly defined additional input parameters: b_0 and JRC. Furthermore, method 2 also showed a sensitivity to k_0. The main findings are:

- Method 1 is highly sensitive to the input parameter b_0, showing a significant difference in outcome in order of magnitudes. Because b_0 can in some cases be seen as a more or less theoretical parameter or state variable that is difficult to determine, caution should be made in defining its value.
- Method 2 shows quite some sensitivity to the JRC, mostly when it ranges between 4 and 8. This sensitivity becomes less pronounced when the JRC increases. When comparing the JRC to b_0 as an input parameter, the JRC might be defined more appropriately as it is more generally accepted parameter, and therefore, more tangible concept.
- Method 2 also shows an interesting dependence on k_0, based on which it might be concluded that method 2 is only applicable to k_0 falling into a specific range. This dependence can most likely be explained by the fact that method 2 defines the overall permeability as a summation of both k_0 and k_{fr}. Because k_{fr} is independent of the initial state of the rock medium, its contribution can become increasingly more significant or insignificant depending on the initial permeability of the rock.

7. Case study: EDZ surrounding underground galleries

7.1 Introduction

This chapter covers a case study on the hydro-mechanical behaviour of Callovo-Oxfordian claystone in the surroundings of underground galleries. The case study has been presented by Armand et al. (2014) discussing its experimental findings which form the basis of a conceptual model of the excavation-induced fracture network. The experimental findings by Armand et al. (2014) will be compared with the simulations generated by the fracture-dependent permeability model as proposed by this study. The case study is also used by Pardoen (2015) as a part of their numerical study on the hydro-mechanical response of fracturing induced by excavation using shear banding. Their interpretation of the in-situ conditions and insights in the results will provide support for the representation of the case study.

The purpose of this case study is to investigate and identify to which extent the fracture-dependent model is capable of simulating hydro-mechanical behaviour due to in-situ conditions other than EGS, and examine its applicability on the simulation of excavation induced damaged zones. The focus will lie mainly on the comparison in qualitative outcome and similarities rather than quantitative results.

The first section describes the case study and the corresponding conceptual model, as presented by Armand et al. (2014). The section after that discusses the analysis and the results generated by the model proposed in this study. Conclusions are drawn in the final section.

7.2 Case description

Excavation of underground galleries causes damage in the rock material in the vicinity of the drift wall, thereby affecting the hydro-mechanical properties of the rock. The extent of the damage generally depends on the initial properties of the rock, in-situ stress field, the geometry of the opening and the time and method of the excavation (Armand et al., 2014). The 'Excavation Damaged Zone' (EDZ) can be defined as the zone, adjacent to the opening, which has been substantially damaged by the excavation resulting in hydro-mechanical modifications that induce changes in flow and transport properties.

Investigating the hydro-mechanical changes of the EDZ can, for example, be of importance for feasibility studies for deep geological repositories of radioactive waste. The French national radioactive waste management agency (ANDRA) for that reason developed the Meuse/Haute-Marne underground research laboratory (URL). The host formation of this URL is Callovo-Oxfordian claystone. A scientific study on the excavation-induced fractures in the EDZ was conducted at the main level of the URL (-490 m). Obser-

vatory methods included: structural analysis on cores, geological surveys and hydraulic conductivity measurements. The paper presented by Armand et al. (2014) discusses the main findings of the study concerning the geometry and properties of the excavation-induced fracture network. Pardoen (2015) used this study as the starting point for their research, which main purpose was to reproduce EDZ behaviour in rock material with shear banding, thereby highlighting its important hydro-mechanical aspects.

7.2.1 Callovo-Oxfordian claystone

In the Meuse/Haute-Marne Underground Research Laboratory (URL), an extensive research program has been carried out consisting of an experimental study to examine the hydro-mechanical properties and response of the Callovo-Oxfordian claystone (argillite). The claystone can be found between 420 and 550 m below the ground. The main laboratory level is located at -490 m (Armand et al., 2014).

Material properties

Numerous laboratory tests have been conducted on claystone core samples to determine its main hydro-mechanical properties. The main findings are summarised in Table 7.1. Note the low permeability of the claystone, which is due to the small mean pore diameter ($0.02\mu m$). Table 7.1 does not account for the slightly anisotropic behaviour of the claystone caused by the sedimentation process (Armand et al., 2014).

Table 7.1: Hydro-mechanical properties of the Callovo-Oxfordian claystone determined the main URL level (Armand et al., 2014).

Parameter	**Value**	**Unit**
Density ρ	2.39	g/cm^3
Porosity n	18 ± 1 %	-
Young modulus E	4000 ± 1470	MPa
Poisson ratio ν	0.29 ± 0.05	-
Uniaxial compressive strength UCS	21 ± 6.8	MPa
Hoek-Brown criteria S m	 0.43 2.5	 - -
Compressive strength σ_c	33.5	MPa
Intrinsic permeability k	$5 \cdot 10^{-20}$	m^2
Water content w	7.2 ± 1.4 %	-

Stress state

Wileveau et al. (2007) conducted a comprehensive in-situ stress field examination of the Callova-Oxfordian claystone formation and the two stiffer limestone formations, which surround the claystone. The investigation was performed at a URL at the Bure site in Northeastern France. The minor horizontal stress direction approaches lithostatic values and thus $\sigma_v \approx \sigma_h$. The K_H ratio for the claystone has an average value of 1.2 but ranges with depth. For the argillite formation, an estimation of the in-situ stress field at approximately -490 m depth, according to Wileveau et al. (2007) is:

σ_v	12.7 MPa
σ_h	11.4-12.4 MPa
σ_H	13.7-14.8 MPa

7.2.2 Induced fracture network

Armand et al. (2014) discuss the experiments and observations regarding the excavation induced fracture network in different drift directions of the URL, where the first direction is parallel to the major horizontal stress (GET/GCS) and the second one parallel to the minor horizontal stress (GED). These drifts can be observed in Figure 7.1, which displays a complete overview of the URL drift network. The following experimental methods were used during the investigation to characterise the induced fractures network:

- Structural analysis of core samples in combination with 3D analysis to determine fracture type and density;
- Geological survey of drift face and walls;
- Seismic measurements;
- Permeability measurements;
- Visualisation and measurement of fractures by resin filling.

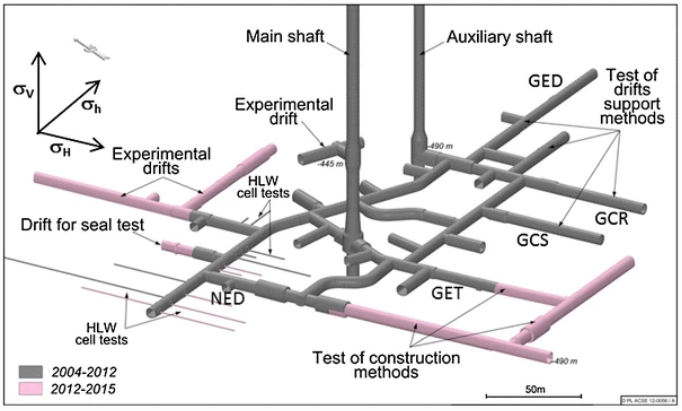

Figure 7.1: Meuse/Haute-Marne URL drifts network (Armand et al., 2014).

The structural analysis of both drifts identifies two fracture structures that were observed near the faces and walls of the excavation: a 'chevron' structure and a 'bulge' structure.

- *Chevron structure*: This structure consists of two types of fractures 'Upper chevron fractures' and 'Lower chevron fractures', which have been generated by normal shear. The 'Lower chevron fractures' are located in the lowest third of the drift's face and walls. They are curved in the horizontal plane and dip towards the excavated zone. The 'Upper chevron fractures', which are located in the upper part, have the same curve in the horizontal plane but dip towards the unexcavated zone.
- *Bulge structure*: The fractures forming the 'bulge' are located between the 'Upper and Lower chevron fractures' and are generated by extension. Their plans have a double curve, following the curve of the chevron fractures horizontally and a bulging curve in the vertical direction.

The core drillings showed that two zones of excavation-induced fracturing could be distinguished. The first zone consists of extensional and shear fractures. The orientation of the fractures in this zone is very heterogeneous. The second zone, which is located further away from the drift, consists of shear fractures only and has a more homogeneous orientation.

Based on the observations, the study defined two conceptual models of the induced fracture network around a drift parallel to the horizontal major (σ_H) and minor principal stress (σ_h). Their findings concluded that the hydraulic permeability measurements in the two drifts exhibit the same behaviour. Results, however, differ considering the location of the most significant increase in hydraulic conductivity and extent of the fracture network. The highest hydraulic conductivity increase is observed in the areas where tensile fractures are located, which is denoted as the highly disturbed zone and can be found in a range < 0.5 m from the excavation wall for the drift parallel to σ_H (GET/GCS) and up to the extent of 2 m from the ceiling and floor of the excavation for the drift parallel to σ_h (GED). In these highly disturbed areas, the hydraulic conductivity (and the permeability) can experience an increase of a factor 10^4-10^6. The transmissivity of the shear fractures in the shear fracture zone, which extends further into the rock than the extensional fracture zone, appear to have a lower impact on the hydraulic conductivity.

The conceptual model and the results from the field measurements for the drift parallel to σ_h (GED) are summarised in the next section. The results from the permeability measurements are displayed in diagrams by plotting the hydraulic conductivity versus the distance from the drift wall. It should be noted that an intrinsic permeability of $5 \cdot 10^{-20}$ m^2 corresponds to a hydraulic conductivity of approximately $5 \cdot 10^{-13}$ m/s, assuming that the gravitational constant g = 9.81 m/s^2, the water density ρ_w = 1000 kg/m^3 and the dynamic viscosity of the water $\mu = 1 \cdot 10^{-3}$ $Pa \cdot s$ (see Equation (7.1) below).

$$K = \frac{\rho g}{\mu} k \tag{7.1}$$

Finally, there are a few points that should be noted before the conceptual model and findings by Armand et al. (2014) are discussed:

- In their representation of the permeability measurements, they did not take into account the time-dependency of the hydraulic conductivity.
- The conceptual model does not always sufficiently represent the heterogeneity of the extent of fractures in the excavation damaged affecting its behaviour and properties, which can differ quite considerably along the drift axis. The conceptual model is, therefore, a representation of average values.
- In some boreholes, to a minimal limited extent, < 1 x the diameter of the drift (D), rocks cuttings induced by the drift excavation or boring were observed. However, because the fractures were difficult to identify, and their orientation could not be determined, they have not been included in the global induced fracture model.

Results GED - parallel to σ_h

The model shown in Figure 7.2 shows the visualisation of the concept of the excavation induced fracture network along a drift parallel to the minor horizontal stress (σ_h) (Armand et al., 2014). In this case, most of the fractures are expected to occur at the floor and

ceiling of the excavated gallery, where the extensional fracture zone extends to 1.24/1.27 m and the shear fracture zone to 2.75/3.70 m. Similar observations are summarised in Table 7.2, where the extent of the fractures zones is displayed as a function of the drift diameter (D). From the table, it can once again be concluded that the shear fracture zone is greater than the extensional fracture zone, and that fractures predominantly occur at the gallery floor/ceiling instead of the wall.

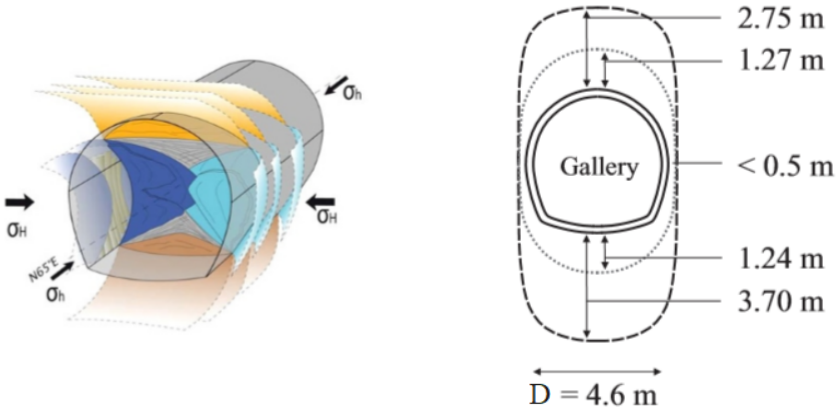

Figure 7.2: Conceptual model of the induced fracture network with a drift (GED) parallel to the minor horizontal stress. The dotted line indicates the extent of tensile fractures and the dashed line the shear fractures (Armand et al., 2014; Pardoen, 2015).

Table 7.2: Extent of fracture zones for a drift parallel to σ_h (Armand et al., 2014). The '-' indicates no extent further than the extensional fracture network.

	Extensional fractures			**Shear fractures**		
	Min	**Average**	**Max**	**Min**	**Average**	**Max**
Ceiling	0.2 x D	0.3 x D	0.4 xD	0.5 x D	0.6 x D	0.8 x D
Wall	0.1 x D	0.1 x D	0.2 x D	-	-	-
Floor	0.2 x D	0.4 x D	0.5 x D	0.8 x D	0.8 x D	1.1 x D

Figure 7.3 shows the results of the permeability measurements, where the hydraulic conductivity is plotted versus the distance from the gallery wall. The left diagram shows the results measured in horizontal boreholes alongside the wall and the diagram on the right displays the results for vertical boreholes located at the floor and ceiling of the gallery. The arrows above the diagrams indicate the extent of the fracture zones. From these diagrams, it can be deduced that the highest increase in hydraulic conductivity is observed in the extensional fracture zone reaching values of $1 \cdot 10^{-9}$ m/s in the horizontal boreholes located at the wall and almost $1 \cdot 10^{-7}$ m/s in the vertical borehole near the floor of the gallery.

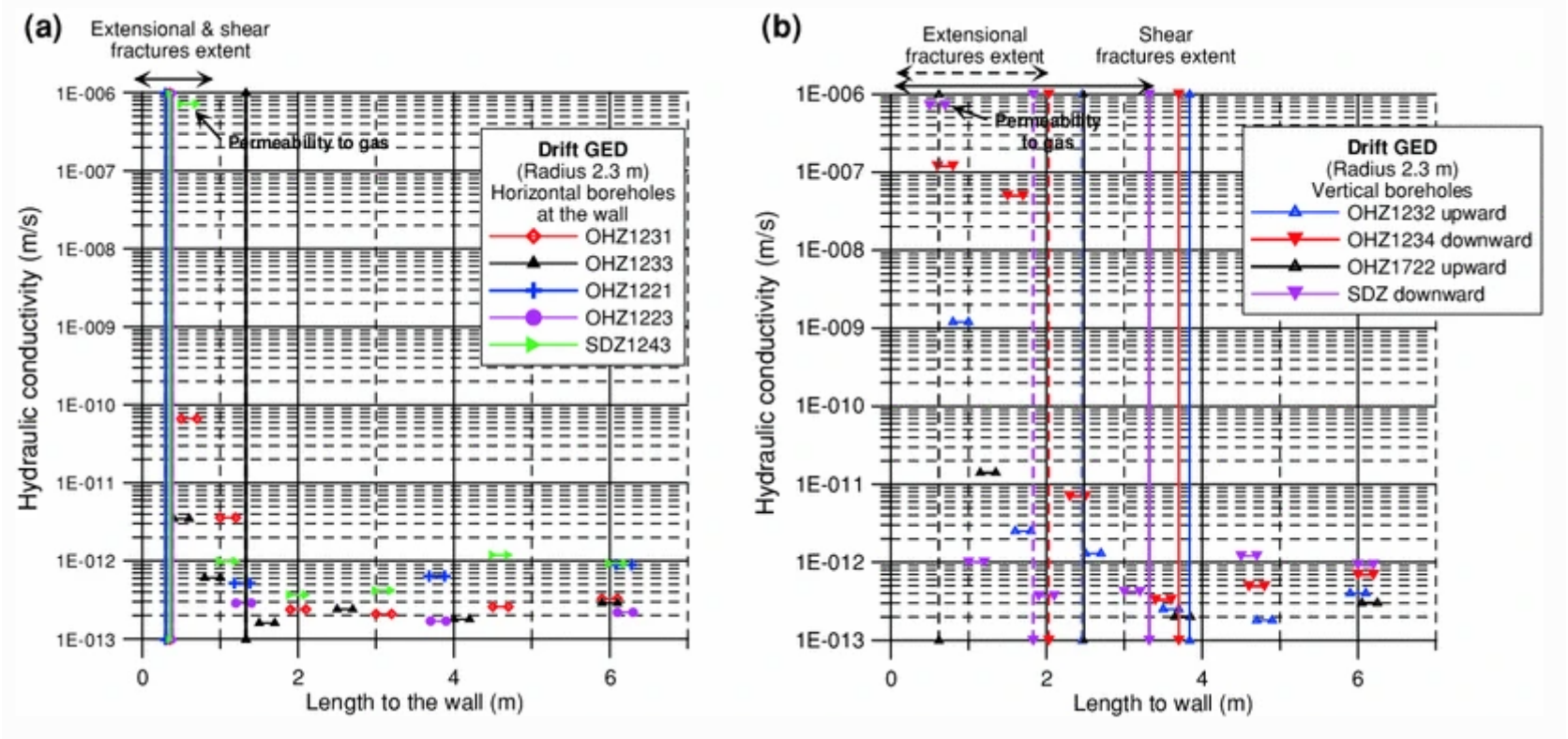

Figure 7.3: Hydraulic conductivity measurements in drift GED (parallel to σ_h) in horizontal boreholes at the wall (a) and vertical boreholes at the floor and ceiling (b) (Armand et al., 2014).

7.3 Analysis

A fracture-dependent permeability analysis is performed considering the situation of the drift parallel to the minor horizontal stress σ_h (GED).

The claystone formation and the excavated drift is represented by a simplified two-dimensional boundary value problem consisting of plane-strain elements. The model is supported in the normal directions along its boundaries. A pore pressure potential support is also applied at the domain boundaries. The dimensions are 40 x 40 m (see Figure 7.4). The dimensions of the domain have been chosen such that its boundary conditions would not affect the excavation damaged zone, considering this zone extended to a maximum of 1 x D (diameter) of the excavation according to the study performed by Armand et al. (2014). The tunnel is represented by circular excavation with a diameter of 4.6 m. This dimension was chosen based on the conceptual model, see Figure 7.2 in the previous section.

The mesh density has been generated such that the desired element size near the excavation is equal to 0.1 x 0.1 m, and elements near the boundary are equal to 1 x 1 m. The localised mesh refinement accounts for the fact that fractures are only expected to occur in the vicinity of the excavation, and at this location elements of 0.1 x 0.1 m are sufficiently small to allow for an appropriate evaluation of the effects on the permeability evolution near the excavation, while also conserving a reasonable computational time.

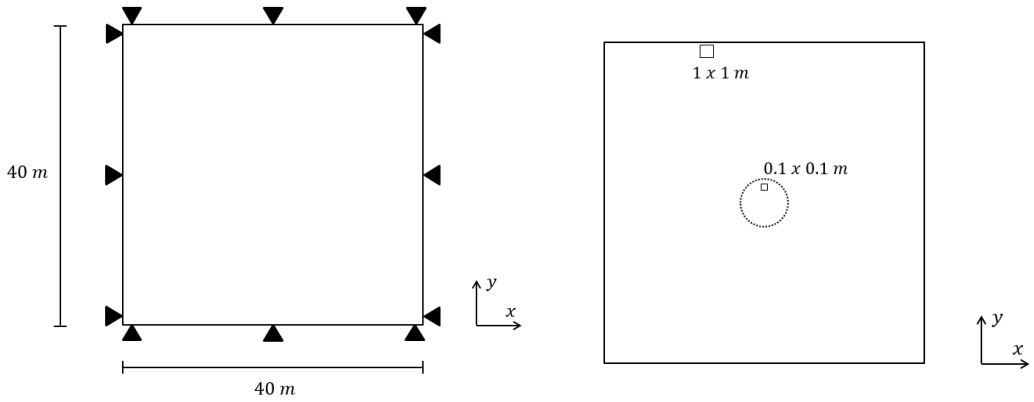

Figure 7.4: The dimensions, boundary conditions and desired element sizes of the mesh of the boundary value problem.

The process of excavation is represented in simplified form by a non-linear phased analysis consisting of two phases. During the first phase (initialisation), when no excavation is present yet, the in-situ stresses (σ_v, σ_h and σ_H) and the pore pressure in the rock are initialised by applying an element pre-stress and a pore pressure potential condition along the boundary of the domain, see Figure 7.5 for illustration. With regards to the in-situ stress state, the following values have been implemented: σ_v = - 12.7 MPa. σ_h = - 11.4 MPa and σ_H = - 14.8 MPa (confining stresses). These values were determined, taking into account the average ranges observed by Wileveau et al. (2007). These values result in a K_H ratio of 1.3, which was also adopted in the numerical simulation by Pardoen (2015).

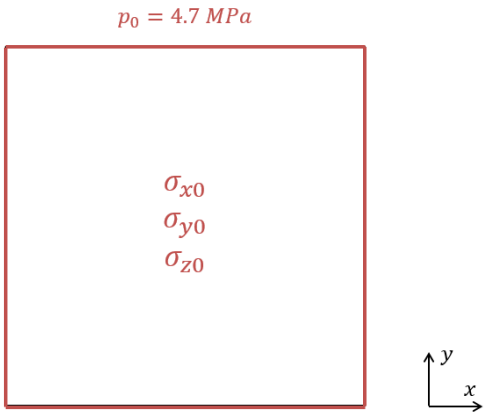

Figure 7.5: Phase 1: Homogeneous stress and pore pressure field.

Moving on to phase 2, the tunnel is excavated and the pore pressure potential is supported along the 'gallery wall', thereby allowing water drainage from the rock into the excavation. The stress in the domain is initialised by making use of the load as defined in phase 1 (see Figure 7.6a) . Next, a time-dependent analysis is performed. At the beginning of second phase, the pore pressure potential at the gallery is reduced to zero by prescribing a pore pressure potential deformation of -4.7 MPa (see Figure 7.6b). The total duration of the time-dependent analysis is two days and 13 hours. Time steps are divided into thirteen time increments, which are smaller at the beginning and become larger towards the end of the analysis.

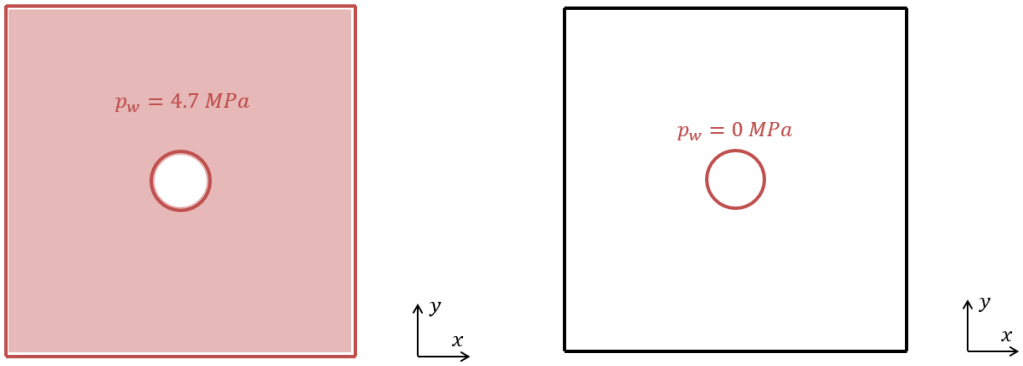

(a) Start

(b) Time

Figure 7.6: Phase 2: Pore pressures during start and time steps.

The claystone material will be described by the fracture-dependent permeability model in combination with the Multi-Directional Fixed crack model. The choice for this particular fracture model and not the Total Strain crack model resides on the fact that the Total Strain crack model is less suited in dealing with initial stresses, as it describes stress as a function of strain. In contrast to the fracture-dependent permeability model, the Multi-Directional Fixed crack model, as its name suggests, assumes the direction of a fracture to remain fixed upon the moment of crack initiation. To determine crack initiation, the model applies the following two criteria which must be satisfied simultaneously:

- The principal tensile stress exceeds the tensile strength (or maximum stress condition) of the material;
- The angle between an already existing crack and the new potential crack exceeds a threshold angle value (α_{TD}).

With regards to the tension softening of the rock material, linear tension softening, based on the ultimate strain (ε_u^{cr}), is assumed. Figure 7.7 shows this tension softening curve. The ultimate strain is the parameter that controls the extent of ductile softening behaviour of the material, and it is assumed to remain constant throughout the analysis. The minimum value of the ultimate crack strain ($\varepsilon_{u,min}^{cr}$ is given by Equation (7.2)). Implementation of this value would correspond with brittle failure. Another input parameter that is required for the Multi-Directional Fixed crack model, is the shear reduction factor β. This parameter governs the shear stiffness reduction of the material due to cracking.

$$\varepsilon_{u,min}^{cr} = \frac{f_t}{E} \tag{7.2}$$

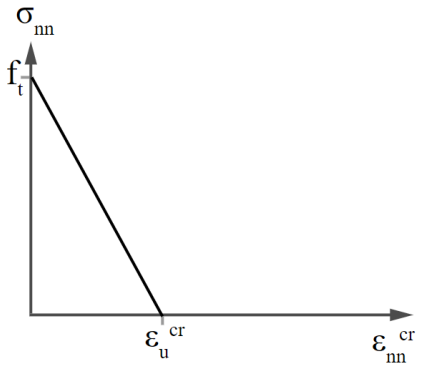

Figure 7.7: Linear tension softening curve based on the ultimate strain (DIANA FEA bv, 2019).

The material properties for the applied Multi-Directional Fixed crack model in combination with the fracture-dependent permeability model can be found in Table 7.3. Because shear fractures are also expected to occur in the surroundings of the excavation, according to the conceptual fracture model by Armand et al. (2014), Mohr-Coulomb yield criterion has also been included to account for shear failure. The material properties were determined based on the parameters used in the studies by Gens et al. (2007), Armand et al. (2014) and Pardoen (2015). Except for the crack model specific parameters, for which either a standard value is adhered to (β) or values are estimated (ε_u^{cr} and f_t).

An estimation of the tensile strength of the claystone is made based on the Hoek and Brown parameters provided in the study by Armand et al. (2014). According to Hoek et al. (2002), the tensile strength can be calculated as

$$\sigma_t = -s\frac{\sigma_{ci}}{m_b} \tag{7.3}$$

where s and m_b are material constants and σ_{ci} is the uniaxial compressive strength of the intact rock material (Hoek et al., 2002). In this case s = 0.43, m_b = 2.5 and σ_{ci} = 21 MPa. Thus the tensile strength is approximately 6 MPa.

Table 7.3: Material properties of the Callovo-Oxfordian claystone described by the fracture-dependent permeability model in combination with the Multi-Directional Fixed crack material model and a Mohr-Coulomb yield criterion.

	Parameter	**Value**	**Unit**
General	Young's modulus E	4	GPa
	Poison's ratio ν	0.29	-
	Density ρ	2.3	kg/m^3
	Porosity n	0.18	-
Multi-Directional Fixed crack model	Tensile strength f_t	6	MPa
	Ultimate strain ε_u^{cr}	$1.5 \cdot 10^{-3}$	-
	Shear retention factor β	0.05	-
Mohr-Coulomb plasticity	Cohesion c	25	MPa
	Friction angle ϕ	23	°
	Dilatancy angle ψ	0.3	°
Fracture-dependent permeability model	Initial permeability k_0	$5 \cdot 10^{-20}$	m^2
	Dynamic viscosity μ	$1 \cdot 10^{-3}$	$Pa \cdot s$
	Initial aperture b_0	$f(\varepsilon_t, h_{cr})$	m

7.4 Results

The results section has been subdivided into two subsections: evaluation of tensile crack development according to the Multi-Directional Fixed crack model, and evaluation of the permeability evolution according to the fracture-dependent permeability model. The findings will be compared and discussed.

In some cases, results are evaluated along two specific directions. The first contour probe is located at the ceiling of the excavation and extends 5 m in the vertical direction and the second contour probe is located at the wall of the excavation and extends 5 m in the x-direction (see Figure 7.8). These locations and directions have been chosen such that results can be best compared by the vertical and horizontal boreholes which were located alongside the drift. An extent of 5 m is adopted because the conceptual model proposed by Armand et al. (2014) defined the EDZ up to a maximum of approximately 5 m.

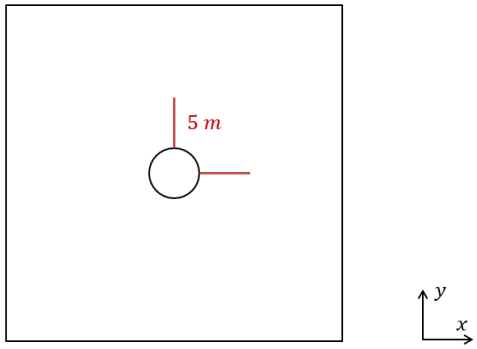

Figure 7.8: Location of the contour probes at the ceiling (y-direction) and the wall (x-direction) of the excavation.

Tensile crack development

The initial in-situ conditions consist of compressive stresses only. However, as a result of the excavation, a ring of tensile stress is formed around the perimeter of the drift. At t = 0 (phase 2), see Figure 7.9a, the effective principal stress is at a maximum value of 4.7 MPa. Due to the drainage of water into the excavation, and the corresponding decrease in pore pressure over time, the effective principal stress will decrease to 0 MPa at (see Figure 7.9b).

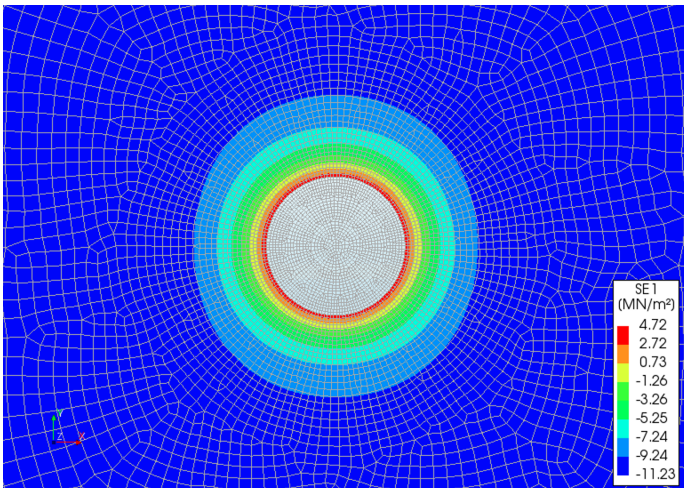

(a) Contour plot at t = 0

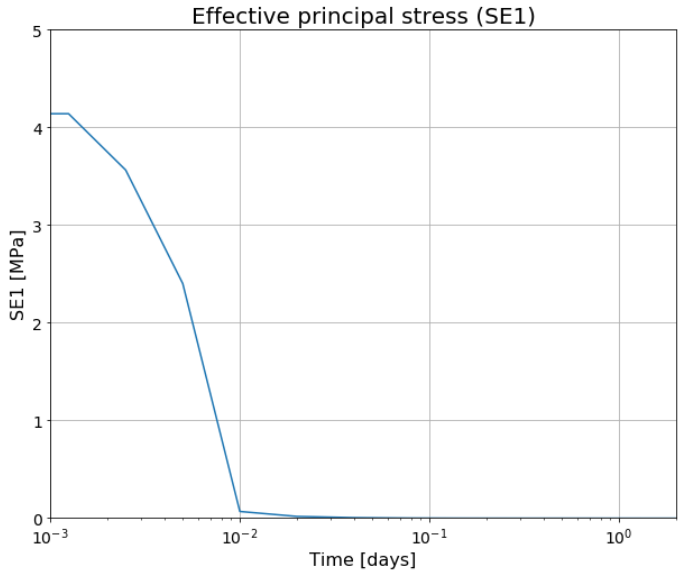

(b) For the duration of the entire drained analysis

Figure 7.9: Development of effective principal stress over time (phase 2).

Because the tensile strength of the material was estimated at 6 MPa, this tensile stress will not lead to the initiation of tensile cracks according to the Multi-Directional Fixed crack model. For that reason, a lower value of the tensile strength is adopted. The tensile strength is now estimated at 4 MPa. In that case, tensile cracks do develop according to the crack model. Figure 7.10a shows the maximum normal tensile crack strains at t = 0 (phase 2). Due to the decrease in effective stresses, these normal tensile crack strains (ε_n^{cr}) will drop to zero (see Figure 7.10b). The extent of the tensile cracks is very limited and only present in the closest vicinity of the perimeter of the excavation (approximately 0.3 m).

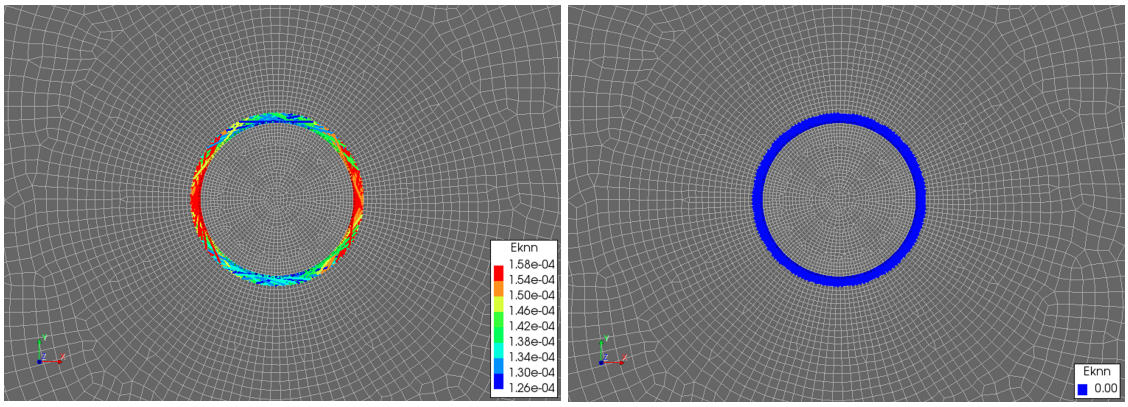

(a) t = 0 (b) t = 14 min (time step 5)

Figure 7.10: Normal tensile crack strains (ε_n^{cr}) according to the Multi-Directional Fixed crack model.

Figure 7.11a and 7.11b, show the development of the effective principal stress and principal strain at the ceiling of the excavation for two different values of the tensile strength (f_t) and ultimate crack strain (ε_u^{cr}). It can be observed that a lower f_t results in a slightly lower principal effective stress and higher principal strain. A different value for the ultimate crack strain was adopted to evaluate the effects on the stress and strain development. If $f_t = 4$ MPa, then $\varepsilon_{u,min}^{cr} = f_t/E = 1 \cdot 10^{-3}$. The value of $\varepsilon_u^{cr} = 1.5 \cdot 10^{-3}$ is close to the minimum value and therefore the behaviour will resemble more brittle cracking, resulting in greater strain development than for a higher value of ε_u^{cr} (see Figure 7.11b).

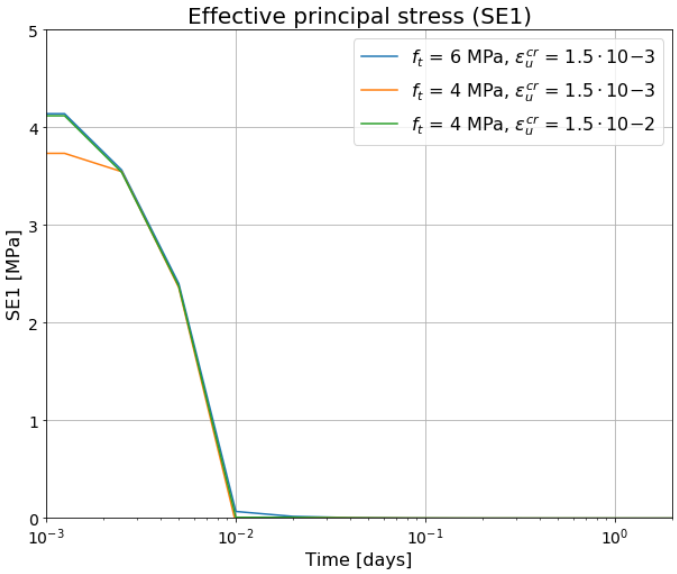

(a) SE1

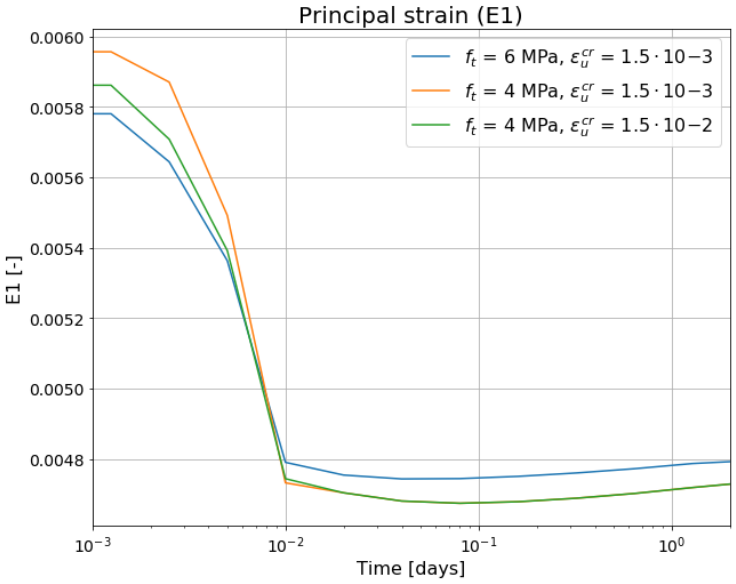

(b) E1

Figure 7.11: Development of effective principal stress (SE1) and principal strain (E1) for different values of the tensile strength (f_t) and ultimate strain (ε_u^{cr}) of the material.

Permeability evolution

The simulation has been performed according to method 1 for $b_0 = \varepsilon_t \cdot h_{cr} \cdot 0.01$. The definition of b_0 as a function rather than a constant parameter was employed to reduce the mesh-dependency. The factor of 0.01 was adopted for calibration of the results.

The results according to method 2 are not discussed in this section. The reason for this is that simulations according to method 2 results in extremely high permeabilities (or hydraulic conductivities). This phenomenon might again be attributed to the very low initial permeability of the claystone, thereby resulting in a relatively high increase in permeability due to the presence of fractures.

Figure 7.12a shows the hydraulic conductivity development along a vertical contour

probe from the ceiling of the excavation, and Figure 7.12b for a horizontal probe from the wall. The diagrams show both the hydraulic conductivity at the start (t = 0) and at the end of the analysis (t = 2 days and 13 hours). The values for the hydraulic conductivity (K) along the contour probe have been determined based on the computed modified permeability, and assuming that g = 9.81 m/s^2 and ρ_w = 1000 kg/m^3.

When evaluating these diagrams, a maximum hydraulic conductivity of approximately $1 \cdot 10^{-7}$ m/s can be observed at the edge of the excavation. This corresponds with the measurements by Armand et al. (2014). However, the extent of the permeability increase (maximum distance at which an increase in permeability is observed) is much greater than expected. For the final values, an extent of 2.5 m increase in hydraulic conductivity can be found along the vertical contour probe at the ceiling, and an even greater reach, a little over 3 m, for the horizontal contour probe at the wall. This extent is not only greater than predicted in the conceptual fracture model by Armand et al. (2014) but also than the extent of cracking according to the Multi-Directional Fixed crack model, which only showed a maximum extent of approximately 0.3 m. This discrepancy between the Multi-Directional Fixed crack model and the fracture-dependent permeability model can most likely be attributed to the difference in crack criterion, which is defined as a stress criterion for the Multi-Directional Fixed crack model and a strain criterion for the fracture-dependent permeability model. In this case, the strain criterion for the fracture-dependent permeability model as a function of the tensile strength and the Young's modulus does not seem to be appropriate, and appears to be an underestimation of the tensile strength of the material. Furthermore, it should also be noted that under these circumstance (being decreasing tensile stresses and strains over time) the rotating crack approach of the fracture-dependent permeability model is also not suitable, since it could lead to the complete disappearance of cracks over time.

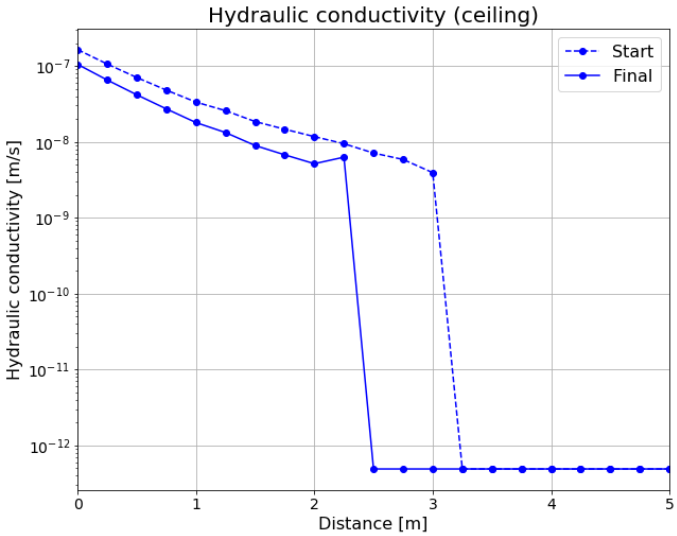

(a) Ceiling (y-direction)

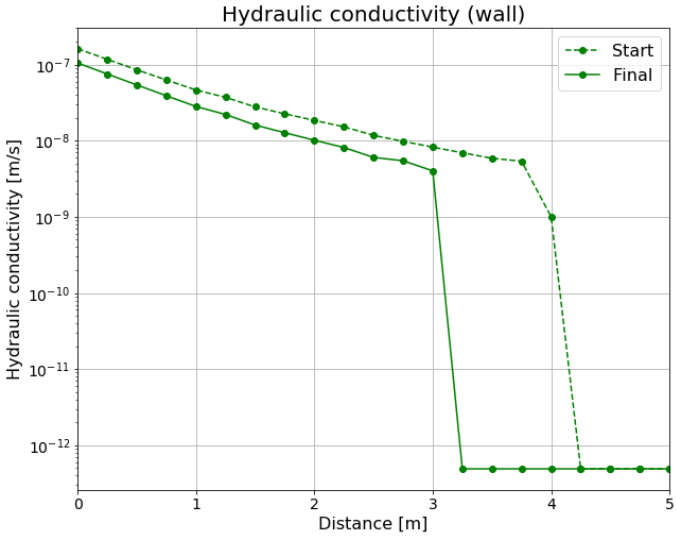

(b) Wall (x-direction)

Figure 7.12: Development of hydraulic conductivity along a vertical (ceiling) and horizontal (wall) contour probe at the beginning and end of the analysis (phase 2).

Figure 7.13 shows the contour plot of the modified permeability in the borehole vicinity, where (a) displays the maximum values of k' irrespective of its direction, moreover, (b) and (c) show the values of k'_{xx} and k'_{yy}, respectively. From these figures, it can be observed that the increase in permeability k'_{xx} is more significant at the excavation ceiling/floor than alongside the wall. The opposite is true for k'_{yy}. This specific evolution of k' in a particular direction could correspond with 'bulging', or so-called 'onion-like skin' fractures. This bulging structure has been illustrated in Figure 7.14.

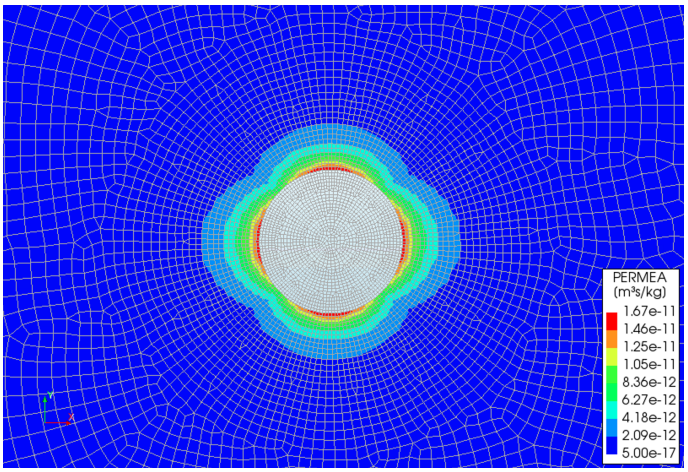

(a) k'

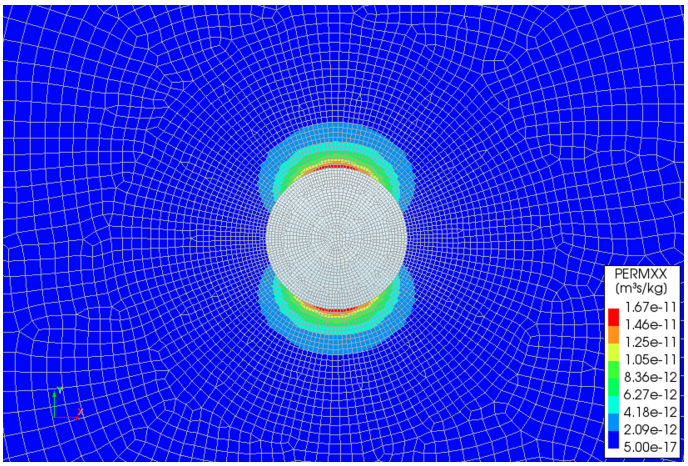

(b) k'_{xx}

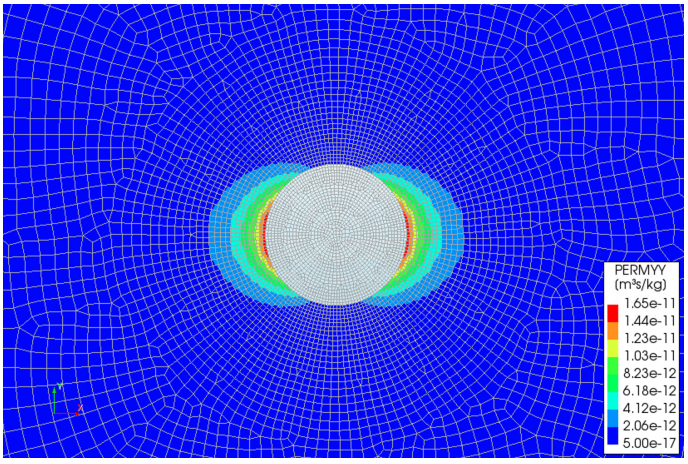

(c) k'_{yy}

Figure 7.13: Contour plot of the modified permeability at phase 2 for drift parallel to σ_h (GED).

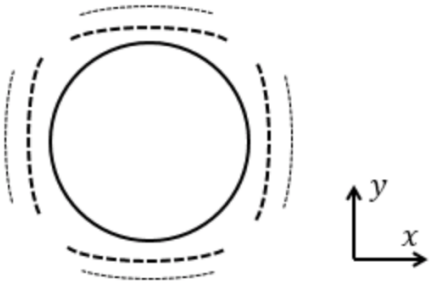

Figure 7.14: Visualisation of extensional fractures in the highly disturbed zone representing a bulging structure.

The pore pressure distribution in the vicinity of the excavation over time is shown in Figure 7.15. It can be seen that due to the drainage of water into the excavation, the pore pressures in a radius of approximately 5 m, drops completely to zero. Due to the bulging structure of the fractures surrounding the excavation, the initial zero pore pressure front shows a square-like shape. As time progresses, this shape disappears and the pore pressures become more evenly distributed.

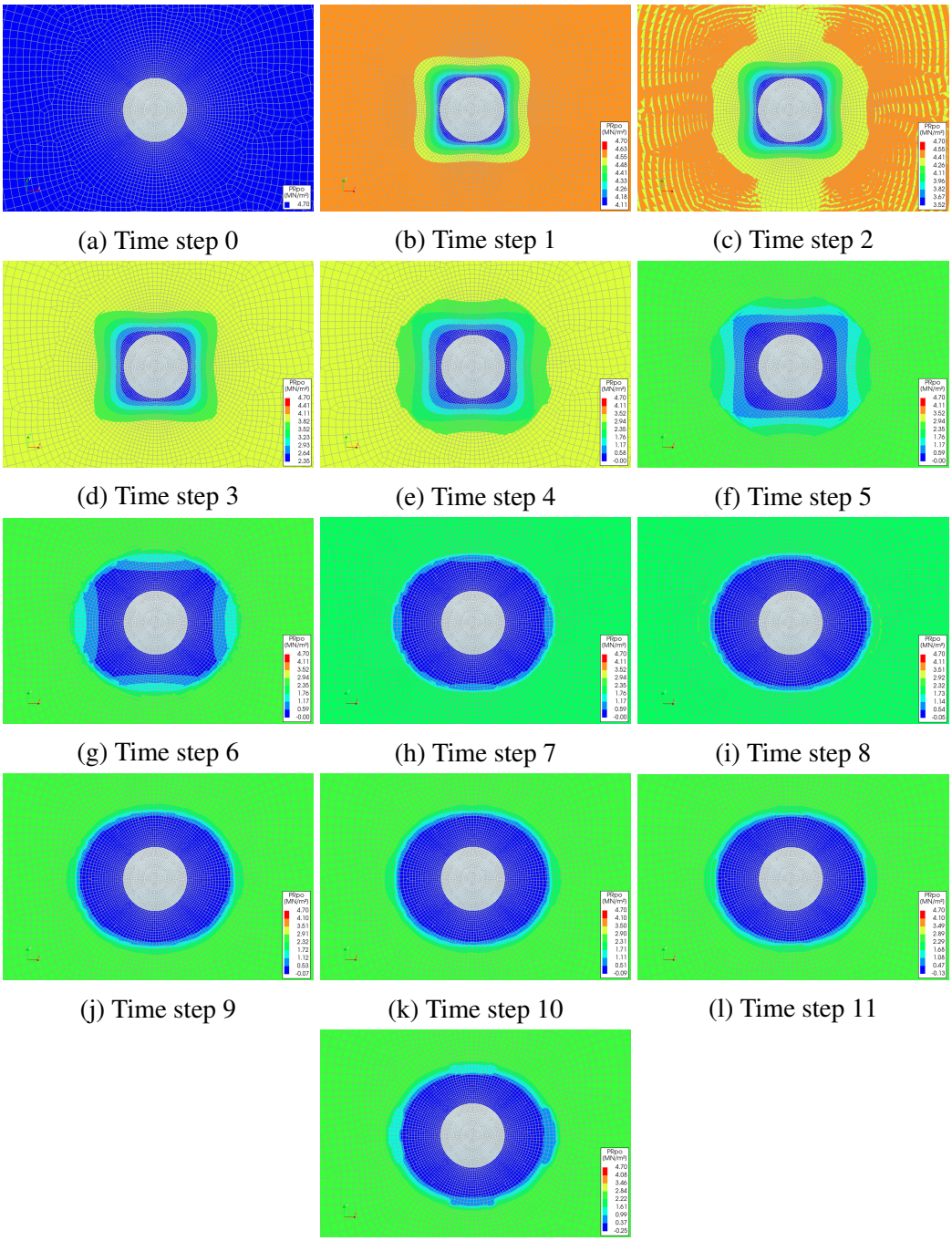

(a) Time step 0 (b) Time step 1 (c) Time step 2

(d) Time step 3 (e) Time step 4 (f) Time step 5

(g) Time step 6 (h) Time step 7 (i) Time step 8

(j) Time step 9 (k) Time step 10 (l) Time step 11

(m) Time step 12

Figure 7.15: Pore pressure development in the vicinity of the excavation.

Modified crack strain criterion

The previous analysis demonstrated that the current crack strain criterion is not appropriate in this case; it results in an underestimation of the tensile strength of the rock material because it does not take into account the initial stress state in the domain. For that reason, the model's crack strain criterion has been modified, see Equation (7.4). For σ_0 the lowest value of the three confining stresses (σ_{x0}, σ_{y0} and σ_{z0}) has been adopted, and thus σ_0 = σ_{z0} = -11.4 MPa. Due to this modification, the strain threshold for cracking is higher than before, resulting in a more limited increase in hydraulic conductivity. This can be seen

in Figures 7.16a and 7.16b, showing the development of the hydraulic conductivity along the contour probes at the ceiling and wall. The development has been evaluated over the first 2 m of the contour probes (instead of over the full length of 5 m). The first thing that can be observed, is that the hydraulic conductivity at the exact edge of the excavation (distance = 0 m) is a factor 10 smaller than the simulations of the previous analysis, adhering to the original definition of the strain crack criterion. Secondly, an increase in hydraulic conductivity is only observed over a distance < 0.75 m from the excavation, where for the previous analysis, this could extend up to a maximum of 4 m. This more limited extent is in better agreement with the results from the Multi-Directional Fixed crack model, which only indicated cracking in the closest vicinity of the excavation.

$$\varepsilon_t = \frac{f_t - \sigma_0}{E} \tag{7.4}$$

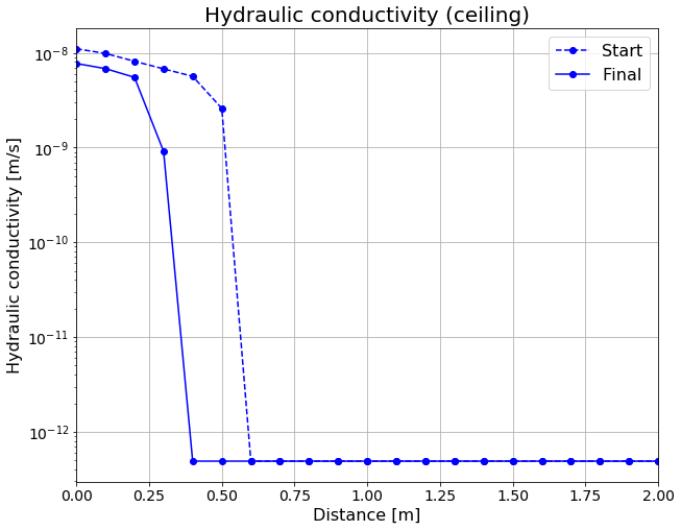

(a) Ceiling (y-direction)

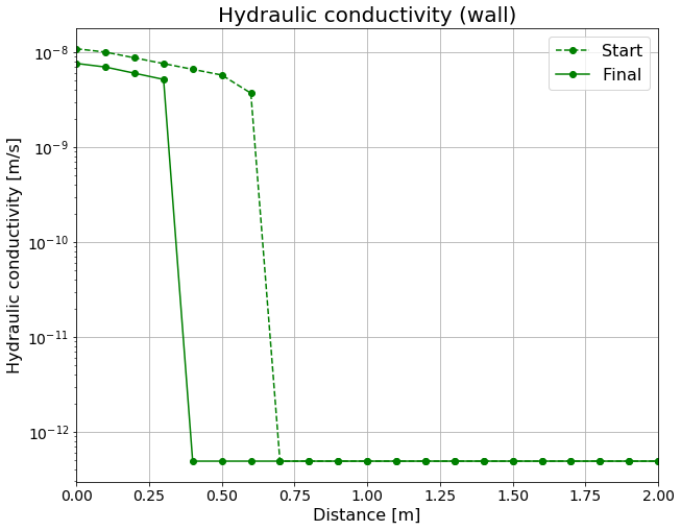

(b) Wall (x-direction)

Figure 7.16: Development of hydraulic conductivity along a vertical (ceiling) and horizontal (wall) contour probe at the beginning and end of the analysis (phase 2) for the modified crack strain criterion.

Figure 7.17a and 7.17b show a contour plot of the modified permeability development in the vicinity of the borehole at the beginning and end of the second phase. It can be seen that over time the absolute value of the permeability decreases as well as the spacial extent of permeability development. This can be explained by the fact that tensile stresses and thus tensile strains decrease over time, and by adhering to a rotating crack approach, it will consequently affect the permeability evolution.

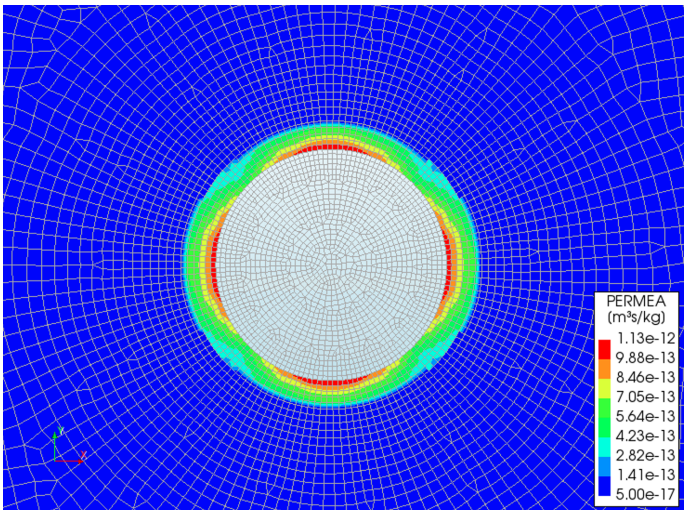

(a) k' (start)

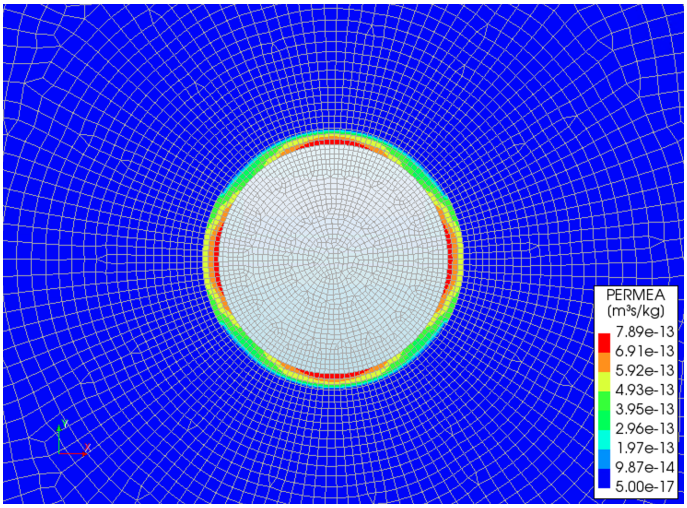

(b) k' (final).

Figure 7.17: Contour plot of the modified permeability at phase 2 according to the updated crack strain criterion.

7.5 Conclusion

The simulations according to the fracture-dependent permeability model correctly show an increase in hydraulic conductivity of approximately $1 \cdot 10^{-10}\ m/s$ in the closest vicinity of the excavation, and the directional development of the permeability displayed a bulging-like structure. Apart from that, there are quite a few dissimilarities between the simulations according to the fracture-dependent permeability model and the conceptual fracture model proposed by Armand et al. (2014), as well as the fracture development

denoted by the Multi-Directional Fixed crack model. Based on that, it can be concluded that given the current state of the fracture-dependent permeability model, it is not very suited for representing the hydro-mechanical behaviour in the excavation damaged zone of the Callovo-Oxfordian claystone. This conclusion is supported by the following points, highlighting the limitations and room for improvement of the model:

- The crack criterion formulated as a strain criterion (based on the tensile strength of the material), might not be appropriate in this case. The fracture-dependent permeability model accounts for mode I cracking; extensional cracks. Extensional cracks can form as a result of tensile stresses exceeding the tensile strength of the material, i.e. tension cracks are formed. However, they can also propagate due to increased pore pressure, which consequently results in tensile strains, but not necessarily tensile stress exceeding the tensile strength of the material. In this particular case study on the EDZ, we are looking at purely tension cracks. And therefore, this strain criterion might not be suitable. The greater spacial extent of the permeability evolution according to the fracture-dependent permeability model when comparing it to the results generated by the Multi-Directional Fixed crack model, can be attributed to this difference in crack criterion. A second fracture-dependent permeability analysis showed that this could be improved if the initial stress state of the domain is included in the definition of the strain crack criterion.

- In this situation, a decrease in tensile stresses was observed over time. If the fracture-dependent permeability model had adhered to a stress crack criterion or a higher threshold for the strain crack criterion, cracks would have 'disappeared' over time due to the rotating crack approach that is employed by the model. It is possible that the aperture of tension cracks could somewhat decrease over time, due to the decrease in tensile stress. However, it is not very realistic if they would have completely disappeared. A rotating crack approach is therefore not very suitable in this case.

- The model is not able to capture the effects of shear fractures on the hydro-mechanical behaviour of the rock, since the model only incorporates cracking and aperture development according to the crack mode I (extensional cracks). The absence of shear fractures in the definition of the permeability increase could have also affected the results for the extensional fracture zone, which also includes shear fractures. In the case of simulating excavation damaged zones, shear fractures play a significant role, and therefore this model might not be most appropriate.

- The description of cracks in the fracture-dependent permeability model could arguably be improved by incorporating a more refined interpretation of the initial fracture state and fracture development. Initial heterogeneity as a result of bedding planes will most likely have affected the hydro-mechanical behaviour of the rock and thus the field measurements. Defining the rock material as an initially fractured medium with cracks of a particular dimension and direction would probably be more appropriate.

8. Discussion

This chapter discusses the most relevant concepts and methods that were adhered to in the development of the fracture-dependent permeability model, and thereby attempts to provide a critical review on the interpretation of the findings.

Cubic law

The cubic law adheres to the simplest representation of a fracture in the form of two smooth, parallel plates, and assumes a laminar fluid flow, which is a cubic function of the fracture aperture. The fracture-dependent permeability model consequently defined the modified permeability as a quadratic function of the aperture. It can be questioned to which extent this quadratic relation is valid, and if the expression is also appropriate for larger scale fractures. It should be further investigated if the model would benefit from a maximum aperture value. Moreover, literature already indicated that a direct implementation of the mechanical aperture in the expression for the fluid flow in terms of the cubic law is not very appropriate since the parallel plate model is not a very realistic representation of a rough, undulating fracture, possibly containing infill. It is therefore suggested to account for this deviation by either applying a reduction factor or by incorporating an empirical formula to determine the equivalent hydraulic aperture of the fracture. In this study, the expression for the hydraulic aperture as a function of the joint roughness coefficient by Barton and Choubey (1977) was adhered to. However, it could be evaluated if this is the most suited expression for determining the equivalent hydraulic aperture, or if another empirical formula would me more appropriate in different circumstances or considering different types of rock.

Rotating crack concept

From an engineering point of view the rotating crack concept is very attractive, because it ensures coincidence between the principal directions and the crack axes. However, from a physical point of view, it is not possible to provide a logical explanation as to why cracks are able to rotate freely upon different loading conditions. Nonetheless, for monotonic loading conditions, which is generally the case for EGS, the difference between a rotating and a fixed crack concept is not so relevant. It does become relevant if the rock material is subjected to cyclic loading, due to for example seismic waves, resulting in the fracture initiation and propagation. In such a situation, the current adoption of the rotating crack concept in the fracture-dependent permeability model would not be appropriate. Furthermore, the final case study on the hydro-mechanical behaviour in excavation damaged zones also provided an exemplary situation in which the rotating crack concept is less suited than the fixed crack concept due to the decreasing tensile stresses over time, which would lead to the complete 'disappearance' of fractures that were initially present.

Besides that, the model is very limited in describing the initially cracked state of rock material. It could be argued that the model should include a more detailed description of the initial conditions of the cracks, being its size and direction, as this will ultimately affect the development of the fracture growth. Method 1 defines the initial aperture, yet this parameter functions more as a threshold value for the onset or propagation of cracking than that it is a state parameter. Moreover, the expression of b_0 does not include any information regarding the initial direction of the fractures. Method 2 does not take into account any expression for the fact that cracks might already be present on beforehand. Heterogeneities in the rock material that are already present, due to for example a drilling method or bedding planes, can very much affect the propagation of fracture development. A more elaborate description of the initial state of the material should therefore be reflected in the model. If such a description is implemented, the adoption of the rotating crack model will have to be reconsidered, since it is not very logical to on the one hand predetermine the direction of cracks while at the same time allowing them to rotate during the analysis.

Permeability as a function of the crack normal strain

A strain-dependent rather than a stress-dependent permeability has been employed, because it is arguably better suited to deal with non-linear/post-peak behaviour. This is also reflected in crack criterion, which has also been formulated as a strain criterion instead of a stress criterion. Adopting a strain dependency is more convenient if the rotating crack concept is adopted, since upon fracturing tension softening is expected to occur leading to a decrease in effective tensile stresses, which would consequently result in the 'disappearance' of cracks. However, the determination of a tensile strain criterion is less straightforward than the implementation of a tensile stress parameter, because in most literature and experimental studies the strength of a material is expressed in terms of maximum stresses. For that reason, the fracture-dependent permeability model defined the tensile strain criterion as a function of the tensile strength and Young's modulus of the rock material. Nevertheless, in the final case study, this definition did not appear to be appropriate because it did not take into account the initial stresses in the rock and therefore resulted in an underestimation of the crack criterion of the material. A reconsideration of the strain crack criterion could therefore be argued.

Moreover, the fracture-dependent permeability model only takes into account the development of mode I (extensional) fractures. For the incorporation of crack modes II and III, the model should reconsider the definition of the aperture as a function of the crack normal strain only, as it can also be affected by shear dilation. Nevertheless, the case study also showed that the extensional fractures affected the permeability development the most, showing the highest increase in the zones containing these fractures. On top of that, it should also be further examined to which degree a geothermal hydraulic fracturing problem would benefit from the inclusion of shear fracturing.

Method evaluation

When evaluating the results generated by both methods the first noticeable thing is the difference in permeability evolution. Method 1 shows a very responsive jump in permeability increase at the onset of cracking, whereas, method 2 shows a more gradual increase. This difference was first observed for the simple 2D test case analysis in Section 5.2 and later on also when comparing the results with the hydraulic fracturing analysis in Chapter 6.

It could be argued that either one of the representations of the permeability increase is correct depending on the type of fracture development. If fracture growth is gradual and can be described as a relatively stable process of an increasing linking of microcracks, method 2 might be more accurate. The fracture development could, on the other hand, also be more sudden, corresponding with an immediate local increase in permeability and therefore more similar to method 1. Nevertheless, because of this difference in expressing the overall permeability of the fractured element, method 1 is slightly less stable and therefore possibly more prone to errors as it could cause more significant, sudden differences in permeability.

The simulations, according to both methods, show a mesh dependency, indicating a lower increase in permeability for a finer mesh. Yet method 1 appeared to show a slightly better convergence of the results. Furthermore, convergence of the solution, according to method 1, can be achieved if b_0 is defined as a function of the tensile strain and the crack bandwidth, thereby making it dependent on the size of the element. If b_0 were to be defined accordingly, this would mean that smaller elements have a lower initial aperture. It is disputable whether such a definition for the initial aperture is appropriate from a physical point of view. It is not at all unlikely for cracks to initially not be evenly developed over the domain, however, it would be more logical if this would also be reflected in different parameters such as k_0.

Both models show sensitive responses to differences in input parameters. For method 1, the solution considerably depends on the initial aperture, which is not very unexpected as the permeability is defined as a quadratic function of its aperture. However, because this initial aperture is a bit of an abstract concept, it might be difficult to define it appropriately before the analysis. On the other hand, the analyses have also shown that the parameter can be used to calibrate the results. Calibration of the solution is slightly more challenging for method 2, which depends on the JRC. The JRC is a more well-known and therefore more tangible rock property than b_0, making it easier to estimate correctly on beforehand but thus making calibration more difficult. Moreover, method 2 also indicates a dependency on the initial permeability. For low permeable rocks, having a low initial permeability, the simulations according to method 2 show incredibly high increases in permeability. The opposite is true for rock having a relatively high initial permeability. In that case, almost no increase in permeability is observed even though fracturing did occur. This phenomenon can probably be explained because the permeability is defined as a summation of the initial permeability and a fracture-dependent permeability. This fracture permeability is calculated irrespective of the initial state of the rock and thus will contribute much more significantly if the initial permeability is low, and will also most have no contribution at all if k_0 is relatively high. Due to this specific definition of the permeability, method 2 is only applicable in a limited range of k_0.

9. Conclusion and recommendations

The main purpose of this research is to develop a model, as a part of the Diana FEA software, that is able to simulate fluid flow through fractures, which consequently can be used for the simulation of (enhanced) geothermal energy systems. This chapter, first of all, concludes on the current state of the model with respect to the simulation of fluid flow through fractures, and secondly, provides suggestions and recommendations for further model development.

Conclusion

In case of hydraulic fracturing in EGS, cracking occurs when the tensile stresses around the borehole exceed the tensile strength of the rock material due to the increasing fluid pressure. Fracture development strongly depends on the in-situ stresses, as the rock will most easily part in the direction of the least confining stresses, causing fractures to propagate in the orthogonal direction. In order to properly represent the hydraulic fracturing process, the model should be able to link the changes in the direction and magnitude of the permeability to the presence of fractures. The fracture-dependent permeability model does so by defining a material model that includes a description of the permeability as a function of the fracture aperture. The model defines the direction and size of the fractures based on the existing principal strain field. By linking the fracture aperture development to the crack normal strains, the model is able to represent the development of mode I (extensional) fractures, which develop orthogonal to the main principal strain.

The model can be used in combination with other smeared, fracture models in the Diana FEA software, being the Total Strain crack model and the Multi-Directional fixed model. Both models can simulate multiple cracks occurring simultaneously in one point at a specific time, where for the Total Strain crack model these cracks are either fixed or constantly rotating and for the Multi-Directional fixed crack model the direction of these cracks depends on a threshold angle. Because the fracture-dependent permeability model adopts a rotating crack approach, it shows better agreement with the Total Strain crack model than with the Multi-Directional Fixed crack model. Concerning the simulation of fluid flow, Diana offers a mixture analysis. It considers an extra degree of freedom for the non-linear analysis in the form of pore pressure potentials in addition to displacements. It adheres to Darcy's law relating the fluid flow in the porous medium with the gradient in pore pressure potential through the modified permeability. This modified permeability can be updated throughout the analysis, by incorporating a relative permeability factor. The fracture-dependent permeability model has therefore been formulated in such a way that it defines a relative permeability factor, which can update the direction as well as the magnitude of the permeability in case of fracturing.

Two different methods are included for the formulation of the fracture-dependent permeability. According to the first method, the permeability is updated in the presence of fractures by treating the rock mass a continuum, whereas the second method includes the

effect of the crack by adding a fracture permeability. Method 1 requires an initial input parameter in the form of an initial aperture b_0, and for method 2 the extra input parameter is the JRC. Both methods adhere to the cubic law for the expression of the permeability change due to the presence of fractures. Based on the objectivity evaluation of the model and the two different methods, it can be concluded that the model is not completely mesh-independent, and that it also shows quite some sensitivity to its input parameters. This is true for both methods, and it is therefore not completely straightforward to draw a final conclusion on which approach is best suited for the simulation hydro-mechanical behaviour, because neither one of the two methods works perfectly. Nevertheless, there are two important arguments making method 1 favourable over method 2. Firstly, the mesh-dependency of method 1 can be successfully reduced by adopting an element size dependent definition of b_0. This is less straightforward for method 2, since it does not include a length-related parameter. And second of all, even though both methods show sensitivity to their input parameters (b_0 for method 1 and JRC for method 2), method 1 appears to be applicable to a greater range of situations than method 2 due to its independence of k_0. Based on those reasons it is concluded that method 1 is favourable over method 2.

In short, the main conclusions thus are:

- The fracture-dependent permeability model is able to simulate the occurrence and corresponding changes in permeability due to the presence of mode I (extensional) fractures that occur in the vicinity of geothermal boreholes, by evaluating the principal strain field, and linking the permeability to the fracture aperture by means of the cubic law.
- The model is implemented in the Diana FEA software through the definition of a new material model, which defines a fracture-dependent permeability that can be used in mixture analysis. The new material model can be used in combination with other smeared fracture models in Diana.
- Even though both methods show their advantages and disadvantages in the implementation, it is concluded that the first method is slightly favourable over the second method, because its mesh dependency can be reduced considerably and it can be applied to a wider range of situations because of its independence on the initial permeability field.

Nevertheless, model evaluation indicated that there is still a lot of room for improvement. First of all, the model lacks the ability to also incorporate thermal effects, which play an important role in the simulation of geothermal energy reservoirs. It is therefore not yet capable of simulating all the THM coupled processes that are relevant in EGS. And furthermore, when looking at the applicability of the fracture-dependent model for a greater range of situations other than only EGS analyses, model limitations have been identified as well. For example, the results were compared with a case study investigating the hydro-mechanical behaviour of excavation induced damaged zones in the surroundings of underground galleries. This comparison shows that the model is only capable of replicating complex in-situ behaviour to a limited extent. It is not able to simulate fractures other than extension fractures (mode I) and their influence on the permeability evolution. On top of that, the fracture-dependent permeability model is also very limited in describing an initially cracked state leading to heterogeneous conditions. The initially

cracked state could nevertheless be very important when, for example, the rock formation shows evident bedding planes and thus has an initial preferred direction of cracking. And finally, the rotating crack approach is suited for the simulation of EGS due to the monotonic loading conditions. However, under different loading conditions, such as for example cyclic shear loading or unloading conditions, the rotating approach is not appropriate. It can therefore be concluded that the current state of the fracture-dependent permeability model is not very suited for the simulation of a wider range of hydro-mechanical fracture problems other than (enhanced) geothermal energy systems.

Recommendations

The model would be able to describe the fluid flow through fractured rock in geothermal energy reservoirs more properly if also were able to represent the thermal effects on fracturing and fluid flow. In the case of thermo-hydraulic fracturing, cold water is injected, which subsequently cools the surface of the hot rock which it encounters, leading to the formation of secondary cracks perpendicular to the primary crack. The model should be able to simulate the formation of these secondary fractures, which consequently lead to leak-off and thus a loss of flow rate. Furthermore, it poses additional stresses on the rock leading to thermal contraction and thus an increase in fracture aperture. The additional contraction should be included in the calculation of the aperture based on the deformation. The differences in temperature can also affect the rock properties such as the tensile strength and fracture toughness. Incorporation of these temperature influences should thus be included in the definition of the crack criterion. Moreover finally, as the cold water travels through the rock formation and increases temperature due to the heat exchange with the rock, its viscosity will decrease thereby affecting the fluid flow. An assumption of a constant dynamic viscosity would therefore not be valid.

Based on the evaluation of the simulations, a merging together of the two methods is proposed to overcome their limitations and join their strengths. On top of that, it is also recommended to incorporate a better description of a possible initially cracked state. For example, in their study on gas flow through clay barriers, Olivella and Alonso (2008) proposes the following definition of the equivalent intrinsic permeability of an element in the direction of parallel to the fractures

$$k = k_0 + \frac{b^3}{12w} \tag{9.1}$$

where w is the width associated with each fracture and can be calculated as

$$w = \frac{s}{n} \tag{9.2}$$

with s being the element size in the direction orthogonal to the flow direction and n the number of fractures in the element. Furthermore, Olivella and Alonso (2008) defines the aperture of the fracture as following

$$b = b_0 + \Delta b \tag{9.3}$$

where the definition of Δb is similar to b in this study being a function of the deformation and an expression of the crack width according to

$$\Delta b = w\Delta\varepsilon = w(\varepsilon - \varepsilon_0) = \frac{s}{n}(\varepsilon - \varepsilon_0) \tag{9.4}$$

In short, adhering to this line of reasoning in merging methods 1 and 2 results in the following definition of k_x being the permeability in direction x

$$k_x = k_{x0} + \frac{b_x^3}{12 w_x} \tag{9.5}$$

where k_{x0} is the initial permeability, b_x is the aperture and w_x is the width associated with each fracture in direction x, which can be calculated as

$$w_x = \frac{h_{cr}}{n_x} \tag{9.6}$$

with h_{cr} being the crack bandwidth, according to Govindjee et al. (1995), and n_x the number of cracks in direction x. The aperture is defined as

$$b_x = b_{x0} + \Delta b_x = b_{x0} + w_x \Delta \varepsilon \tag{9.7}$$

This newly defined expression for fracture-dependent permeability adheres to method 2 by expressing it as a summation of both the initial and the fracture permeability. It uses an expression for b_0 as proposed in method 1, which is not only assumed to be more appropriate in many cases when fractures will most likely initially be present, but it also allows for some calibration of the results. Furthermore, in order to reduce mesh-dependency it is recommended to define b_0 as an element size dependent parameter rather than a constant value. On top of that, the new definition adds an aspect of initial fracture directionality in the expression by employing a valuation of the number of fractures present in a specific direction (n_x). It is assumed that the fracture-dependent permeability model would benefit from this redefinition of the permeability due to the more detailed description of an initially cracked state of the rock while maintaining its simplicity and only requiring two additional input parameters in the form of b_0 and n. However, if such a description is included, the rotating crack approach becomes less appropriate and should therefore be reconsidered.

Moreover, in the case of further model development, it would be recommended to either seek for a different numerical study simulating the hydro-mechanical behaviour of rock in the vicinity of geothermal boreholes, which contains a more detailed and precise description of the experimental conditions, (numerical) parameters and results. Or alternatively, the other option is to self perform a small-scale experimental study investigating hydraulic fracturing, such that all conditions and results are known precisely, and findings can be compared more appropriately.

And finally, if there is a wish to apply the model to a broader spectrum of situations, for example, in describing the behaviour of excavation induced damaged zones near underground galleries, it is recommended to not only include tensile cracking (mode I) but also the development of shear cracking (mode II and mode II). Taking it one step further this would mean that the definition of the aperture according to Equation (9.7) would not only be a function of the crack normal strain but would also incorporate an expression of the shear deformation. In this case, the rotating crack approach that the model currently adheres to should definitely also be changed, or the user should be given the possibility to change it to either a fixed or a multi-directional fixed approach.

References

AbuAisha, M., Loret, B., & Eaton, D. (2016). Enhanced geothermal systems (EGS): Hydraulic fracturing in a thermo-poroelastic framework. *Journal of Petroleum Science and Engineering*, *146*, 1179–1191.

Adachi, J., Siebrits, E., Peirce, A., & Desroches, J. (2007). Computer simulation of hydraulic fractures. *International Journal of Rock Mechanics and Mining Sciences*, *44*(5), 739–757.

Armand, G., Leveau, F., Nussbaum, C., de La Vaissiere, R., Noiret, A., Jaeggi, D., Landrein, P., & Righini, C. (2014). Geometry and properties of the excavation-induced fractures at the meuse/haute-marne url drifts. *Rock Mechanics and Rock Engineering*, *47*(1), 21–41.

Atkinson, B., & Meredith, P. (1987). Fracture mechanics of rock, Academic Press Geology Series. *The theory of subcritical crack growth with applications to minerals and rocks* (p. 119).

Barton, N., Bandis, S., & Bakhtar, K. (1985). Strength, deformation and conductivity coupling of rock joints. *International Journal of Rock Mechanics and Mining Sciences*, *22*(3), 121–140.

Barton, N., & Choubey, V. (1977). The shear strength of rock joints in theory and practice. *Rock mechanics*, *10*(1-2), 1–54.

Carman, P. (1961). L'écoulement des gaz á travers les milieux poreux, bibliothéque des sciences et techniques nucléaires. *Paris: Presses Universitaires de France*.

Chen, Y., & Zhou, C. (2011). Stress/strain-dependent properties of hydraulic conductivity for fractured rocks. *Developments in Hydraulic Conductivity Research*, 1.

Chen, Y., Zhou, C., & Sheng, Y. (2007). Formulation of strain-dependent hydraulic conductivity for a fractured rock mass. *International Journal of Rock Mechanics and Mining Sciences*, *44*(7), 981–996.

DIANA FEA bv. (2019). *Diana user's manual* [Release 10.3].

Fjar, E., Holt, R. M., Raaen, A., & Horsrud, P. (2008). *Petroleum related rock mechanics*. Elsevier.

Gan, Q., & Elsworth, D. (2016). A continuum model for coupled stress and fluid flow in discrete fracture networks. *Geomechanics and Geophysics for Geo-Energy and Geo-Resources*, *2*(1), 43–61.

Gens, A., Vaunat, J., Garitte, B., & Wileveau, Y. (2007). In situ behaviour of a stiff layered clay subject to thermal loading: Observations and interpretation. *Géotechnique*, *57*(2), 207–228.

Govindjee, S., Kay, G. J., & Simo, J. C. (1995). Anisotropic modelling and numerical simulation of brittle damage in concrete. *International journal for numerical methods in engineering*, *38*(21), 3611–3633.

Grant, M. (2013). *Geothermal reservoir engineering*. Elsevier.

Griffith, A. A. (1921). Vi. The phenomena of rupture and flow in solids. *Philosophical Transactions of the Royal Society of London. Series A, containing papers of a mathematical or physical character*, *221*(582-593), 163–198.

Hoek, E., Carranza-Torres, C., Corkum, B., et al. (2002). Hoek-brown failure criterion-2002 edition. *Proceedings of NARMS-Tac*, *1*(1), 267–273.

Hubbert, M. K., & Willis, D. G. (1957). Mechanics of hydraulic fracturing. *Transactions of Society of Petroleum Engineers of AIME*, *210*, 153–163.

Janssen, Z., & Wanhill. (2004). *Fracture mechanics (2nd ed.)* London: Spon Press.

Kissling, W., Ellis, S., & McNamara, D. D. (2015). Modelling fluid flow through fractured rock: Examples using tvz geothermal reservoirs. *New Zealand Geothermal Workshop 2015*.

Kozeny, J. (1927). Uber kapillare leitung der wasser in boden. *Royal Academy of Science, Vienna, Proc. Class I*, *136*, 271–306.

Kranz, R. L. (1983). Microcracks in rocks: A review. *Tectonophysics*, *100*(1-3), 449–480.

Latief, F. D. E., & Fauzi, U. (2012). Kozeny-Carman and empirical formula for the permeability of computer rock models. *International Journal of Rock Mechanics and Mining Sciences*, *50*, 117–123.

Lyons, W. C., & Plisga, G. J. (2011). *Standard handbook of petroleum and natural gas engineering*. Elsevier.

Meijer, K. L. (1985). Computation of stresses and strains in saturated soil.

Olivella, S., & Alonso, E. (2008). Gas flow through clay barriers. *Géotechnique*, *58*(3), 157–176.

Oliver, J. (1989). A consistent characteristic length for smeared cracking models. *International Journal for Numerical Methods in Engineering*, *28*(2), 461–474.

Pardoen, B. (2015). *Hydro-mechanical analysis of the fracturing induced by the excavation of nuclear waste repository galleries using shear banding* (Doctoral dissertation). Université de Liège, Liège, Belgique.

Rots, J. (1988). Computational modeling of concrete fracture [phd dissertation]. *Delft, The Netherlands: Delft University of Technology*.

Salimzadeh, S., Paluszny, A., Nick, H. M., & Zimmerman, R. W. (2018). A three-dimensional coupled thermo-hydro-mechanical model for deformable fractured geothermal systems. *Geothermics*, *71*, 212–224.

Shao, J.-F., Zhou, H., & Chau, K. (2005). Coupling between anisotropic damage and permeability variation in brittle rocks. *International Journal for Numerical and Analytical Methods in Geomechanics*, *29*(12), 1231–1247.

Snow, D. T. (1969). Anisotropie permeability of fractured media. *Water resources research*, *5*(6), 1273–1289.

Souley, M., Homand, F., Pepa, S., & Hoxha, D. (2001). Damage-induced permeability changes in granite: A case example at the url in canada. *International Journal of Rock Mechanics and Mining Sciences*, *38*(2), 297–310.

Taghipoor, S., Roostaei, M., Velayati, A., Sharbatian, A., Chan, D., & Nouri, A. (2020). Numerical investigation of the hydraulic fracturing mechanisms in oil sands. *Underground Space*.

Tomac, I., & Sauter, M. (2018). A review on challenges in the assessment of geomechanical rock performance for deep geothermal reservoir development. *Renewable and Sustainable Energy Reviews*, *82*, 3972–3980.

Vecchio, F. J., & Collins, M. P. (1986). The modified compression-field theory for reinforced concrete elements subjected to shear. *ACI J.*, *83*(2), 219–231.

Wileveau, Y., Cornet, F., Desroches, J., & Blumling, P. (2007). Complete in situ stress determination in an argillite sedimentary formation. *Physics and Chemistry of the Earth, Parts A/B/C*, *32*(8-14), 866–878.

Zhou, X., Ghassemi, A., & Cheng, A.-D. (2009). A three-dimensional integral equation model for calculating poro-and thermoelastic stresses induced by cold water injection into a geothermal reservoir. *International Journal for Numerical and Analytical Methods in Geomechanics*, *33*(14), 1613–1640.

Zimmerman, R. W., & Bodvarsson, G. S. (1996). Hydraulic conductivity of rock fractures. *Transport in porous media*, *23*(1), 1–30.